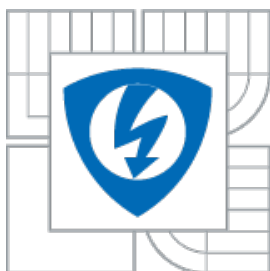




VYSOKÉ UČENÍ TECHNICKÉ V BRNĚ
BRNO UNIVERSITY OF TECHNOLOGY



FAKULTA ELEKTROTECHNIKY A KOMUNIKAČNÍCH
TECHNOLOGIÍ
ÚSTAV FYZIKY

FACULTY OF ELECTRICAL ENGINEERING AND COMMUNICATION
DEPARTMENT OF PHYSICS

TRANSPORT NÁBOJE V Ta_2O_5 OXIDOVÝCH NANOVRSŤVÁCH S APLIKACÍ NA TANTALOVÉ KONDENZÁTORY

CHARGE CARRIER TRANSPORT IN Ta_2O_5 OXIDE NANOLAYERS WITH APPLICATION TO THE
TANTALUM CAPACITORS

DOKTORSKÁ PRÁCE
DOCTORAL THESIS

AUTOR PRÁCE
AUTHOR

Ing. MARTIN KOPECKÝ

VEDOUCÍ PRÁCE
SUPERVISOR

doc. Ing. VLASTA SEDLÁKOVÁ, Ph.D.

BRNO 2015

ABSTRAKT

Studium transportu náboje v Ta₂O₅ oxidových nanovrstvách se zaměřuje na objasnění vlivu defektů na vodivost těchto vrstev a na identifikaci transportních mechanismů projevujících se při nízkých teplotách. Soustředím se na studium oxidových nanovrstev Ta₂O₅ vytvořených pomocí anodické oxidace. Proces výroby Ta₂O₅ zahrnuje řadu parametrů, jež ovlivňují koncentraci defektů (oxidových vakancí) v této struktuře. Vrstva oxidu Ta₂O₅ o tloušťce 20 až 200 nm se často používá jako dielektrikum pro tantalové kondenzátory, které se staly nedílnou součástí elektrotechnického průmyslu. Kondenzátory s Ta₂O₅ dielektrickou vrstvou lze modelovat jako strukturu MIS (kov – izolant – polovodič). Anodu tvoří tantal s kovovou vodivostí, katodu potom MnO₂ či vodivý polymer (CP), které jsou polovodiče. Hodnoty elektronových afinit, respektive výstupních prací, jednotlivých materiálů potom určují výšku potenciálových bariér vytvořených na rozhraních kov-izolant (M-I) a izolant-polovodič (I-S). Mechanizmy transportu náboje lze určit analýzou *I-V* charakteristiky zbytkového proudu. Dominantní mechanismy transportu náboje izolační vrstvou při pokojové teplotě jsou ohmický, Poole-Frenkelův a tunelování při zapojení kondenzátoru v normálním modu (kladné napětí je připojeno na anodě) a ohmický mechanismus a termoemise přes Schottkyho bariéru při zapojení v reversním modu (kladné napětí je připojeno na katodě). Uplatnění jednotlivých vodivostních mechanismů je závislé na teplotě a intenzitě elektrického pole v izolantu. Hodnota zbytkového proudu je významným indikátorem kvality daného izolantu. Zbytkový proud závisí na technologii výroby kondenzátoru, významně především na parametrech anodické oxidace a na materiálu katody. *I-V* charakteristiky zbytkového proudu se měří v normálním a reversním módu. *I-V* charakteristika je výrazně nesymetrická, a proto tyto kondenzátory musí být vhodně polarizovány. Nesymetrie *I-V* charakteristiky se snižuje s klesající teplotou, při teplotě pod 50 K a je možno některé kondenzátory používat jako bipolární součástky. Z analýzy *I-V* charakteristik v rozsahu teplot 12 – 250 K jsem určil dominantní mechanismy transportu náboje v Ta₂O₅ vrstvách v rozsahu teplot 12 až 100 K a 100 až 250 K. Při teplotách v rozsahu 12 -100 K se uplatňují ohmický a tunelový proud, a to jak v normálním, tak v reversním modu. Vedle těchto dvou mechanismů, jež se projevují u všech měřených vzorků, jsem v tomto teplotním rozsahu sledoval u vzorků s katodou z CP ještě tunelování z HOMO hladiny ve vodivém polymeru do pásu defektů v izolantu a transport omezený prostorovým nábojem (SCHLC). V teplotním rozsahu 100 až 250 K se začíná vedle ohmického a tunelového proudu uplatňovat i Poole-Frenkelův mechanismus vedení náboje (v normálním modu) a termoemise přes Schottkyho bariéru (v reversním modu). U jednoho vzorku s MnO₂ katodou byl sledován i SCHLC. Z parametrů tunelových proudů jsem určil parametry MIS modelu kondenzátoru - hodnotu potenciálových bariér na rozhraních M-I a I-S a také závislost výšky těchto bariér na teplotě. Ze složky SCHLC jsem vypočítal pohyblivost nosičů náboje ve vrstvách Ta₂O₅. Měření *C-V* charakteristik při různých teplotách v rozsahu 12 až 300 K je využito pro určení výšky potenciálové bariéry na rozhraní I-S, pro určení závislosti kapacity na teplotě, určení efektivní koncentrace defektů v izolační Ta₂O₅ vrstvě a dále pro výpočet efektivní plochy elektrod. Z výbrusu vzorků na skenovacím elektronovém mikroskopu byly určeny tloušťky dielektrika Ta₂O₅ pro jednotlivé vyhodnocované řady kondenzátorů.

Klíčová slova: tantalové kondenzátory, MIS struktura, transport elektronu, tunelový proud, oxid tantalitý, vodivý polymer, oxid manganičitý, Ta₂O₅

ABSTRACT

The study of charge carrier transport in Ta₂O₅ oxide nanolayers is oriented on the explanation of the defects influence on the conductivity of these layers and on the identification of the charge transport mechanisms involved in the low temperature range. I am concerned on the study of tantalum pentoxide nanolayers provided by the anodic oxidation. The technology process of oxide preparation contains many parameters which influence the concentration of defects (probably oxygen vacancies) in the structure. Tantalum pentoxide of the thickness 20 to 200 nm is used as a dielectric layer in the tantalum capacitors. These capacitors can be considered as a metal-insulator-semiconductor (MIS) structure. Anode is formed from the tantalum powder with metallic conductivity and cathode is from manganese dioxide (MnO₂) or conducting polymer (CP), respectively, both with semiconductor conductivity. The value of Ta₂O₅ electron affinity and work functions of Ta, MnO₂ and CP, respectively, determine the heights of potential barriers formed on the metal-insulator (M-I) and insulator-semiconductor (I-S) interfaces. The dominant mechanisms of the charge carriers' transport at the room temperature in the Ta₂O₅ insulating layer are ohmic, Poole-Frenkel and tunneling in the normal mode (positive bias on anode) and ohmic mechanism and thermionic emission over the Schottky barrier in the reverse mode (positive bias on cathode), and these could be determined from the analysis of the leakage current *I-V* characteristic. Particular transport mechanisms are dependent on temperature and electric field in the insulation layer. The leakage current is important indicator of the insulation layer quality. Its value depends on the production technology, namely on the anodic oxidation and the cathode material. *I-V* characteristic is measured both in normal and reverse mode. *I-V* characteristic is asymmetric at the room temperature. This asymmetry decreases with decreasing temperature, and for the temperature below 50 K some of capacitors could be used as bipolar devices. I have determined the dominant charge transport mechanisms in Ta₂O₅ layers in the temperature ranges 12 to 100 K and 100 to 250 K, respectively, from the analysis of *I-V* characteristics measured in the range 12 to 250 K. Ohmic and tunneling mechanisms are involved in charge transport both in normal and reverse mode in the temperature range 12 to 100 K for all evaluated samples. Beside that the tunneling from HOMO level in CP into the defect band in the insulator and space charge limited current (SCHLC) are observed in this temperature range for the samples with CP cathode. Additional current component driven by the Poole-Frenkel mechanism is observed in the range 100 to 250 K in the normal mode and thermionic emission over the Schottky barrier is involved in reverse mode in this temperature range. SCHLC was detected for one sample with MnO₂ cathode at the temperature 250 K. I have determined the MIS model parameters from the tunneling current components evaluation, namely the heights of potential barriers formed on the M-I and I-S interfaces and their temperature dependence. I have calculated the charge carriers' mobility from the SCHLC component evaluation. *C-V* characteristic measurements and their temperature dependencies could be used for the estimation of I-S potential barrier height, capacitor electrodes effective area and the defects' concentration in the Ta₂O₅ layer. The analysis of the capacitor cross-sections was performed by scanning electron microscope and the measurements of Ta₂O₅ layer thickness were performed for the each series of the capacitors.

Keywords: tantalum capacitor, MIS structure, electron transport, tunneling current, tantalum pentoxide, conducting polymer, manganese dioxide, Ta₂O₅

KOPECKÝ, M. *Transport náboje v Ta₂O₅ oxidových nanovrstvách s aplikací na tantalové kondenzátory*. Brno: Vysoké učení technické v Brně, Fakulta elektrotechniky a komunikačních technologií, 2015. 125 s. Vedoucí disertační práce doc. Ing. Vlasta Sedláková, Ph.D.

Prohlášení

Prohlašuji, že svou dizertační práci na téma „Transport náboje v Ta₂O₅ oxidových nanovrstvách s aplikací na tantalové kondenzátory“ jsem vypracoval samostatně pod vedením školitele a s použitím odborné literatury a dalších informačních zdrojů, které jsou všechny citovány v práci a uvedeny v seznamuliteratury na konci práce.

Jako autor uvedené dizertační práce dále prohlašuji, že v souvislosti s vytvořením této disertační práce jsem neporušil autorská práva třetích osob, zejména jsem nezasáhl nedovoleným způsobem do cizích autorských práv osobnostních a jsem si plně vědom následků porušení ustanovení § 11 a následujících autorského zákona č. 121/2000 Sb., včetně možných trestněprávních důsledků vyplývajících z ustanovení § 152 trestního zákona č. 140/1961 Sb.

V Brně, dne 5. 1. 2015

.....
podpis autora

Poděkování

Děkuji vedoucí disertační práce Doc. Ing. Vlastě Sedlákové, Ph.D., vedoucímu Ústavu fyziky Prof. Ing. Lubomíru Grmelovi, CSc. a v neposlední řadě i Prof. Ing. RNDr. Josefu Šikulovi, DrSc. za cenné rady a účinnou metodickou, pedagogickou a odbornou pomoc při zpracování mé dizertační práce. Také za velmi vstřícný osobní přístup.

V Brně, dne 5. 1. 2015

.....
podpis autora

Content

LIST OF PICTURES	iii
LIST OF TABLES	xii
LIST OF USED SYMBOLS	xiii
1. INTRODUCTION	1
2. STATE OF ART	3
2.1. TANTALUM CAPACITORS	3
2.2. TECHNOLOGY OF TANTALUM CAPACITORS	6
2.2.1. TANTALUM ANODE CREATION	6
2.2.2. TA_2O_5 DIELECTRIC LAYER FORMING	8
2.2.3. PREPARATION OF THE CATHODE SIDE	11
3. MIS MODEL OF TANTALUM CAPACITORS	14
3.1. THE THEORY OF MIS STRUCTURE	16
3.2. CHARGE TRANSPORT IN TANTALUM CAPACITOR	23
3.2.1. OHMIC CURRENT COMPONENT	23
3.2.2. SPACE CHARGE LIMITED CURRENT	24
3.2.3. POOLE-FRENKEL CURRENT COMPONENT	25
3.2.4. SCHOTTKY CURRENT COMPONENT	27
3.2.5. TUNNELING CURRENT COMPONENT	28
3.2.6. THERMIONIC EMISSION LIMITED CURRENT OVER A SCHOTTKY BARRIER	32
4. AIMS OF DOCTORAL THESIS	34
5. EXPERIMENTAL SETUP AND MEASURED SAMPLES	35
5.1. SAMPLE DESCRIPTION AND PREPARATION	35
5.2. SEM ANALYSIS OF THE STRUCTURES	37
5.3. <i>I-V</i> CHARACTERISTICS	40
5.4. <i>C-V</i> CHARACTERISTICS	44
6. EXPERIMENTAL RESULTS	47
6.1. ANALYSIS OF <i>C-V</i> CHARACTERISTICS FOR 10 K UP TO 300 K	47
6.2. ANALYSIS OF <i>I-V</i> MEASUREMENTS	52
6.2.1. ANALYTICAL METHOD FOR DCL COMPONENTS DETERMINATION IN NORMAL MODE	55
6.2.2. ANALYTICAL METHOD FOR DCL COMPONENTS DETERMINATION IN REVERSE MODE	58
6.2.3. TUNNELING FROM HOMO LEVEL OF CONDUCTING POLYMER	61
6.2.4. POTENTIAL BARRIER ESTIMATION	63
6.2.4.1. POTENTIAL BARRIER BETWEEN TA_2O_5 AND CATHODE	63
6.2.4.2. POTENTIAL BARRIER BETWEEN ANODE AND TA_2O_5	67
6.2.5. GRAPHICAL METHOD FOR THE OHMIC CURRENT COMPONENT ANALYSIS	70
6.2.6. GRAPHICAL METHOD FOR THE POOLE-FRENKEL CURRENT COMPONENT ANALYSIS	73
6.2.7. GRAPHICAL METHOD FOR THE SCHOTTKY CURRENT COMPONENT ANALYSIS	74
6.2.8. GRAPHICAL METHOD FOR THE FOWLER-NORHEIM TUNNELING FOR NORMAL MODE	76

6.2.9. GRAPHICAL METHOD FOR THE FOWLER-NORHEIM TUNNELING FOR REVERSE MODE _____	80
6.2.10. THERMIONIC EMISSION LIMITED CURRENT OVER THE SCHOTTKY BARRIER _____	83
6.2.11. SPACE CHARGE LIMITED CURRENT _____	87
7. DISCUSSION _____	92
8. CONCLUSION _____	100
REFERENCES _____	101
AUTHOR'S PRODUCTS _____	105
AUTOR'S INVOLVEMENT IN PROJECTS _____	106

List of pictures

FIG. 2.1	FACEDOWN CONSTRUCTION IN TANTALUM CAPACITORS WITH THE TERMINALS	4
FIG. 2.2	SMALL CASE STANDARD VS. FACEDOWN [12]	4
FIG. 2.3	VARIOUS TYPES OF TANTALUM POWDER	6
FIG. 2.4	PRESSING TANTALUM POWDER AND SINTRATION PROCESS OF ANODE	7
FIG. 2.5	STRUCTURE OF TANTALUM PARTICLES AND CONNECTIONS AFTER SINTRATION PROCESS	7
FIG. 2.6	SEM PICTURE OF THE LAYERS INSIDE THE CAPACITORS AND DESCRIPTION OF FRAGMENTS Ta_2O_5 OF ANODE	8
FIG. 2.7	FORMING VOLTAGE AND FORMING CURRENT DEPENDENCE ON TIME [16]	9
FIG. 2.8	THE ELECTROCHEMICAL REACTION OF THE GROWING DIELECTRIC LAYER	9
FIG. 2.9	POTENTIAL BARRIERS IN THE SYSTEM OXIDE-ELECTROLYTE [16]	10
FIG. 2.10	I - V CHARACTERISTIC FOR REVERSE MODE FOR DIFFERENT ANODIZATION CURRENTS AT TEMPERATURE 300 K [8]	11
FIG. 2.11	THE DIFFERENCE OF THE MATERIAL FOR THE MnO_2 AN CP [17]	12
FIG. 2.12	BASIC STRUCTURE OF TANTALUM CAPACITOR	12
FIG. 3.1	IDEAL STRUCTURE OF PHYSICAL MODEL OF CAPACITOR	14
FIG. 3.2	BASIC MIS STRUCTURE OF TANTALUM CAPACITOR	15
FIG. 3.3	MIS MODEL STRUCTURE BEFORE THERMODYNAMIC EQUILIBRIUM FOR THE TANTALUM CAPACITOR WITH MnO_2 CATHODE	17
FIG. 3.4	MIS MODEL STRUCTURE BEFORE THERMODYNAMIC EQUILIBRIUM FOR THE TANTALUM CAPACITOR WITH CP CATHODE	17
FIG. 3.5	MIS MODEL STRUCTURE IN THERMODYNAMIC EQUILIBRIUM FOR THE TANTALUM CAPACITOR WITH MnO_2 CATHODE	18
FIG. 3.6	MIS MODEL STRUCTURE IN THERMODYNAMIC EQUILIBRIUM FOR THE TANTALUM CAPACITOR WITH CP CATHODE	18
FIG. 3.7	MIS MODEL STRUCTURE FOR APPLIED VOLTAGE ON THE TANTALUM CAPACITOR WITH MnO_2 CATHODE – NORMAL MODE	19
FIG. 3.8	MIS MODEL STRUCTURE FOR APPLIED VOLTAGE ON THE TANTALUM CAPACITOR WITH CP CATHODE – NORMAL MODE	20
FIG. 3.9	BASIC PRINCIPAL OF THE CHARGE CARRIER TRANSPORT IN THE CAPACITOR	20
FIG. 3.10	MIS MODEL STRUCTURE FOR APPLIED VOLTAGE ON THE TANTALUM CAPACITOR WITH MnO_2 CATHODE – REVERSE MODE	21
FIG. 3.11	MIS MODEL STRUCTURE FOR APPLIED VOLTAGE ON THE TANTALUM CAPACITOR WITH CP CATHODE – REVERSE MODE	22
FIG. 3.12	DEFECT IN THE Ta_2O_5 STRUCTURE AS A SOURCE OF LEAKAGE CURRENT	23
FIG. 3.13	I - V CHARACTERISTIC (LINEAR SCALE) AND J - E CHARACTERISTIC (LOGARITHMIC SCALE) FOR SAMPLE KOL2012 – 05 MEASURED FOR TEMPERATURES 12 K, 40 K AND 150 K	24
FIG. 3.14	ANALYTICAL METHOD FOR DETERMINATION OF POOLE-FRENKEL CURRENT COMPONENT FROM I - V CHARACTERISTICS FOR THE SAMPLE KOL2012-05 IN NORMAL MODE FOR THE TEMPERATURE 150 K	27

FIG. 3.15	GRAPHICAL METHOD OF POOLE-FRENKEL CURRENT COMPONENT EVALUATION WITH EXPERIMENTALLY DETERMINED LINE FOR THE SAMPLE KOL2012-05 IN NORMAL MODE FOR THE TEMPERATURE 150K _____	27
FIG. 3.16	TUNNELING PARAMETER E_T AND TUNNELING PARAMETER U_T VS. BARRIER HEIGHT CALCULATED FOR DIFFERENT ELECTRON EFFECTIVE MASS VALUES FOR THE DIELECTRIC LAYER THICKNESS 30 NM _____	29
FIG. 3.17	TUNNELING PROBABILITY COEFFICIENT D VS. TUNNELING BARRIER THICKNESS FOR DIFFERENT BARRIER ENERGY VALUES _____	30
FIG. 3.18	THE TRIANGULAR POTENTIAL BARRIER FOR ELECTRON TUNNELING _____	31
FIG. 3.19	ANALYTICAL METHOD FOR DETERMINATION OF TUNNELING CURRENT COMPONENT FOR SAMPLE KOL2012-05 AT TEMPERATURE 12 K _____	31
FIG. 3.20	INTERPRETATION OF FOWLER-NORDHEIM GRAPH BY GRAPHICAL METHOD FOR SAMPLE KOL2012-05 AT TEMPERATURE 12 K _____	32
FIG. 5.1	THE SOLDERED SAMPLES ON THE TESTING BOARD _____	35
FIG. 5.2	THE GILT METAL WIRES CONNECTED FOR THE EACH CAPACITOR _____	36
FIG. 5.3	PREPARED SAMPLES FOR THE SEM MICROSCOPY IN EPOXY RESIN _____	37
FIG. 5.4	SEM FIGURES OF WHOLE CAPACITOR STRUCTURE CROSS-SECTION FOR THE SAMPLES CTS2012 AND KOL2012 _____	37
FIG. 5.5	SEM PICTURE OF POROUS TANTALUM ANODE FOR SAMPLE KOL2012 _____	38
FIG. 5.6	SEM PICTURE FOR SAMPLE KOL2012 FOR THE DETERMINATION OF Ta_2O_5 AND CP LAYER THICKNESS _____	38
FIG. 5.7	SEM PICTURE FOR SAMPLE CTS2012 FOR THE DETERMINATION OF Ta_2O_5 AND MnO_2 LAYER THICKNESS _____	39
FIG. 5.8	SEM PICTURE FOR SAMPLE MK2012 FOR THE DETERMINATION OF Ta_2O_5 AND MnO_2 LAYER THICKNESS _____	39
FIG. 5.9	THE BLOCK SCHEME OF $I-V$ OR $I-T$ CHARACTERISTICS _____	40
FIG. 5.10	THE ELECTRICAL CIRCUIT INSIDE THE CRYOSTAT SYSTEM _____	41
FIG. 5.11	REAL CONNECTIONS OF THE CRYOSTAT SYSTEM _____	41
FIG. 5.12	$I-V$ CHARACTERISTICS FOR SAMPLE KOL2012 - 02 FOR THE NORMAL AND REVERSE MODE FROM 12 K UP TO 150 K _____	42
FIG. 5.13	BLOCK SCHEME OF THE $C-V$ MEASUREMENT _____	43
FIG. 5.14	ELECTRIC CIRCUIT INSIDE IN THE CRYOSTAT SYSTEM FOR $C-V$ CHARACTERISTICS MEASUREMENTS _____	43
FIG. 5.15	$C-V$ CHARACTERISTICS FOR 5 SAMPLES OF CTS2012 SERIES MEASURED AT FREQUENCY 20 HZ FOR TEMPERATURE 300 K _____	44
FIG. 5.16	$1/C^2$ VS. VOLTAGE FOR SAMPLE CTS2012-01 FOR TEMPERATURES 10 K, 100 K, 300 K _____	45
FIG. 5.17	DONOR CONCENTRATION N_D VS. U_D FOR SAMPLE CTS2012-01 FOR TEMPERATURES 10 K, 100 K, 300 K _____	45
FIG. 6.1	MEASURED DEPENDENCE C VS. VOLTAGE AND CALCULATED DEPENDENCE $1/C^2$ VS. VOLTAGE FOR SAMPLE CTS2012-03 FOR TEMPERATURES 10 K, 100 K, 300 K _____	46
FIG. 6.2	MEASURED DEPENDENCE C VS. VOLTAGE AND CALCULATED DEPENDENCE $1/C^2$ VS. VOLTAGE FOR SAMPLE CTS2012-05 FOR TEMPERATURES 10 K, 100 K, 300 K _____	46
FIG. 6.3	DONOR CONCENTRATION N_D VS. U_D FOR SAMPLE CTS2012-03 FOR TEMPERATURES 10 K, 100 K, 300 K _____	47

FIG. 6.4	DONOR CONCENTRATION N_D VS. U_D FOR SAMPLE CTS2012-05 FOR TEMPERATURES 10 K, 100 K, 300 K	47
FIG. 6.5	MEASURED DEPENDENCE C VS. VOLTAGE AND CALCULATED DEPENDENCE $1/C^2$ VS. VOLTAGE FOR SAMPLE MK2012-01 FOR TEMPERATURES 10 K, 100 K, 300 K	48
FIG. 6.6	MEASURED DEPENDENCE C VS. VOLTAGE AND CALCULATED DEPENDENCE $1/C^2$ VS. VOLTAGE FOR SAMPLE MK2012-03 FOR TEMPERATURES 10 K, 100 K, 300 K	48
FIG. 6.7	MEASURED DEPENDENCE C VS. VOLTAGE AND CALCULATED DEPENDENCE $1/C^2$ VS. VOLTAGE FOR SAMPLE MK2012-04 FOR TEMPERATURES 10 K, 100 K, 300 K	48
FIG. 6.8	DONOR CONCENTRATION N_D VS. U_D FOR SAMPLE MK2012-01, MK2012-03, MK2012-04 FOR TEMPERATURE 300 K	49
FIG. 6.9	MEASURED DEPENDENCE C VS. VOLTAGE AND CALCULATED DEPENDENCE $1/C^2$ VS. VOLTAGE FOR SAMPLES KOL2012 - 01, KOL2012 - 03, KOL2012 - 05 FOR TEMPERATURE 300 K	49
FIG. 6.10	DONOR CONCENTRATION N_D VS. U_D FOR SAMPLE KOL2012-01, KOL2012-03, KOL2012-05 FOR TEMPERATURE 300 K	52
FIG. 6.11	$I - V$ CHARACTERISTICS FOR SAMPLE KOL2012 - 02 IN THE TEMPERATURE RANGE FROM 12 K UP TO 150 K FOR THE NORMAL AND REVERSE MODE, LEFT GRAPH SHOWS $I - V$ CHARACTERISTICS FOR SELECTED TEMPERATURES	51
FIG. 6.12	$I - V$ CHARACTERISTICS FOR SAMPLE KOL2012 - 03 IN THE TEMPERATURE RANGE FROM 12 K UP TO 150 K FOR THE NORMAL AND REVERSE MODE, LEFT GRAPH SHOWS $I - V$ CHARACTERISTICS FOR SELECTED TEMPERATURES	51
FIG. 6.13	$I - V$ CHARACTERISTICS FOR SAMPLE KOL2012 - 05 IN THE TEMPERATURE RANGE FROM 12 K UP TO 150 K FOR THE NORMAL AND REVERSE MODE, LEFT FIGURE SHOWS $I - V$ CHARACTERISTICS FOR SELECTED TEMPERATURES	52
FIG. 6.14	$I - V$ CHARACTERISTICS FOR SAMPLE CTS2012 - 01 FOR THE TEMPERATURES 12 K, 100 K AND 150 K FOR THE NORMAL AND REVERSE MODE	52
FIG. 6.15	$I - V$ CHARACTERISTICS FOR SAMPLE CTS2012 - 04 FOR THE TEMPERATURES 12 K, 100 K AND 150 K FOR THE NORMAL AND REVERSE MODE	53
FIG. 6.16	$I - V$ CHARACTERISTICS FOR SAMPLE MK2012 - 01 IN THE TEMPERATURE RANGE FROM 12 K UP TO 150 K FOR THE NORMAL AND REVERSE MODE	53
FIG. 6.17	$I - V$ CHARACTERISTICS FOR SAMPLE MK2012 - 02 IN THE TEMPERATURE RANGE FROM 12 K UP TO 150 K FOR THE NORMAL AND REVERSE MODE	53
FIG. 6.18	$I - V$ CHARACTERISTICS FOR SAMPLE MK2012 - 03 IN THE TEMPERATURE RANGE FROM 12 K UP TO 150 K FOR THE NORMAL AND REVERSE MODE	54
FIG. 6.19	ANALYTICAL METHOD FOR THE ANALYSIS OF DATA MEASURED FOR SAMPLE KOL2012 - 02 IN NORMAL MODE FOR TEMPERATURE RANGE FROM 12 K UP TO 150 K	54
FIG. 6.20	ANALYTICAL METHOD FOR THE ANALYSIS OF DATA MEASURED FOR SAMPLE KOL2012 - 05 IN NORMAL MODE FOR TEMPERATURE RANGE FROM 12 K UP TO 150 K	55
FIG. 6.21	ANALYTICAL METHOD FOR THE ANALYSIS OF DATA MEASURED FOR SAMPLE CTS2012 - 01 IN NORMAL MODE FOR TEMPERATURE RANGE FROM 12 K UP TO 150 K	55

FIG. 6.22	ANALYTICAL METHOD FOR THE ANALYSIS OF DATA MEASURED FOR SAMPLE CTS2012 - 04 IN NORMAL MODE FOR TEMPERATURE RANGE FROM 12 K UP TO 150 K	55
FIG. 6.23	ANALYTICAL METHOD FOR THE MK2012 - 01 IN NORMAL MODE FOR TEMPERATURE RANGE FROM 12 K UP TO 150 K	56
FIG. 6.24	ANALYTICAL METHOD FOR THE ANALYSIS OF DATA MEASURED FOR SAMPLE MK2012 - 02 IN NORMAL MODE FOR TEMPERATURE RANGE FROM 12 K UP TO 150 K	56
FIG. 6.25	ANALYTICAL METHOD FOR THE ANALYSIS OF DATA MEASURED FOR SAMPLE MK2012 - 03 IN NORMAL MODE FOR TEMPERATURE RANGE FROM 12 K UP TO 150 K	56
FIG. 6.26	ANALYTICAL METHOD FOR THE ANALYSIS OF DATA MEASURED FOR SAMPLE KOL2012 - 02 IN REVERSE MODE FOR TEMPERATURE RANGE FROM 12 K UP TO 100 K	57
FIG. 6.27	ANALYTICAL METHOD FOR THE ANALYSIS OF DATA MEASURED FOR SAMPLE KOL2012 - 03 IN REVERSE MODE FOR TEMPERATURE RANGE FROM 12 K UP TO 200 K	57
FIG. 6.28	ANALYTICAL METHOD FOR THE ANALYSIS OF DATA MEASURED FOR SAMPLE KOL2012 - 05 IN REVERSE MODE FOR TEMPERATURE RANGE FROM 12 K UP TO 100 K	58
FIG. 6.29	ANALYTICAL METHOD FOR THE ANALYSIS OF DATA MEASURED FOR SAMPLE CTS2012 - 01 IN REVERSE MODE FOR TEMPERATURE RANGE FROM 12 K UP TO 100 K	58
FIG. 6.30	ANALYTICAL METHOD FOR THE ANALYSIS OF DATA MEASURED FOR SAMPLE CTS2012 - 04 IN REVERSE MODE FOR TEMPERATURE RANGE FROM 12 K UP TO 100 K	58
FIG. 6.31	ANALYTICAL METHOD FOR THE ANALYSIS OF DATA MEASURED FOR SAMPLE MK2012 - 01 IN REVERSE MODE FOR TEMPERATURE RANGE FROM 12 K UP TO 100 K	59
FIG. 6.32	ANALYTICAL METHOD FOR THE ANALYSIS OF DATA MEASURED FOR SAMPLE MK2012 - 02 IN REVERSE MODE FOR TEMPERATURE RANGE FROM 12 K UP TO 100 K	59
FIG. 6.33	ANALYTICAL METHOD FOR THE ANALYSIS OF DATA MEASURED FOR SAMPLE MK2012 - 03 IN REVERSE MODE FOR TEMPERATURE RANGE FROM 12 K UP TO 100 K	59
FIG. 6.34	<i>I-V</i> CHARACTERISTIC FOR SAMPLE KOL2012 - 03 SAMPLE IN NORMAL MODE FOR TEMPERATURE FROM 12 K UP TO 150 K IN DETAILED VIEW	60
FIG. 6.35	<i>I-V</i> CHARACTERISTIC IN NORMAL MODE ANALYSIS FOR SAMPLE KOL2012 - 03 FOR TEMPERATURE 12 K. BLUE CURVE - MEASURED DEPENDENCE (A), RED CURVE - TRAP ASSISTED TUNNELING FROM HOMO LEVEL (B), BLACK CURVE - FOWLER-NORDHEIM TUNNELING COMPONENT (C)	60
FIG. 6.36	<i>I-V</i> CHARACTERISTIC IN NORMAL MODE ANALYSIS FOR SAMPLE KOL2012 - 03 FOR TEMPERATURE 20 K. BLUE CURVE - MEASURED DEPENDENCE (A), RED CURVE - TRAP ASSISTED TUNNELING FROM HOMO LEVEL (B), BLACK CURVE - FOWLER-NORDHEIM TUNNELING COMPONENT (C)	61
FIG. 6.37	<i>I-V</i> CHARACTERISTIC IN NORMAL MODE ANALYSIS FOR SAMPLE KOL2012 - 03 FOR TEMPERATURE 40 K. BLUE CURVE - MEASURED DEPENDENCE (A), RED	

	CURVE – TRAP ASSISTED TUNNELING FROM HOMO LEVEL (B), BLACK CURVE – FOWLER-NORDHEIM TUNNELING COMPONENT (C)_____	61
FIG. 6.38	<i>I</i> - <i>V</i> CHARACTERISTIC IN NORMAL MODE ANALYSIS FOR SAMPLE KOL2012 - 03 FOR TEMPERATURE 60 K. BLUE CURVE – MEASURED DEPENDENCE (A), RED CURVE – TRAP ASSISTED TUNNELING FROM HOMO LEVEL (B), BLACK CURVE – FOWLER-NORDHEIM TUNNELING COMPONENT (C)_____	61
FIG. 6.39	<i>I</i> - <i>V</i> CHARACTERISTIC IN NORMAL MODE ANALYSIS FOR SAMPLE KOL2012 - 03 FOR TEMPERATURE 100 K. BLUE CURVE – MEASURED DEPENDENCE (A), RED CURVE – TRAP ASSISTED TUNNELING FROM HOMO LEVEL (B), BLACK CURVE – FOWLER-NORDHEIM TUNNELING COMPONENT (C)_____	62
FIG. 6.40	<i>I</i> - <i>V</i> CHARACTERISTIC IN NORMAL MODE ANALYSIS FOR SAMPLE KOL2012 - 03 FOR TEMPERATURE 150 K. BLUE CURVE – MEASURED DEPENDENCE (A), RED CURVE – TRAP ASSISTED TUNNELING FROM HOMO LEVEL (B), BLACK CURVE – FOWLER-NORDHEIM TUNNELING COMPONENT (C)_____	62
FIG. 6.41	TRANSPARENCY OF THE BARRIER FOR ELECTRON TUNNELING VS. TEMPERATURE FOR THE SERIES KOL2012 IN NORMAL MODE IN THE TEMPERATURE RANGE FROM 12 K UP TO 150 K_____	63
FIG. 6.42	ENERGY OF THE BARRIER FOR ELECTRON TUNNELING VS. TEMPERATURE FOR THE SERIES KOL2012 IN NORMAL MODE IN THE TEMPERATURE RANGE FROM 12 K UP TO 150 K_____	64
FIG. 6.43	TRANSPARENCY OF THE BARRIER FOR ELECTRON TUNNELING VS. TEMPERATURE FOR THE SERIES CTS2012 IN NORMAL MODE IN THE TEMPERATURE RANGE FROM 12 K UP TO 150 K_____	64
FIG. 6.44	ENERGY OF THE BARRIER FOR ELECTRON TUNNELING VS. TEMPERATURE FOR THE SERIES CTS2012 IN NORMAL MODE IN THE TEMPERATURE RANGE FROM 12 K UP TO 150 K_____	65
FIG. 6.45	TRANSPARENCY OF THE BARRIER VS. TEMPERATURE FOR THE SERIES MK2012 IN NORMAL MODE IN THE TEMPERATURE RANGE FROM 12 K UP TO 150 K_____	65
FIG. 6.46	ENERGY OF THE BARRIER FOR ELECTRON TUNNELING VS. TEMPERATURE FOR THE SERIES MK2012 IN NORMAL MODE IN THE TEMPERATURE RANGE FROM 12 K UP TO 150 K_____	66
FIG. 6.47	TRANSPARENCY OF THE BARRIER VS. TEMPERATURE FOR THE SERIES KOL2012 IN REVERSE MODE IN THE TEMPERATURE RANGE FROM 12 K UP TO 100 K_____	66
FIG. 6.48	ENERGY OF THE BARRIER FOR ELECTRON TUNNELING VS. TEMPERATURE FOR THE SERIES KOL2012 IN REVERSE MODE IN THE TEMPERATURE RANGE FROM 12 K UP TO 100 K_____	67
FIG. 6.49	TRANSPARENCY OF THE BARRIER VS. TEMPERATURE FOR THE SERIES CTS2012 IN REVERSE MODE IN THE TEMPERATURE RANGE FROM 12 K UP TO 100 K_____	67
FIG. 6.50	ENERGY OF THE BARRIER FOR ELECTRON TUNNELING VS. TEMPERATURE FOR THE SERIES CTS2012 IN REVERSE MODE IN THE TEMPERATURE RANGE FROM 12 K UP TO 100 K_____	68
FIG. 6.51	TRANSPARENCY OF THE BARRIER VS. TEMPERATURE FOR THE SERIES MK2012 IN REVERSE MODE IN THE TEMPERATURE RANGE FROM 12 K UP TO 100 K_____	68

FIG. 6.52	ENERGY OF THE BARRIER FOR ELECTRON TUNNELING VS. TEMPERATURE FOR THE SERIES MK2012 IN REVERSE MODE IN THE TEMPERATURE RANGE FROM 12 K UP TO 100 K	68
FIG. 6.53	CURRENT DENSITY J VS. ELECTRIC FIELD E CHARACTERISTIC FOR SAMPLE KOL2012 - 05 FOR TEMPERATURE 12 K, 60 K AND 100 K FOR THE NORMAL MODE	69
FIG. 6.54	CURRENT DENSITY J VS. ELECTRIC FIELD E CHARACTERISTIC IN LOGARITHMIC SCALE FOR SAMPLE KOL2012 - 05 FOR TEMPERATURE 12 K AND 80 K FOR THE NORMAL MODE	69
FIG. 6.55	CURRENT DENSITY J VS. ELECTRIC FIELD E CHARACTERISTIC FOR SAMPLE CTS2012 - 01 FOR TEMPERATURE 12 K, 70 K AND 100 K FOR THE NORMAL MODE	70
FIG. 6.56	CURRENT DENSITY J VS. ELECTRIC FIELD E CHARACTERISTIC IN LOGARITHMIC SCALE FOR SAMPLE CTS2012-01 FOR TEMPERATURE 12 K, 70 K AND 100 K FOR THE NORMAL MODE	70
FIG. 6.57	CURRENT DENSITY J VS. ELECTRIC FIELD E CHARACTERISTIC FOR SAMPLE MK2012 - 01 FOR TEMPERATURE 12 K, 70 K AND 100 K FOR THE NORMAL MODE	70
FIG. 6.58	CURRENT DENSITY J VS. ELECTRIC FIELD E CHARACTERISTIC IN LOGARITHMIC SCALE FOR SAMPLE MK2012 - 01 FOR TEMPERATURE 12 K, 70 K AND 100 K FOR THE NORMAL MODE	71
FIG. 6.59	POOLE-FRENKEL PLOT FOR THE SAMPLE CTS2012 - 01 FOR THE TEMPERATURE 150 K	72
FIG. 6.60	POOLE-FRENKEL PLOT FOR THE SAMPLE CTS2012 - 04 FOR THE TEMPERATURE 150 K	72
FIG. 6.61	POOLE-FRENKEL PLOT FOR THE SAMPLE MK2012 - 01 FOR THE TEMPERATURES 100 K, 150 K AND 250 K	73
FIG. 6.62	SCHOTTKY PLOT FOR THE SAMPLE KOL2012 - 05 FOR TEMPERATURE 150 K	74
FIG. 6.63	SCHOTTKY PLOT FOR THE SAMPLE CTS2012 - 01 FOR TEMPERATURE 150 K	74
FIG. 6.64	SCHOTTKY PLOT FOR THE SAMPLE CTS2012 - 04 FOR TEMPERATURE 150 K	74
FIG. 6.65	SCHOTTKY PLOT FOR THE SAMPLE MK2012 - 01 FOR TEMPERATURES 150 K AND 100 K	75
FIG. 6.66	FOWLER-NORDHEIM PLOT IN NORMAL MODE FOR THE SAMPLE KOL2012 - 02 FOR THE TEMPERATURES 12 K, 60 K AND 100 K	75
FIG. 6.67	FOWLER-NORDHEIM PLOT IN NORMAL MODE FOR THE SAMPLE KOL2012 - 03 FOR THE TEMPERATURES 12 K, 60 K AND 100 K	76
FIG. 6.68	FOWLER-NORDHEIM PLOT IN NORMAL MODE FOR THE SAMPLE KOL2012 - 05 FOR THE TEMPERATURES 12 K, 60 K AND 100 K	76
FIG. 6.69	FOWLER-NORDHEIM PLOT IN NORMAL MODE FOR THE SAMPLE CTS2012 - 01 FOR THE TEMPERATURES 12 K, 70 K AND 100 K	77
FIG. 6.70	FOWLER-NORDHEIM PLOT IN NORMAL MODE FOR THE SAMPLE CTS2012 - 04 FOR THE TEMPERATURES 12 K, 70 K AND 100 K	77
FIG. 6.71	FOWLER-NORDHEIM PLOT IN NORMAL MODE FOR THE SAMPLE MK2012-01 FOR THE TEMPERATURES 12 K, 70 K AND 100 K	78
FIG. 6.72	FOWLER-NORDHEIM PLOT IN NORMAL MODE FOR THE SAMPLE MK2012-02 FOR THE TEMPERATURES 12 K, 70 K AND 100 K	78

FIG. 6.73	FOWLER-NORDHEIM PLOT IN NORMAL MODE FOR THE SAMPLE MK2012-03 FOR THE TEMPERATURES 12 K, 70 K AND 100 K	78
FIG. 6.74	FOWLER-NORDHEIM PLOT IN REVERSE MODE FOR THE SAMPLE KOL2012 – 02 FOR THE TEMPERATURES 12 K, 60 K AND 80 K	79
FIG. 6.75	FOWLER-NORDHEIM PLOT IN REVERSE MODE FOR THE SAMPLE KOL2012 – 03 FOR THE TEMPERATURES 12 K, 60 K AND 80 K	79
FIG. 6.76	FOWLER-NORDHEIM PLOT IN REVERSE MODE FOR THE SAMPLE KOL2012 – 05 FOR THE TEMPERATURES 12 K, 60 K AND 80 K	80
FIG. 6.77	FOWLER-NORDHEIM PLOT IN REVERSE MODE FOR THE SAMPLE CTS2012-01 FOR THE TEMPERATURES 12 K, 40 K AND 70 K	80
FIG. 6.78	FOWLER-NORDHEIM PLOT IN REVERSE MODE FOR THE SAMPLE CTS2012-04 FOR THE TEMPERATURES 12 K, 40 K AND 70 K	80
FIG. 6.79	FOWLER-NORDHEIM PLOT IN REVERSE MODE FOR THE SAMPLE MK2012-01 FOR THE TEMPERATURES 12 K, 50 K AND 70 K	81
FIG. 6.80	FOWLER-NORDHEIM PLOT IN REVERSE MODE FOR THE SAMPLE MK2012-02 FOR THE TEMPERATURES 12 K, 50 K AND 70 K	81
FIG. 6.81	FOWLER-NORDHEIM PLOT IN REVERSE MODE FOR THE SAMPLE MK2012-03 FOR THE TEMPERATURES 12 K, 50 K AND 70 K	82
FIG. 6.82	$I - V$ CHARACTERISTIC IN REVERSE MODE IN SEMI-LOGARITHMIC SCALE WITH LINEAR APPROXIMATION FOR THE THERMIONIC EMISSION CURRENT COMPONENT ANALYSIS FOR SAMPLE KOL2012 – 02 FOR TEMPERATURES 100 K, 150 K AND 200 K	82
FIG. 6.83	THERMIONIC EMISSION CURRENT CONSTANT I_0 VS. TEMPERATURE (LEFT) AND THERMIONIC EMISSION CURRENT CONSTANT VS. $1000/T$ (RIGHT) FOR SAMPLE KOL2012 – 02	83
FIG. 6.84	$I - V$ CHARACTERISTIC IN REVERSE MODE IN SEMI-LOGARITHMIC SCALE WITH LINEAR APPROXIMATION FOR THE THERMIONIC EMISSION CURRENT COMPONENT ANALYSIS FOR SAMPLES KOL2012–03 AND 05 FOR TEMPERATURES 100 K, 150 K AND 200 K	83
FIG. 6.85	$I - V$ CHARACTERISTIC IN REVERSE MODE IN SEMI-LOGARITHMIC SCALE WITH LINEAR APPROXIMATION FOR THE THERMIONIC EMISSION CURRENT COMPONENT ANALYSIS FOR SAMPLES CTS2012 – 01 AND 04 FOR TEMPERATURES 100 K, 150 K AND 200 K	84
FIG. 6.86	$I - V$ CHARACTERISTIC IN REVERSE MODE IN SEMI-LOGARITHMIC SCALE WITH LINEAR APPROXIMATION FOR THE THERMIONIC EMISSION CURRENT COMPONENT ANALYSIS FOR SAMPLES MK2012 – 01 AND 02 FOR TEMPERATURES 100 K, 150 K AND 200 K	85
FIG. 6.87	CURRENT DENSITY (LOG J) VS. ELECTRIC FIELD (LOG E) FOR SAMPLE KOL2012 – 03 FOR REVERSE MODE AT TEMPERATURES 12 K (LEFT) AND 80 K (RIGHT)	87
FIG. 6.88	CURRENT DENSITY (LOG J) VS. ELECTRIC FIELD (LOG E) FOR SAMPLE KOL2012 – 05 IN NORMAL MODE AND IN REVERSE MODE AT TEMPERATURE 12 K	87
FIG. 6.89	CURRENT DENSITY (LOG J) VS. ELECTRIC FIELD (LOG E) FOR SAMPLE KOL2012 – 05 IN NORMAL MODE AT TEMPERATURES 20 K AND 30 K	88
FIG. 6.90	CURRENT DENSITY (LOG J) VS. ELECTRIC FIELD (LOG E) FOR SAMPLE KOL2012 – 05 IN NORMAL MODE AND IN REVERSE MODE AT TEMPERATURE 60 K	89

FIG. 6.91	CURRENT DENSITY (LOG J) VS. ELECTRIC FIELD (LOG E) FOR SAMPLE MK2012 – 02 IN NORMAL MODE FOR TEMPERATURE 12 K AND 150 K _____	89
FIG. 6.92	CURRENT DENSITY (LOG J) VS. ELECTRIC FIELD (LOG E) FOR SAMPLE CTS2012 – 04 IN NORMAL MODE FOR TEMPERATURE 20 K, 200 K AND 250 K _____	89
FIG. 7.1	DONOR CONCENTRATION N_D VS. DIFFUSE VOLTAGE U_D FOR ALL SERIES AND SELECTED SAMPLES FOR TEMPERATURE 300 K _____	90
FIG. 7.2	DONOR CONCENTRATION FOR DIFFERENT TEMPERATURES FOR SAMPLES CTS2012 – 01, CTS2012 – 03, CTS2012 – 05 _____	90
FIG. 7.3	DIFFUSE VOLTAGE U_D VS. DIFFERENT TEMPERATURES FOR SERIES CTS2012 _____	91
FIG. 7.4	U_T TUNNELING PARAMETER VS. TEMPERATURE FROM THE ANALYTICAL METHOD IN NORMAL MODE FOR THE TEMPERATURE RANGE FROM 12 K UP TO 150 K IN NORMAL MODE _____	92
FIG. 7.5	E_T AND U_T TUNNELING PARAMETERS VS. TEMPERATURE FROM THE GRAPHICAL METHOD IN NORMAL MODE FOR THE TEMPERATURE RANGE FROM 12 K UP TO 150 K IN NORMAL MODE _____	92
FIG. 7.6	COMPARISON OF THE POTENTIAL BARRIER HEIGHT FROM THE ANALYTICAL METHOD AND GRAPHICAL METHOD, DEPENDENCE OF THE POTENTIAL BARRIER ON THE CATHODE SIDE VS. TEMPERATURE FROM 12 K UP TO 150 K IN NORMAL MODE _____	93
FIG. 7.7	U_T TUNNELING PARAMETER VS. TEMPERATURE FROM THE ANALYTICAL METHOD IN REVERSE MODE FOR THE TEMPERATURE RANGE FROM 12 K UP TO 200 K IN NORMAL MODE _____	94
FIG. 7.8	E_T AND U_T TUNNELING PARAMETERS VS. TEMPERATURE FROM THE GRAPHICAL METHOD IN REVERSE MODE FOR THE TEMPERATURE RANGE FROM 12 K UP TO 150 K IN NORMAL MODE _____	94
FIG. 7.9	COMPARISON OF THE POTENTIAL BARRIER HEIGHT FROM THE ANALYTICAL METHOD AND GRAPHICAL METHOD, DEPENDENCE OF THE POTENTIAL BARRIER ON THE CATHODE SIDE VS. TEMPERATURE FROM 12 K UP TO 150 K IN REVERSE MODE _____	97
FIG. 7.10	COMPARISON OF THE POTENTIAL BARRIER HEIGHT ON THE ANODE SIDE FROM THE ANALYTICAL METHOD AND GRAPHICAL METHOD, DEPENDENCE OF THE POTENTIAL BARRIER VS. TEMPERATURE FROM 12 K UP TO 150 K FOR SAMPLES OF SERIES KOL2012 _____	95
FIG. 7.11	COMPARISON OF THE POTENTIAL BARRIER HEIGHT ON THE ANODE SIDE FROM THE ANALYTICAL METHOD AND GRAPHICAL METHOD, DEPENDENCE OF THE POTENTIAL BARRIER VS. TEMPERATURE FROM 12 K UP TO 150 K FOR SAMPLES OF SERIES CTS2012 _____	95
FIG. 7.12	COMPARISON OF THE POTENTIAL BARRIER HEIGHT ON THE ANODE SIDE FROM THE ANALYTICAL METHOD AND GRAPHICAL METHOD, DEPENDENCE OF THE POTENTIAL BARRIER VS. TEMPERATURE FROM 12 K UP TO 150 K FOR SAMPLES OF SERIES MK2012 _____	96

FIG. 7.13 CHANGE OF ENERGY BAND STRUCTURE IN THE MIS MODEL FOR TANTALUM CAPACITOR: A) TRIANGULAR POTENTIAL BARRIER FOR FOWLER-NORDHEIM TUNNELING; B) DECREASE OF POTENTIAL BARRIER WIDTH FOR ELECTRON TUNNELING DUE TO THE BAND-BENDING; C) INCREASE OF POTENTIAL BARRIER HEIGHT DUE TO THE SHIFT OF FERMI LEVEL WITH TEMPERATURE – FERMI LEVEL DRAW CLOSER TO THE DONOR ENERGY BAND _____ 96

List of tables

TAB. 1.	ANODIZATION COEFFICIENTS FOR DIFFERENT ELECTROLYTES FOR TANTALUM CAPACITORS [16]	9
TAB. 2.	BASIC DESCRIPTION OF THE SAMPLES FROM MANUFACTORY	35
TAB. 3.	CALCULATED PARAMETERS FROM MEASURING	36
TAB. 4.	THEORETICAL VALUES OF POOLE-FRENKEL COEFFICIENT FOR DIFFERENT TEMPERATURES, THEORETICAL VALUES OF THE SLOPE OF LINEAR APPROXIMATION IN PF PLOT MPF(THEORY) AND EXPERIMENTALLY OBTAINED VALUES THE SLOPE OF LINEAR APPROXIMATION MPF(MEASURED) IN NORMAL MODE FOR SAMPLE KOL2012 – 05	71
TAB. 5.	VALUES OF M, BTE AND IDEALITY FACTOR N CALCULATED FOR SAMPLE KOL2012 – 02 FOR TEMPERATURES 100 K, 150 K AND 200 K	83
TAB. 6.	VALUES OF M, BTE AND IDEALITY FACTOR N CALCULATED FOR SAMPLE KOL2012 – 03 FOR TEMPERATURES 100 K, 150 K AND 200 K	84
TAB. 7.	VALUES OF M, BTE AND IDEALITY FACTOR N CALCULATED FOR SAMPLE KOL2012 – 05 FOR TEMPERATURES 100 K, 150 K AND 200 K	84
TAB. 8.	VALUES OF M, BTE AND IDEALITY FACTOR N CALCULATED FOR SAMPLE CTS2012 – 01 FOR TEMPERATURES 100 K, 150 K AND 200 K	85
TAB. 9.	VALUES OF M, BTE AND IDEALITY FACTOR N CALCULATED FOR SAMPLE CTS2012 – 04 FOR TEMPERATURES 100 K, 150 K AND 200 K	85
TAB. 10.	VALUES OF M, BTE AND IDEALITY FACTOR N CALCULATED FOR SAMPLE MK2012 – 01 FOR TEMPERATURES 100 K, 150 K AND 200 K	86
TAB. 11.	VALUES OF M, BTE AND IDEALITY FACTOR N CALCULATED FOR SAMPLE MK2012 – 02 FOR TEMPERATURES 100 K, 150 K AND 200 K	86
TAB. 12.	MOBILITY OF CHARGE CARRIERS μ FOR SAMPLE KOL2012 – 03 FOR REVERSE MODE AT TEMPERATURES 12 K AND FOR SAMPLE KOL2012 – 05 FOR NORMAL MODE AT DIFFERENT TEMPERATURES	88
TAB. 13.	CHARGE TRANSPORT MECHANISMS SUMMARY IN NORMAL MODE	98
TAB. 14.	CHARGE TRANSPORT MECHANISMS SUMMARY IN REVERSE MODE	98

List of used symbols

<i>DCL</i>	Direct current leakage
<i>ESR</i>	Equivalent series resistance
<i>ESL</i>	Equivalent series inductance
<i>CP</i>	Conductive polymer
W_{CP}	Work function for conductive polymer
<i>ECDL</i>	Electrochemical double layer capacitors
<i>SMD</i>	Surface mount device
<i>d</i>	Weight of the conductive connection between two particles, The thickness of dielectric layer
<i>a</i>	Anodization coefficient
U_f	Forming voltage
<i>SEM</i>	Scanning electron microscope
<i>MIS</i>	Metal-Insulator-Semiconufactor
I_0	Constant dependent on concentration of uncompensated bonds at the oxide surface
N_D	Donor concentration
<i>c</i>	Electron affinity
eF_S	Potential barrier between Nb_2O_5 and MnO_2
<i>Q</i>	Elementary charge
<i>C</i>	Capacitance
<i>V</i>	Voltage
ϵ_0	Dielectric constant for vacuum, permittivity of vacuum
ϵ_r	Relative permittivity
<i>A</i>	Active surface area
W_M	Work function of tantalum
c_i	Ta_2O_5 electron affinity
W_{MnO_2}	Work function for the manganese dioxide MnO_2
E_F	Fermi level energy
E_{CI}	Conducting band energy in insulator layer Ta_2O_5
E_{VI}	Valence band energy in insulator layer Ta_2O_5
E_D	Donor energy band in insulator layer Ta_2O_5
E_{CS}	Conducting band energy in semiconductor layer MnO_2
E_{VS}	Valence band energy in the semiconductor layer MnO_2
<i>HOMO</i>	Highest occupied molecular orbital
<i>LUMO</i>	Lowest unoccupied molecular orbital
ef_{M1}	Energy barrier on the interface between tantalum and insulating layer Ta_2O_5
ef_{IS}	Energy barrier on the interface between insulator layer Ta_2O_5 and semiconductor MnO_2
E_g	Forbidden energy gap value
E_d	Electric field strength
DE_{imp}	Impurity band width
DF_{PF}	Rice of potential barrier lowering
J_{SC}	Space charge limited current density

G_{Ω}	Ohmic conductivity
m	Mobility of charge carriers
m_0	Parameter of electron mobility
E_a	Activation energy
ΔF	Reduction of the potential barrier
G_{PF}	Poole-Frenkel conductivity
β_{PF}	Poole-Frenkel coefficient
β_{TE}	Thermionic emission parameter
e	Elementary charge
k	Boltzmann constant
T	Thermodynamic temperature
ΔF_{PF}	Decreasing of the potential barrier by Poole-Frenkel phenomena
E	Electric field
D	Tunneling probability
D_0	Tunneling probability constant
t_0	Tunneling layer thickness
m_{ef}	Effective electron mass
h	Planck constant
F_0	Barrier energy
eF_c	Barrier on the cathode side
λ	Electron wave length
m^*	Effective electron mass
m_0	Electron rest mass
π	Mathematical constant
A	Effective area of electrodes
R	Richardson constant
v_{ds}	Thermal velocity
V_f	Forming voltage

1. Introduction

The first tantalum capacitor was produced and marketed in 1930 by Fansteel USA. Significant improvements in technology and expansion of capacitance and voltage ranges were shown during WWII. New producers entered the market – General Electric Company (USA), Siemens und Halske (Ger.), Electrometallurgy (Ger.) and Murex Limited (UK). During the late 1940s, Fansteel developed a sub-miniature, porous-slug type tantalum capacitor in conjunction with Bell Laboratories and the U.S. Air Force. During the late 1950's and early 1960's, a solid counter electrolyte was developed in the form of manganese dioxide for use in slug-type tantalum capacitors. This represented a technical breakthrough that virtually eliminated the disadvantages and use of the gelled sulfuric acid electrolyte. In the early 1960's, anode weights of 1 to 5 grams were common. Today the average anode weight across all production is 50 to 55 mg with the smallest anode weighing about 0.5 mg and dimensionally less than 1 mm in any plane. This opened up new opportunities for tantalum capacitors and their characteristics of high reliability, long life, wide temperature range with minimal change in performance, low leakage current DCL, and occupation of 'small real estate' on a circuit board in comparison with alternative technologies. The evolutions of capacitors have continued very rapidly and many manufactures focused in this area and developed new materials, structures and applied it in the many electronic devices [1-6].

To improve quality and reliability of tantalum capacitors the nondestructive testing methods were used. These methods are based on measurements of current-voltage (I - V), capacitance - voltage (C - V), capacitance - temperature (C - T), and current - time (I - t) dependences. Investigation of capacitors in the wide temperature range was provided to analyze the dependence of DCL components on temperature, i.e. contribution of ohmic current component, Poole-Frenkel, Schottky and tunneling current components to the total DCL value.

The growing of the dielectric Ta₂O₅ layer by anodic oxidation was tuned to prepare amorphous insulating layer with low concentration of interstitial and oxygen vacancies. It was founded that parameters of anodic oxidation as current density of anodization current or used electrolyte, respectively, determine the electron affinity and concentration of oxygen vacancies in insulating layer. Electron affinity of Ta₂O₅ increases with anodization current density which leads to decrease of potential barriers between Ta- Ta₂O₅ and Ta₂O₅ - cathode, respectively. Very low anodization current density can lead to the creation of nano and micro crystalline structures which can be source of field crystallization [7-8].

For application of tantalum capacitors an important parameter is equivalent series resistance (ESR). From this point of view the manganese dioxide (MnO₂) cathode was replaced by conducting polymer (CP) which has higher conductivity. However new issues have appeared the P-N structure is part of electron-band structure of capacitors. While manganese dioxide is N-type semiconductor with work function value $W_{\text{MnO}_2} = 5,6$ eV, the conducting polymer is P-type structure with work function value about $W_{\text{CP}} = 5$ eV only. Then CP creates lower potential barrier between cathode and insulating layer and then this is a source of higher leakage current. Potential barrier between insulating layer and cathode determined ohmic current component, Poole-Frenkel and tunneling current component. The technology of tantalum capacitors is oriented to increase of this potential barrier, e.g. by dipole layer with proper orientation of dipoles. Interface between insulating layer and cathode contents high

density of electronic states and then during the ageing their concentration can be changed and leakage current can increase or decrease with the time of ageing [8-11].

The investigation of leakage current behavior in the wide temperature range shows, that the temperature dependent charge carriers' transport components as Poole-Frenkel and Schottky current component play important role at the temperatures above 150 K while tunneling of charge carriers becomes dominant in the low temperature range, where the thermally activated over barrier current components are negligible. Tunneling current component is considered to be temperature independent however the experiments performed on tantalum capacitors for the temperatures below 100 K show, that the tunneling current increases with decreasing temperature in the range 100 K to 50 K, while slightly increases in the range 50 to 10 K [11]. Detail study of this issue will be given in this thesis.

2. State of Art

2.1. Tantalum capacitors

In this chapter I present the overview of Ta capacitor production, the basic model for the tantalum capacitor and present research of the tantalum capacitors.

The present capacitors are very different electronics devices and in comparison with the historical types still consist of two electrodes, anode and cathode, and insulator placed in between these electrodes. There are many types of capacitors - electrostatic, electrolytic or electrochemical in the market. The electrostatic capacitors are based on a dielectric film between two metal electrodes. The principal types have a ceramic or plastic (film) dielectric. Types that are more specialized are based on silicon (for RF), mica, porcelain, and glass dielectrics. The electrochemical capacitors are very often called as double layer capacitors, supercapacitors, ultracapacitors, or electrochemical double layer capacitors (ECDL) [12]. It consists of two conducting electrodes separated by an electrolyte. A very thin layer of solvent molecules acts as the dielectric between the charge on the electrode and the charged ions in solution. This electrical double layer can have huge capacitances 10 $\mu\text{F}/\text{cm}^2$. In addition, some surface oxidation-reduction reactions may contribute to charge transfer and, therefore to capacitance (called pseudocapacitance). To maximize the capacitance, the electrodes are made of high surface area materials like activated carbon. The next type of capacitors are electrolytic capacitors, amount then the most common are aluminum, niobium-based and tantalum-based capacitors. There were many permutations of electrode systems and in the meantime there are used MnO₂ and conductive polymers instead of liquid electrolytes [12].

First, the electrodes were made of the same material (symmetric type). More recently, asymmetric types have been developed. In asymmetric devices, the two electrodes are made from different materials. After discovering the porous tantalum anode has been Ta electrolytic capacitors became much better comparing with classical aluminum electrolyte capacitor. The main advantages are high dielectric constant of Ta₂O₅, high dielectric stability and reliability but there are some limitation as high volume of case, the case is important to seal up and protected before leakage of electrolytic liquid, and many others undesirable phenomenon [12].

As was mentioned market needs better properties for the capacitors. The main benefit for the tantalum capacitors is the capacitance per unit volume. These capacitors have very high volumetric efficiencies. It is caused by very good electrical properties of tantalum powder and manufacturing processes of dielectric layer created by anodic oxidation. These capacitors are distinguished by very good quality, reliability, very low ESR, equivalent series inductance ESL and wide temperature range, and also comply require for Pb-free solders. These capacitors with the tantalum pentoxide are polar devices. The first tantalum capacitors with a solid electrolyte MnO₂ were produced in Lanškroun already in 1966 as one of the first worldwide. Mass manufacturing of these capacitors however started later in 1971 due to the high investment cost. TESLA Lanškroun became one of the main passive component suppliers in middle and Eastern Europe (former East Bloc) at that time. SMD chip type tantalum capacitors were developed in TESLA at the beginning of the 1980's, however mass manufacturing had not been implemented. Lack of high quality materials, limited material base from the Eastern bloc countries and/or inaccessibility to high technology equipment's from Western countries was prevalent throughout the 80's [12, 13]. Tantalum capacitors are used across all product

segments in the areas of bypass, decoupling, and filtering. The producers are able to provide the various classes of tantalum capacitors with guaranteed failure rate are available for military, aerospace, and implantable medical use.

The most of manufactures have focused on continuing to increase volumetric efficiency and downsizing, so the same capacitance fits a smaller case size. The volumetric efficiency is proportional to usage of different types of the tantalum powder. The research and developing the new tantalum powder is next topic for increasing volumetric efficiency of capacitors. New trends in packaging techniques also contribute to higher volumetric efficiency. Fig. 2.1 shows the standard molded case construction for tantalum capacitors and a relatively new „facedown” terminal construction for molded cases [10]. There are lead frames as contacts for the cathode and anode. Inside the capacitor there is pellet. Pellet is a pressed tantalum powder which is connected with the contacts by tantalum wire.

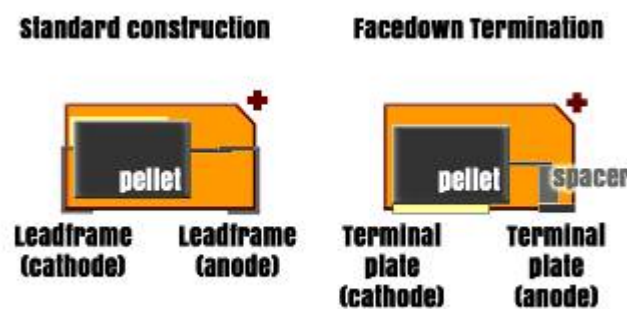


Fig. 2.1 Facedown construction in tantalum capacitors with the terminals

These two types of cases construction make for a more efficient use of the volume in the molded case and allow for the use of a larger tantalum anode. There are other solutions offered by different vendors which also offer improved volumetric efficiency. Chart in Fig. 2.2 shows the gain in percentages of the package utilized in going from a standard to face down termination configuration.

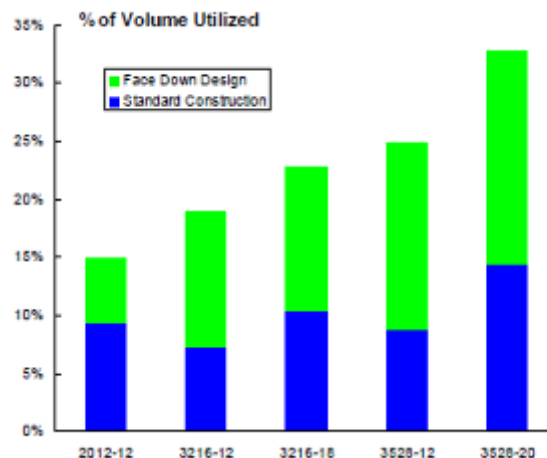


Fig. 2.2 Small case standard vs. facedown [12]

Conformal-coated devices are the best efficiency for tantalum capacitors, there is a thin layer of resin which is coated on the active element. These capacitors are used in the application with the highest capacitance and voltage. The development of extension from the maximum temperature range is a discussed issue and a typical operation temperature is 125 °C. For special types of capacitors with manganese dioxide cathode or conductive polymer cathode is the temperature up to 150 °C. From 2006 there are available new types for automotive industry with operation temperature 175 °C, and new types with wet cathodes up to 200 °C.

In 1994 were tested first conductive polymers with a polypyrrole backbone in the tantalum capacitors. Latest capacitors have begun use these materials. However, main advantages of the organic polymer types compared to the manganese dioxide type are lower ESR, surge robustness, and a non-ignition failure mode. They looked like ideal capacitors, but there were problems with higher cost, higher leakage current, a restricted voltage range, greater sensitivity to reflow soldering conditions, and a reduced maximum temperature of use. In early 2008, devices in these footprints with ESR's of 15 mΩ are in mass production and sub 10 mΩ devices are beginning to be sampled [12]. Tantalum capacitors with lower ESL are also becoming more widely commercially available. This is driven by decoupling requirements for microprocessors and the desire to eliminate some of the ceramic capacitors used. In the last years the producers many of these problems eliminate. Tantalum-polymer capacitors can be used for multiple reflows at Pb-free conditions and operation temperature has been changed up to 125 °C. However, there are many key technical challenges to be solved in the future [12].

The characterization of the tantalum capacitors is important for next usage of these devices. Tantalum capacitor consists of three layers; Ta metal, Ta₂O₅insulator and MnO₂ or CP semiconductor. This structure is described in many publications as MIS structure. The transport of the charge inside this MIS structure has several transport mechanisms. There mechanisms are Ohmic transport, Schottky, Poole-Frenkel and tunneling mechanisms. The all transport mechanisms are temperature dependent and this dependence is the main goal of this thesis especially for the lower temperatures for the aerospace applications. The identification of charge transport mechanism can be done on the base of I-V characteristic analysis.

2.2. Technology of tantalum capacitors

2.2.1. Tantalum anode creation

Tantalum metal powder, including the precursor to capacitor grade powder, is generally produced by the sodium reduction of the potassium tantalum fluoride in a molten salt system at high temperature. The metal can also be produced by the carbon or aluminum reduction of the oxide or the hydrogen or alkaline earth reduction of tantalum chloride. The choice of process is based on the specific application and whether the resultant tantalum will be further consolidated by processing into ingot, sheet, rod, tubing, wire and other fabricated articles. The tantalum powder is made by morphology with applied high temperature and producers have many various types of these particles for example choral or granules type and various sizes see in Fig. 2.3. Tantalum powders with charges of 150,000 $\mu\text{FV/g}$ were used from 2006. However, the particles with charges of 200,000 $\mu\text{FV/g}$ are becoming available. The particle sizes are available typically from 10 nm. The bigger particles are used for the high-voltage capacitors and the smaller particles for the others [14, 15].

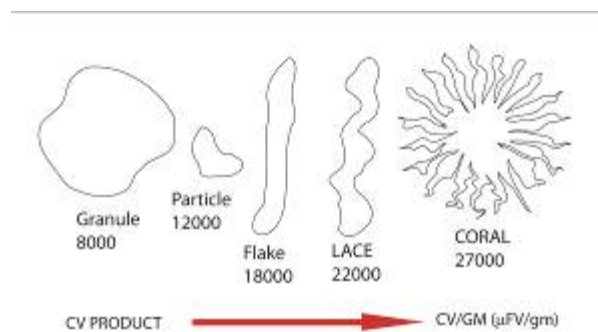


Fig. 2.3 Various types of Tantalum powder

The chronological technical process of manufactory begins with the tantalum powder and finds a suitable type of particles of powder for given application. The powder particles are mixed with eligible binder and subsequently pressed on the tantalum wire. The particles of the tantalum powder were pressed into the pellet on the tantalum wire.

The capacity is proportional to the surface volume of anode. It is possible to say with regards of experience in the manufactory that tantalum powder with bigger particles is used for capacitors with high rated voltage usually up to 50 V and vice versa. The process of pressing and sinteration is shown in Fig. 2.4. The particles were described in previous chapter. The process of pressing particles on the anode is shown in the Fig. 2.5.

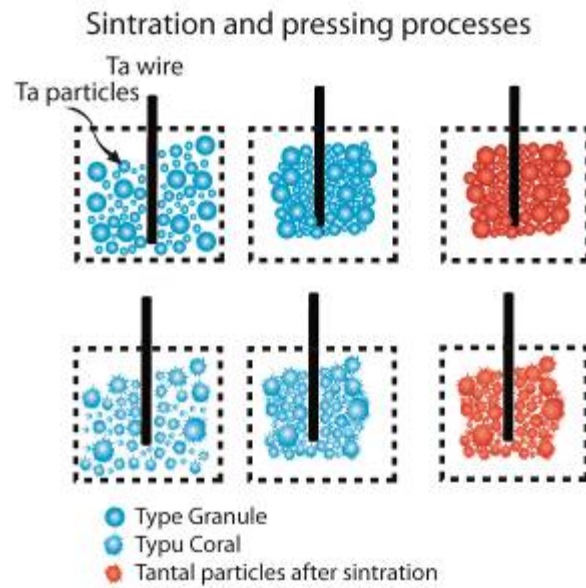


Fig. 2.4 Pressing tantalum powder and sinteration process of anode

With high temperature from 1500 °C to 2000 °C the sinteration is applied. This process leads to the creation of conductive contacts among the grains of powder and helps to clear all dirties in tantalum powder from previous pressing on the anode with the ongoing chemical reactions. The Fig. 2.5 shows the connection between two different types as was mentioned before of the tantalum particles. Type granule has smaller capacity than rough surface of Coral type. The d means the weight of the conductive connection between two particles [15, 16].

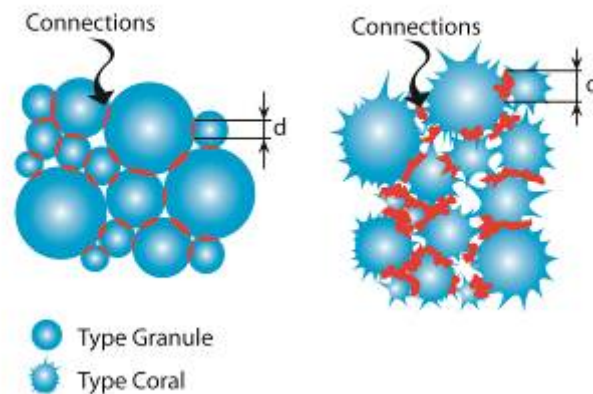


Fig. 2.5 Structure of tantalum particles and connections after sinteration process

The sinteration also causes the mechanical connection between the particles and new strong porous structure is created. The connection between the tantalum wire and pressed particles is now ready for the next process of dielectric layer creating. The time of sinteration has an important role on the on the particle connection, longer process leads to the high compactness and this corresponds to decrease of the capacity of capacitor. On the other hand when the sinteration is applied for a short time the particles have small compactness and the reliability will be low in this case.

2.2.2. Ta₂O₅ dielectric layer forming

The forming process, also called anodic oxidation, is applied as next step of creating tantalum capacitor. Tantalum wire with pressed anode is putted into the low concentration acid (e.g. phosphoric acid) and it is dipped for a defined time with applied higher temperature at 85 °C. The acid gets to around all small pressed particles. Subsequently is applied voltage between the acid and anode. This process is called anodic oxidation of anode and it caused growing of the dielectric layer of Ta₂O₅. Growing is caused due to the acid motion of oxygen's ions in the crystalloid grid and with applied electric field these ions caused the growing of dielectric layer. The time is proportional with the size of dielectric layer as insulator. The amorphous structure of Ta₂O₅ is created on the surface of anode.

The thickness of dielectric layer d is possible to calculate from the equation.

$$d = a \cdot U_f \quad (2.1)$$

where d is dielectric thickness in meters, a is anodization coefficient with value dependent on forming acid in m.V^{-1} and U_f is forming voltage in Volts. Fig. 2.6 shows the real image from SEM after the forming process. There is surface of the dielectric layer and description of the individual parts on the right side [16, 17].

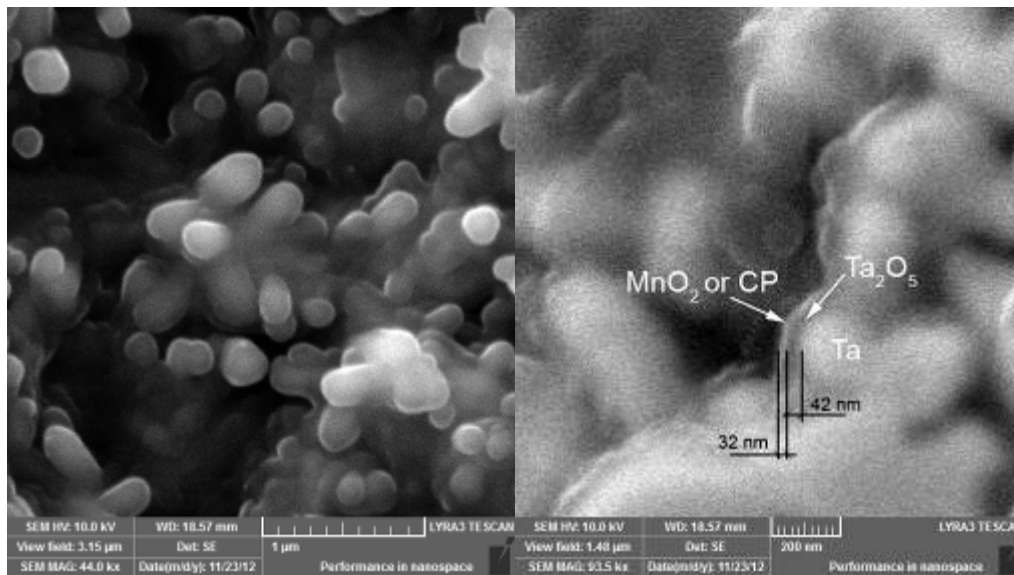


Fig. 2.6 SEM picture of the layers inside the capacitors and description of fragments Ta₂O₅ of anode

In principal of the forming of the dielectric layer is applied constant current throw the structure in the acid and when is U_f reached then the current throw the structure flow down to the minimal level and the low leakage current is reached also. Fig. 2.7 show the graph with the curve for the voltage and curve for the current (which is constant and after reach some point falling down), respectively.

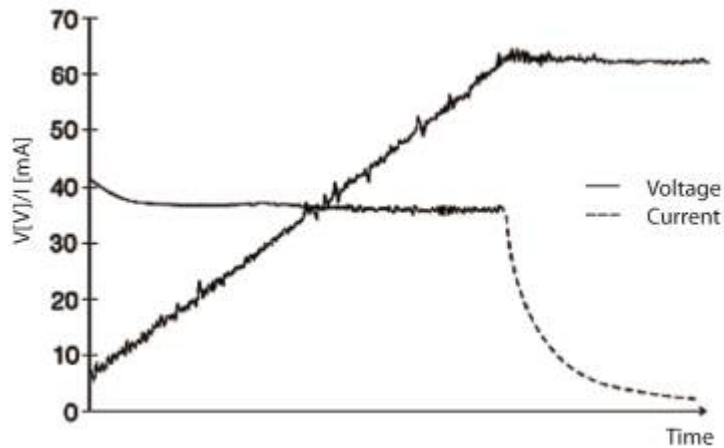


Fig. 2.7 Forming voltage and forming current dependence on time [16]

The principal scheme of the electrochemical reaction is shown in Fig. 2.8. There is chemical reaction described with equation 2.1. The tantalum wire is dipped into the bath with acid and high voltage is applied.

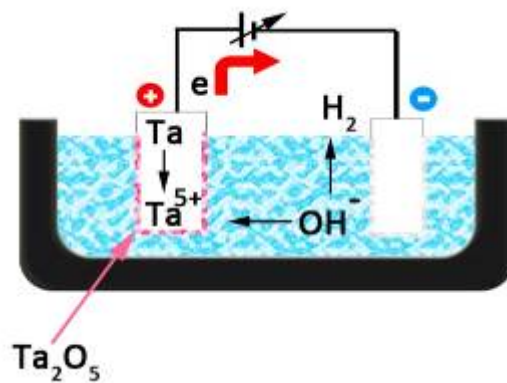


Fig. 2.8 The electrochemical reaction of the growing dielectric layer

The anodization in H₃PO₄ electrolyte results in an average value of the anodization coefficient: For tantalum capacitors is $a = 1.5 \text{ nm.V}^{-1}$. Anodization coefficient determined for different electrolytes for Ta₂O₅ creation is shown in Tab. 1

Tab. 1. Anodization coefficients for different electrolytes for tantalum capacitors [16]

Anodization coefficient a / nmV^{-1}	
Electrolyte	Ta/Ta ₂ O ₅
H ₂ SO ₄	1.54
HNO ₃	1.50
H ₃ PO ₄	1.42
NaOH	1.65

The growing speeds of the dielectric layer strongly influence the electron affinity. The potential barrier between the semiconductor – insulator and insulator – metal will be changed in this reason in the considered MIS model. The MIS model is described in the separate chapter. The dielectric thickness is possible to estimate according to the color of formatted anode. The porous structure caused the diffraction of light on the surface of anode.

Growing of the oxide layer is caused by transport of ions motion during anodic oxidation process. Ionic motion is due to interstitial and vacancy mechanism [16]. Oxides of valve metals have mixed ionic-covalent bond where the portion of covalent bond is relatively high. It was deduced that in such cases oxide is created in an amorphous form with three-dimensional disordered lattice. Such bond interruptions can be understood as single charged defects. Each atom is allowed to shift at one interatomic distance only. Metal oxide transition region was observed experimentally and the thickness of is about 2 nm [16]. Potential distribution near the oxide-electrolyte interface is illustrated in Fig. 2.9.

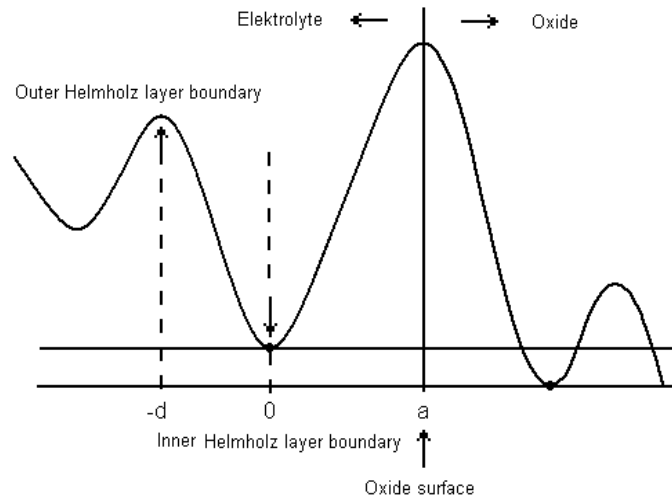


Fig. 2.9 Potential barriers in the system oxide-electrolyte [16]

The oxide chemisorption's have big influence on the electric current during the anodic oxidation processes. This current can be expressed as:

$$I = I_0 \exp\left\{-\frac{eW - (edE_d + eaE_a)}{kT}\right\} \quad (2.2)$$

Where I_0 is constant dependent on concentration of uncompensated bonds at the oxide surface which act as absorption centers, W is potential barrier at the oxide surface, a and d are shown in the Fig. 2.10, E_d and E_a is electric field strength at point d and a respectively. It was published for the system Ta – Ta₂O₅ – electrolyte $a = 0.2$ nm, and $d = 0.4$ nm. E_d and E_a can be found from the relation:

$$e_{ox} E_{0x} = e_a E_a = e_d E_d \quad (2.3)$$

Where ϵ_{ox} is oxide relative permittivity, $\epsilon_a = \epsilon_{ox}$, and according to mechanism [16] $\epsilon_d = 7$. During anodic oxidation the applied electric field is superimposed on the internal electric field of

Helmholtz and Ta₂O₅ layers. It was found that the additional electric field created by chemisorbed oxygen ions decreases the external field, which determines defect transport into oxide. Forming electrolyte has some influence on the density of the oxide layer formed by anodizing. This can be interpreted by assuming that some electrolyte has been built in [7, 8 and 15].

The mentioned amorphous oxide films are characterized by the presence of plenty of various imperfections, stoichiometric, structural defects, traps and other defects. From the measuring of the donor concentration is of the order $N_D = 10^{17}$ to 10^{19} cm⁻³. This concentration can be obtained from the capacity measuring. For value of the N_D higher than 10^{18} cm⁻³ the impurity band is created [16, 17, 18-20]. The mechanisms of charge transport through the oxide layer are directly related for the donor concentration. Fig. 2.10 shows the I - V dependences in reverse mode (positive potential on the cathode side) for NbO capacitors with identical anode which differs in the anodization current density, we can see that with decreasing current density DCL decreases [18-20].

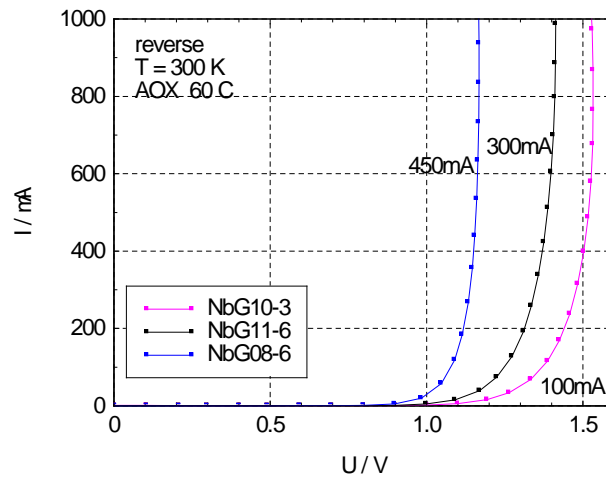
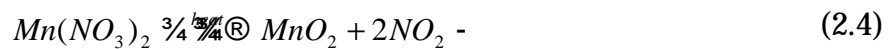


Fig. 2.10 I-V characteristic for reverse mode for different anodization currents at temperature 300 K [8]

That is due to the fact that electron affinity χ increases with anodization current density and potential barrier eF_S between Nb₂O₅ and MnO₂ decreases with increasing anodization current density [18]. Similar behavior is valid for Ta capacitor as well.

2.2.3. Preparation of the cathode side

The every step is very important and the other process is cathode preparation. This process is called **manganization**. The manganese nitrate and his thermal dissociation onto the sequential into the manganese dioxide and nitrogen oxide caused the growing next layer as described the equation 2.4.



The process of manganization is repeated several times for the enough strength of the layer. The concentration of MnO₂ is changed in every step. The preparation of the MnO₂ from

liquid solution is necessary for creation of the contact on Ta₂O₅ inside the porous structure when good penetration of MnO₂ in the pores is required. Alternative method for the cathode preparation is the use of conductive polymer (CP) based on the polypyrrole. Formed anode is dipped in CP to reach proper contact. Sequential CP on pre-polymerized CP is used for cathode creation. MnO₂ forms conductive connection between Ta₂O₅ layer and outer contact electrode [15, 16].

The main difference between MnO₂ and CP is in the structure of the material. The MnO₂ is very hard, crystalline material and it is shown in Fig. 2.11 on the left hand side. Right hand side of the Fig. 2.11 shows the CP material which is more soft and elastic. High elastic is advantageous due to lower probability of the crack creation after the mechanical stress of structure [21, 22].

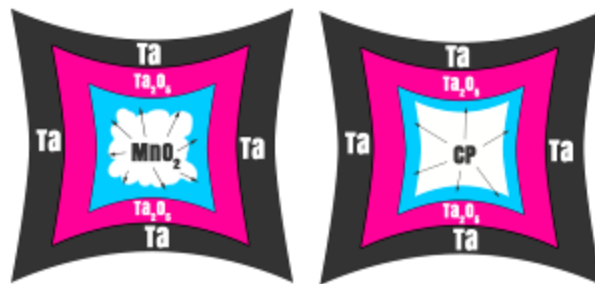


Fig. 2.11 The difference of the material for the MnO₂ an CP [17]

The main advantage of the using the CP is ignition process and due to no oxygen in the structure the ignition process is hardly separated from the failure of the capacitor. A distinguished property of tantalum capacitors with MnO₂ or CP cathode is renovating mechanism, this mechanisms is described in [21, 41 and 51]. Then MnO₂ or CP is covered by the carbon-graphite paste for better adhesion and connection to the silver layer. The process of dipping is used for creating new layer. Structure of tantalum capacitor is shown in Fig. 2.12.

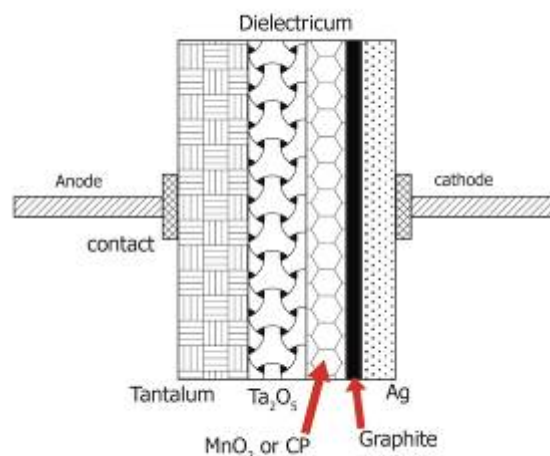


Fig. 2.12 Basic structure of tantalum capacitor

The created structure is connecting with the terminal pins. The positive anode is weld onto the Ta wire with the terminal pin; negative cathode is glued by epoxy. Packaging is next

step, and epoxy resin is impressed for the encapsulation to the final case. The created SMD is cleared, sanded and washed by water. Consequently is made the description into the SMD surface by laser. There are the parameters as polarity, operation voltage, capacity and part number in this case. The capacitors have own protocol during the manufactory process and is it possible to find the mistake in the manufactory of the capacitors in each step. Thus made capacitor is ready for testing and transport to the customers. Before the capacitor leaves the manufactory a lot of tests are performed. Important process is burning of capacitors. This process lead to stabilization of electrical properties and the capacitors with lower quality are excluded from the process. The basic method of burning is applied the higher voltage and **temperature** for a longer time around up to 10 hours. Than the capacitors are measured for their electrical properties and the parameters capacity, ESR and I-V characteristics are discovered. The process of recovering is found as well [23].

3. MIS model of tantalum capacitors

The basic physical models of capacitors (see in Fig. 3.1) consist of two parallel metal plates, which are separated by the dielectric material. There are two electrodes one of them is anode with positive charge, while the second electrode is cathode with negative charge.

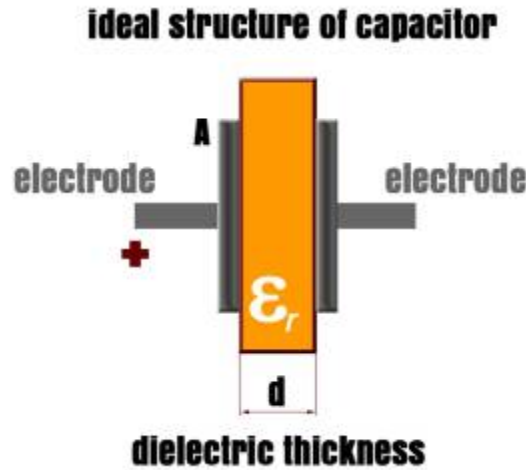


Fig. 3.1 Ideal structure of physical model of capacitor

When this structure is charged it causes the increase of potential difference between the plates. The potential difference is measure as voltage V on capacitor and it is proportional to the charge Q on capacitors as:

$$Q = C.V \quad (3.1)$$

Where C is the capacitance. From the Gauss law of electrostatic we can derive the capacitance of the plate capacitor as:

$$C = \frac{Q}{V} = \frac{\epsilon_r \epsilon_0 A}{d} \quad (3.2)$$

Where d is dielectric thickness, ϵ_0 is dielectric constant for vacuum, ϵ_r is relative permittivity, and A is area of electrodes, Q is charge on the electrode, V is the voltage difference between the electrodes [24].

Porous structure of tantalum capacitor is far away from the ideal plate capacitor but the formula 3.2 for the capacitance calculation can be used as the first approximation for the „sponge” structure surface area estimation. The active surface area A of the tantalum capacitor can be calculated as:

$$A = \frac{C.d}{\epsilon_0 \epsilon_r} \quad (3.3)$$

The dielectric layer thickness d is determined either from the known parameters of anodic oxidation process, or from the direct measurement of thickness from the SEM pictures of the tantalum capacitor cross-cut. Capacitance C value can be measured on the RLC bridge as well.

3.1. The theory of MIS structure

The capacitor structure is very complicated and there are many used materials, many variation of construction. However its behavior, with respect to the charge transport in the capacitor, can be described by the metal-insulator-semiconductor (MIS) model, which for the tantalum capacitor structure is shown in Fig. 3.2. The description of tantalum capacitor as a MIS structure was first presented in [17, 25 - 28]. Further this theory was studied by Teverovsky in [22]. The key parameter for the MIS model of tantalum capacitor is the determination of height of potential barriers' on the metal – insulator, and insulator – semiconductor interface, respectively. These parameters can be determined form the analysis of tantalum capacitor transport characteristic.

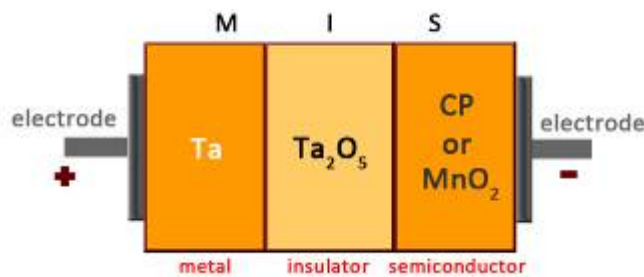


Fig. 3.2 Basic MIS structure of tantalum capacitor

The MIS structure for tantalum capacitor consists of metallic tantalum Ta, insulator Ta₂O₅ and semiconductor MnO₂ or CP, respectively. Figures 3.3 and 3.4 show energy band diagram before the thermodynamic equilibrium for capacitor with MnO₂ cathode and CP cathode, respectively. Here W_M is work function of tantalum, c_i is Ta₂O₅ electron affinity, W_{MnO_2} is work function for the manganese dioxide MnO₂, E_F Fermi level, E_{CI} is conducting band energy in insulating layer Ta₂O₅, E_{VI} valence band energy in insulator layer Ta₂O₅, E_D is donor energy band in insulator layer Ta₂O₅, E_{CS} is conducting band energy in semiconductor layer MnO₂, E_{VS} valence band energy in the semiconductor layer MnO₂, HOMO is energy level of highest occupied molecular orbital in conducting polymer, LOMO is energy level of lowest unoccupied molecular orbital in conducting polymer. HOMO level in the organic semiconductor is corresponds to the valence band maximum energy level in the inorganic semiconductors. The same analogy is between LUMO energy level and the energy level of the bottom of conduction band [26-29].

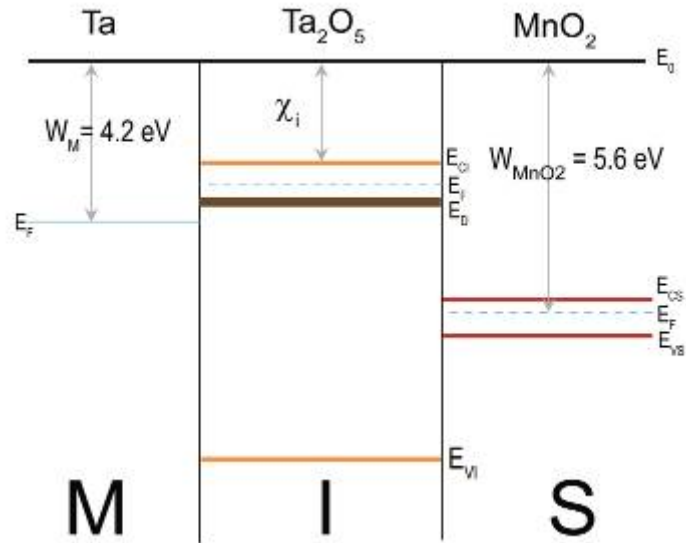


Fig. 3.3 MIS model structure before thermodynamic equilibrium for the tantalum capacitor with MnO₂ cathode

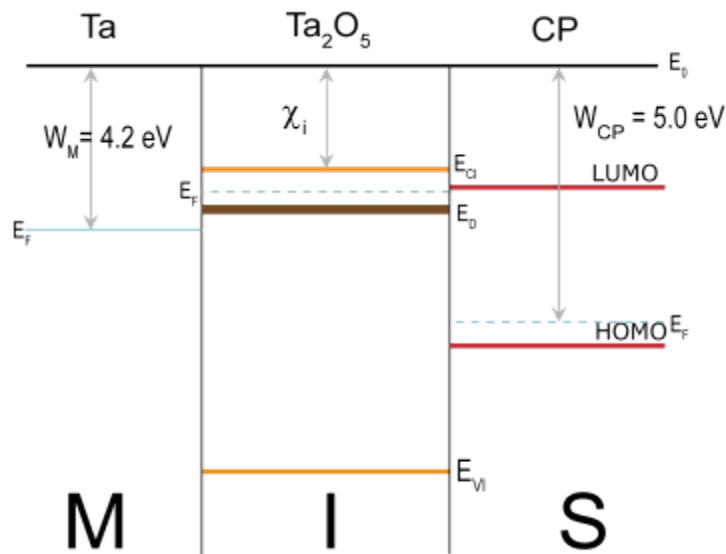


Fig. 3.4 MIS model structure before thermodynamic equilibrium for the tantalum capacitor with CP cathode

Figures 3.5 and 3.6 show the MIS model structure of the tantalum capacitors with MnO₂ and CP cathode, respectively, after the thermodynamic equilibrium. Here ϕ_{MI} is energy barrier on the interface between tantalum and insulating layer Ta₂O₅, ϕ_{IS} is energy barrier on the interface between insulator layer Ta₂O₅ and semiconductor MnO₂, E_g is forbidden energy gap value, E_D is defect energy band in insulating layer Ta₂O₅ [18, 26, 27-32].

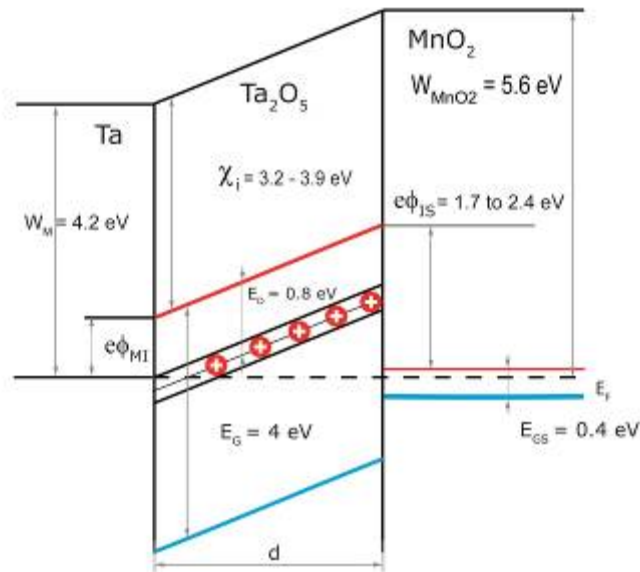


Fig. 3.5 MIS model structure in thermodynamic equilibrium for the tantalum capacitor with MnO₂ cathode

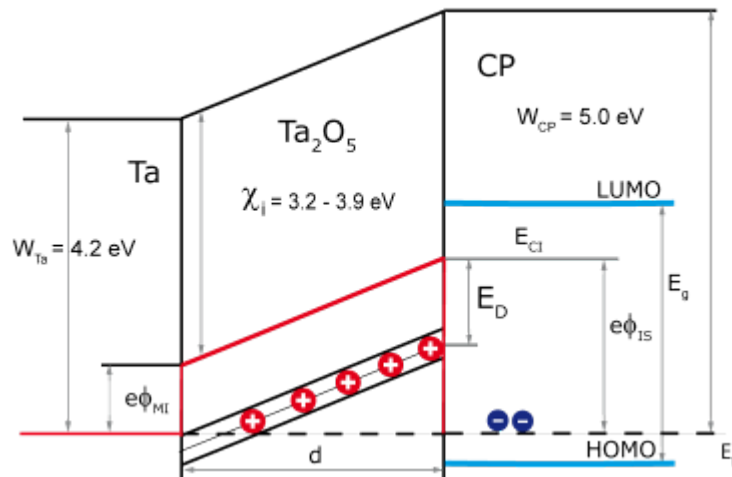


Fig. 3.6 MIS model structure in thermodynamic equilibrium for the tantalum capacitor with CP cathode

The basic values for determination of band diagrams are as follows: value of work function for tantalum Ta is 4.2 eV, work function for manganese dioxide MnO₂ is 5.6 eV, work function for conducting polymer CP is about 5.0 eV, and electron affinity for amorphous structure of Ta₂O₅ in range from 3.2 up to 3.9 eV according the anodic oxidation technology. The electron affinity χ_i is a quantity defined as the energy required for an electron to be removed from the bottom edge of the Ta₂O₅ conduction band to a point in vacuum just outside the Ta₂O₅. The value of the electron affinity depends on the insulating layer structure [18, 26, 27-32]. For amorphous thin Ta₂O₅ film ($d < 50$ nm) the electron affinity χ_i ranges from 3.2 to 3.9 eV while for thick ($d > 200$ nm) polycrystalline Ta₂O₅ film equals $\chi_i = 1.2$ eV [18, 26, 27-32]. It was established that the higher electron affinity χ_i the lower leakage current. The next parameter is

the concentration of the impurity which states in the forbidden energy gap of Ta₂O₅. Insulating Ta₂O₅ films always contain impurities like oxygen vacancies and traps. These impurities form localized states for charge carriers in the forbidden energy gap. When the localized electronic wave functions of the localized states overlap, an electron bound to one impurity state can tunnel

to an unoccupied state without involving activation into the conduction band. This tunneling process between impurity sites is referred to as impurity conduction [18, 26, 27-32].

The difference between Ta₂O₅ electron affinity and work function of MnO₂ or CP respectively determines barrier Φ_{IS} on the insulator – semiconductor interface. This barrier is for amorphous Ta₂O₅ in the range 1.7 up to 2.4 eV. With increasing barrier height the current through the capacitor structure decreases. The difference between Ta₂O₅ electron affinity χ_i and work function from tantalum determines the value of potential barrier Φ_{MI} on the metal – insulator interface. This barrier height value is in the range from 0.2 up to 0.9 eV [18, 26, 27-32].

High number of oxygen vacancies is formed in Ta₂O₅ layer during the anodic oxidation process. The concentration was determined to be in the range 10¹⁷ to 10¹⁹ cm⁻³. Oxygen vacancies act as donor states in tantalum pentoxide and for this high concentration impurity band is formed. The impurity band width DE_{imp} is roughly given by the formula:

$$DE_{imp} = \frac{\hbar e^2 N_D^{1/3}}{4\pi\epsilon_0 \epsilon_r} \quad (3.4)$$

And for donor concentration $N_d = 10^{17}$ to 10^{19} cm⁻³ we have $DE_{imp} = 10$ to 20 meV. Donors' activation energy was determined for 0.4 eV for the temperature range up to 400 K. Then the donor energy band in insulator layer is approximately 0.8 eV below the conduction band in Ta₂O₅.

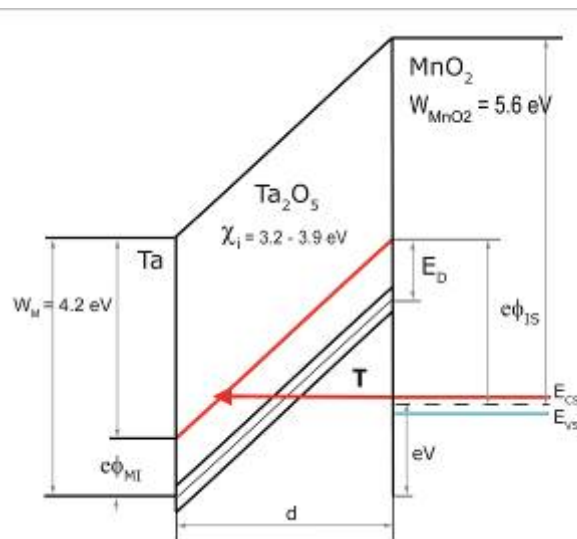


Fig. 3.7 MIS model structure for applied voltage on the tantalum capacitor with MnO₂ cathode – normal mode

Figure 3.7 shows the MIS model structure for applied voltage on tantalum capacitor with MnO₂ cathode in normal mode (anode is positive). The MIS model structure for applied voltage on the tantalum capacitor with CP cathode in normal mode is shown in Fig. 3.8. In this case is the boundary between Ta₂O₅ insulating layer and CP cathode the PN junction exists due to that Ta₂O₅ has N-type conductivity and conducting polymer is P-type semiconductor. This PN junction has influence on low voltage tunneling current component as will be shown in experimental part. After the voltage V application the effective thickness of the potential barrier in insulator decreases. With decreasing potential barrier thickness the probability for charge carrier tunneling increases.

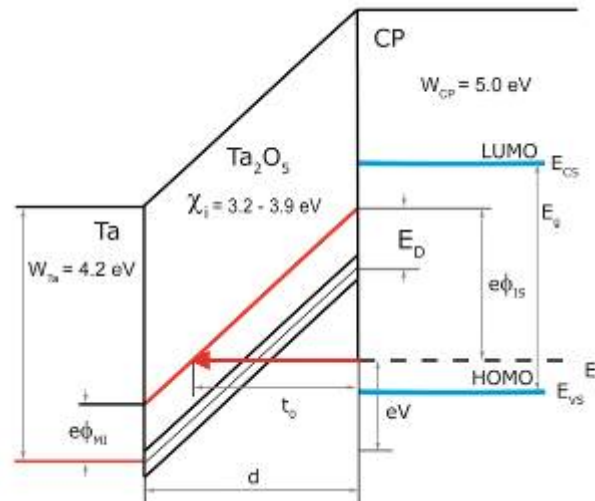


Fig. 3.8 MIS model structure for applied voltage on the tantalum capacitor with CP cathode – normal mode

Figure 3.9 shows the basic band diagram to explain the charge carrier transport in the capacitor in normal mode. These are Ohmic current component, Poole-Frenkel current component and tunneling current component. The Ohmic conduction mechanism is mainly influenced by electron hopping between neighboring impurity site in the defect band. This type of the conduction process depends on impurity concentration and the energy depths of the impurity states.

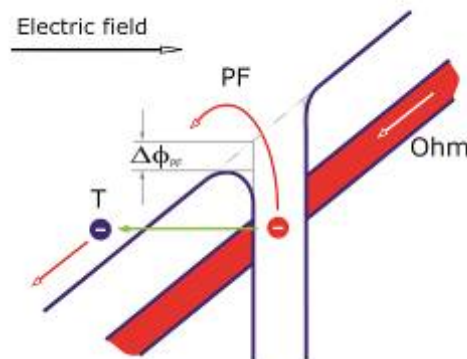


Fig. 3.9 Basic principal of the charge carrier transport in the capacitor

The concept of the hopping transport has been used for a long time in connection with ionic conduction; ions move essentially by hopping, whether through interstices or vacancies. In our case we suppose that electrons' hopping is involved as a source of the Ohmic current. Poole-Frenkel current component is pronounced in higher temperature range and involves the electron excitation from the donor state into the conduction band of tantalum pentoxide. The probability of this mechanism increases with applied voltage due to the rice of potential barrier lowering DF_{PF} . Another transport mechanism is tunneling of charge carrier from the bounded state in impurity band or from the highest occupied state in MnO₂ or CP cathode to the conduction band in tantalum pentoxide. Poole-Frenkel charge transport mechanism is pronounced for temperatures above 150 K while in the low temperature range tunneling current and Ohmic current components are dominant [17,18,25,28,34,38].

Figure 3.10 shows the MIS model structure for applied voltage on tantalum capacitor with MnO₂ cathode in reverse mode (anode is negative). The MIS model structure for applied voltage on the tantalum capacitor with CP cathode in reverse mode is shown in Fig. 3.11. For bias voltage higher than $V_f = (W_{cathode} - W_{anode})/e$, where V_f is flat-band voltage given by the difference between the work-functions of cathode and anode material and e is elementary charge, the effective thickness of the potential barrier in insulator decreases. With decreasing potential barrier thickness the probability for charge carrier tunneling increases.

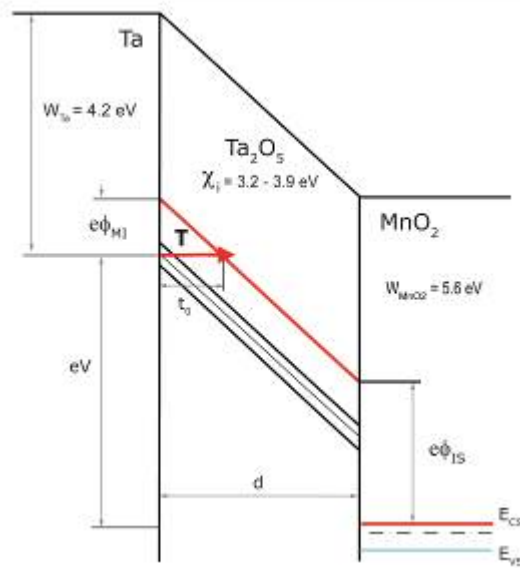


Fig. 3.10 MIS model structure for applied voltage on the tantalum capacitor with MnO₂ cathode – reverse mode

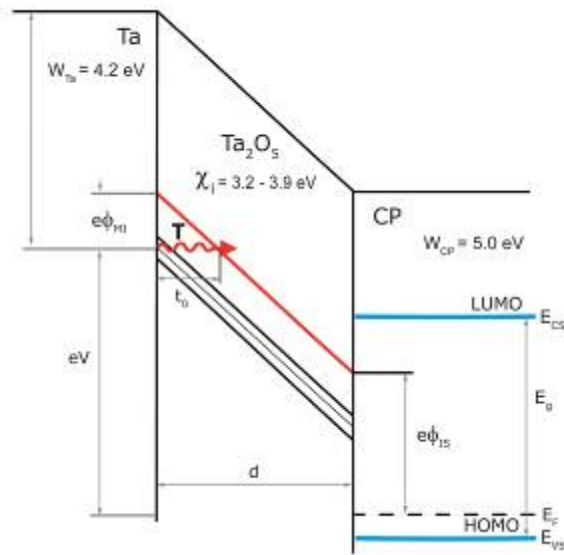


Fig. 3.11 MIS model structure for applied voltage on the tantalum capacitor with CP cathode – reverse mode

In the reverse mode ohmic current component is observed for low electric field while for higher electric field the over barrier thermionic emission current component is dominant for the temperatures higher than 150 K. With decreasing temperature the tunneling current became dominant [17, 18, 25, 28, 34, 38].

3.2. Charge transport in tantalum capacitor

For an ideal capacitor no transport of charge through the insulating layer is considered. In the real structure the current flowing through the capacitor after the steady state achievement is denoted as leakage current (DCL). According to the classical theory the leakage current was described by current on the surface and current through the cracks and defects in dielectrics layer (see Fig 3.12). This model has substantiation in devices with higher leakage currents and these devices have really higher number of cracks inside the structure. With improving capacitor technology the leakage current value decreased and the “crack” theory become insufficient. The DCL characteristics measured for a group of capacitors show excellent reproducibility both in the value and shape of I - V curve, which is unlikely in case of charge transport through the cracks. It is supposed, that the DCL is given by the charge transport mechanisms pronounced in MIS structure [18, 26, 27-33,56-58].

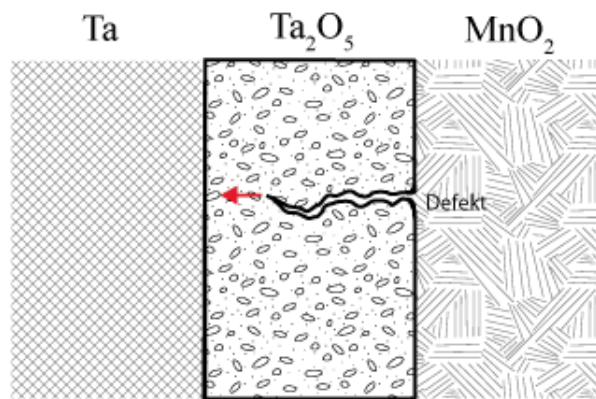


Fig. 3.12 Defect in the Ta₂O₅ structure as a source of leakage current

The appropriate mechanisms involved in the charge transport are possible to determine from the analysis of I - V characteristic [18, 26, 27-33]. Beside the transport mechanisms already mentioned above, i.e. ohmic, Poole-Frenkel, Schottky and tunneling mechanism, we must also consider thermionic emission limited over barrier current, space charge limited current and the polarization current in the I - V characteristic analysis [32-39].

3.2.1. Ohmic current component

The ohmic current can be observed for applied electric field smaller than 0.5 MV.cm⁻¹ at room temperature. There is small influence of the electric field polarity, for the normal mode and reverse mode the value is vice versa. This current component is temperature dependent and it is characterized by resistance of the conductive layer. Ohmic current component is given as:

$$I_w = G_w V \quad (3.5)$$

Where G_w is ohmic conductivity, which is influenced by concentration of oxygen vacancies in the impurity band and V is voltage. For the lower values of electric field the ohmic conductivity can be defined as:

$$G_w = Aenm/d \quad (3.6)$$

Where A is area of capacitor electrode, e is elementary charge, n is concentration of charge carriers, m is mobility of charge carriers and d is the Ta₂O₅ layer thickness. As mentioned above the ohmic conduction mechanism is mainly influenced by electron hopping between neighboring impurities sites. This mechanism causes to the linear dependence of leakage current on the applied voltage.

Figure 3.13 shows the I - V characteristic in linear scale and J - E characteristic in logarithmic scale for sample KOL2012 – 05 measured for temperatures 12 K, 40 K and 150 K. Linear dependence between the current and voltage or current density and electric field, respectively, can be determined from measured characteristics. We can see that linear function fit the measured I - V curve in the voltage range 0 to 0.4 V. The slope of straight line is 5.2×10^{-8} S for temperature 12 K and 1.0×10^{-8} S for temperature 150 K, which gives the value of ohmic conductivity. The logarithmic graph shows the electric field range where the ohmic current component is dominant. That is for the part where the measured data could be approximated by the straight line with the slope $m = 1$. For the sample KOL 2012-05 the ohmic current component is dominant for electric field up to 0.05 MV.cm⁻¹. For higher electric field injection of electrons into insulator is observed (see Fig. 3.13).

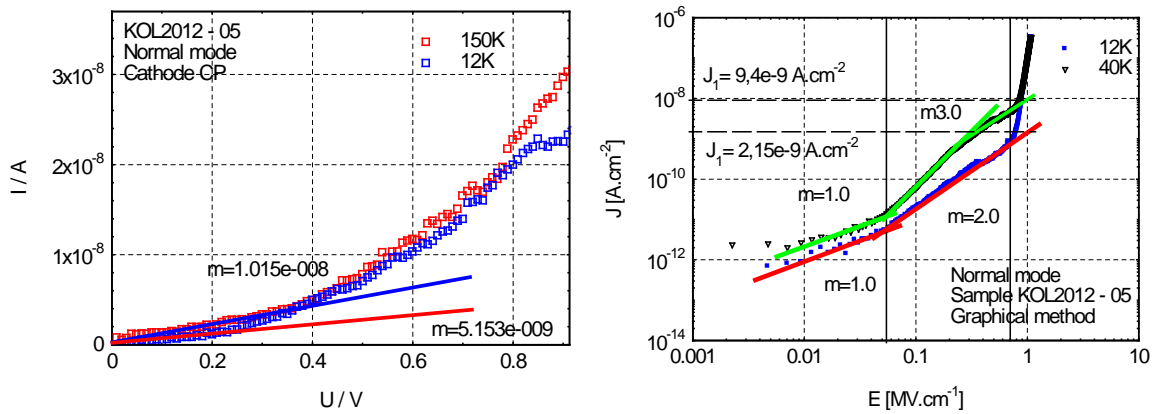


Fig. 3.13 I-V characteristic (linear scale) and J - E characteristic (logarithmic scale) for sample KOL2012 – 05 measured for temperatures 12 K, 40 K and 150 K

3.2.2. Space charge limited current

Space charge limited current density J_{SC} is covered by Mott-Gurney square law [31]:

$$J_{SC} = \frac{8\epsilon_0\epsilon_r m V^2}{9d^3} \quad (3.7)$$

Where ϵ_0 is permittivity of vacuum, ϵ_r is Ta₂O₅ dielectric constant, m is mobility, V is voltage bias, and d is Ta₂O₅ layer thickness.

The equation covers the current density in case of shallow traps in dielectric layer. In our case the donor energy band is approximately 0.8 eV below the conduction band in Ta₂O₅ layer. For deep traps the occupancy of the trap level increases and trapped charges play important role in current density-voltage curve. At low bias voltage the charge transport is governed by the trap-charge-limited current, when an increase in the number of injected electrons causes the filling of traps and increase of the space charge. This leads to an abrupt

increase of the current slope, J vs. V^m with exponent $m > 2$ (see Fig. 3.13 – measurements for temperature 40 K, where the slope in log-log graph is $m = 3$). For higher voltage bias the trapping sites are already filled and all additionally injected carriers contribute to the space-charge-limited current. The voltage exponent higher than 2 decreases and the current density increase toward the square law [56, 57].

Considering the quadratic approximation of space charge limited current density J_{sc} vs electric field plot in logarithmic scale we get the straight line the slope 2. This quadratic approximation in the logarithmic scale is then given by equation:

$$\log J_{sc} = \log \frac{8e_0 e_r m}{9d} + 2 \log E \quad (3.8)$$

Then from the value of current density J_{sc1} obtained from the intersection of quadratic approximation with the line $E = 1$ V/m we can calculate the mobility of charge carriers as:

$$\log J_{sc1} = \log \frac{8e_0 e_r m}{9d} \quad \text{and} \quad m = \frac{J_{sc1} 9d}{8e_0 e_r} \quad (3.9)$$

3.2.3. Poole-Frenkel current component

The process of the Poole-Frenkel (PF) charge transport is described as the thermionic emission of charge from the localized state in the defect band of insulator into the conductivity band and its' transfer into the anode. This effect is important for temperature range above 150 K. Figure 3.9 shows the principle of the PF effect. It is obvious from Fig. 3.9 that the electron is emitted into the conduction band and continues into the anode. There E_a is required charge activation energy, $\Delta e F_{PF}$ is the potential barrier lowering due to the Poole-Frenkel effect, and E is electric field [31, 41 - 43].

Poole-Frenkel current I_{PF} is given as [31]:

$$I_{PF} = G_{PF} V \exp(b_{PF} \sqrt{V}) \quad (3.10)$$

Where G_{PF} is Poole-Frenkel conductivity and β_{PF} is Poole-Frenkel coefficient dependent on the Ta₂O₅ layer thickness d as:

$$b_{PF} = \frac{\sqrt{e^3 / p e_0 e_r d}}{kT} \quad (3.11)$$

Where e is elementary charge, ϵ_0 is dielectric constant of vacuum, ϵ_r is Ta₂O₅ relative permittivity, k is Boltzmann constant and T is thermodynamic temperature in Kelvin. Barrier for the electron thermal emission from the impurity band to the conduction band decrease with increasing electric field according the formula:

$$- DeF_{PF} = \frac{e}{kT} \sqrt{\frac{eE}{\rho e}} \quad (3.12)$$

Where e is electron charge, k is Boltzmann constant, T is thermodynamic temperature, E is the electric field in insulating layer and ρ is dielectric constant of an insulator [31, 41].

For analysis of investigated results there are used two methods - the analytical and the graphical one. The analytic method is based on the fitting of measured results by the mathematical model and determination of the functions and parameters of considered current components. The graphical method is based on the depiction of experimental data in such graph, where the desired charge transport mechanism is represented by linear dependence. This graph is often denoted as PF plot.

The evaluation of experimentally obtained data by both analytical and graphical methods is shown in Figs. 3.14 and 3.15 for sample KOL2012-05 for temperature 150 K. The analytic method considers the ohmic, PF and tunneling current component for fitting the experimental curve. From the fits in Fig. 3.14 it is evident that PF current component for the temperature 150K is not dominant. The Poole-Frenkel coefficient value is determined $\beta_{PF} = 4.78 \text{ V}^{-0.5}$ while the theoretical value is $5.50 \text{ V}^{-0.5}$.

For evaluation by graphical method is necessary to recalculate the data for evaluation. On the y axis is current density divided by the electric field in units $\text{A}\cdot\text{V}^{-1}\cdot\text{m}^{-1}$ in the logarithmic scale. On the x axis is root from the electric field in $\text{V}^{0.5}\text{m}^{-0.5}$ unit in linear scale. The PF mechanism is determined as the linear dependence in the graph and from the slope m of this line is possible to calculate Poole-Frenkel coefficient β_{PF} from the equation:

$$m = b_{PF} \cdot d^{\frac{1}{2}} \cdot \log e \quad b_{PF} = \frac{m}{d^{\frac{1}{2}} \cdot \log e} \quad (3.13)$$

Where the d is insulating layer thickness, e is Euler's number.

Poole-Frenkel coefficient β_{PF} is temperature dependent and it is inversely proportional to the insulating layer thickness d . The β_{PF} coefficient decreases with increasing layer thickness and increases with decreasing temperature [31, 41]. Theoretical value calculated for sample KOL2012-05 at temperature 150 K is $5.50 \text{ V}^{-0.5}$. From that the slope m of line in PF plot should be $4.90 \text{ MV}^{-0.5}\text{cm}^{0.5}$. We can see that the slope determined from the experimental data is about $4.42 \text{ MV}^{-0.5}\text{cm}^{0.5}$, which is close to the theoretical value. However the PF current component is observed only in the range 0.1 to 0.6 MV/cm and for lower temperatures this current component is negligible [31, 41 - 43].

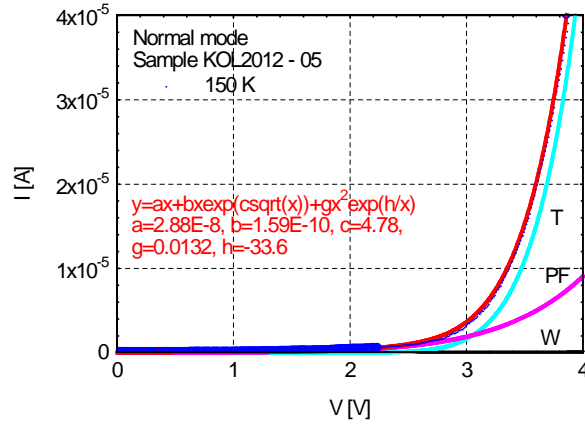


Fig. 3.14 Analytical method for determination of Poole-Frenkel current component from I - V characteristics for the sample KOL2012-05 in normal mode for the temperature 150 K

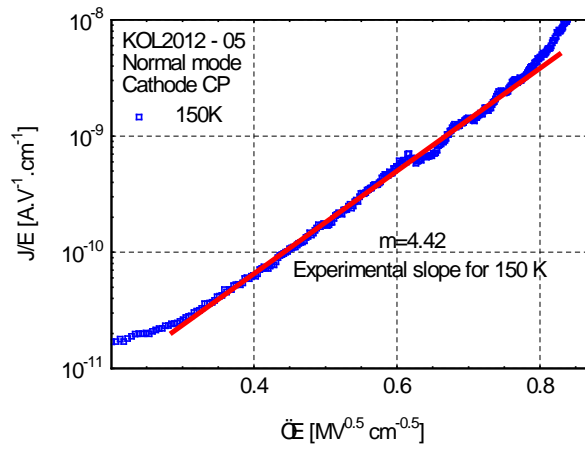


Fig. 3.15 Graphical method of Poole-Frenkel current component evaluation with experimentally determined line for the sample KOL2012-05 in normal mode for the temperature 150 K

3.2.4. Schottky current component

The Schottky charge transport mechanism is described as the thermionic emission of charge from the cathode into the Ta₂O₅ conductivity band and its' transfer into the anode.

Schottky current I_s is given as [31]:

$$I_s = I_{s0} \exp(b_s \sqrt{V}) \quad (3.14)$$

Where I_{s0} is Schottky current constant and β_s is Schottky coefficient dependent on the Ta₂O₅ layer thickness d as:

$$b_s = \frac{\sqrt{e^3 / 4pe_0 \epsilon_r d}}{kT} \quad (3.15)$$

Where e is elementary charge, ϵ_0 is dielectric constant of vacuum, ϵ_r is Ta₂O₅ relative permittivity, k is Boltzmann constant and T is thermodynamic temperature in Kelvin. Barrier for

the electron thermal emission from cathode to the conduction band decreases with increasing electric field according the formula:

$$-DeF_s = \frac{e}{kT} \sqrt{\frac{eE}{4\rho e}} \quad (3.16)$$

Where e is electron charge, k is Boltzmann constant, T is thermodynamic temperature, E is the electric field in insulating layer and ρ is dielectric constant of an insulator [31, 41].

Comparing equations 3.11 and 3.15 we can see that $b_{PF} = 2b_S$. These constant characterize the barrier lowering due to the Poole-Frenkel or Schottky effect, respectively. Schottky constant can be determined by the graphical method from the linear part of $\log J$ vs. E plot. From the slope m of this linear approximation the Schottky coefficient can be calculated as:

$$m = b_S \cdot d^{\frac{1}{2}} \cdot \log e \quad \text{and} \quad b_S = \frac{m}{d^{\frac{1}{2}} \cdot \log e} \quad (3.17)$$

Where d is insulating layer thickness, e is Euler's number.

However the Schottky current component in tantalum capacitors as well as in MIS structures with insulator thickness of the order of tens of nanometers at the room temperature is mostly negligible [3, 20, 57].

3.2.5. Tunneling current component

The leakage current is at low temperatures and at high electric field influenced mainly by electron tunneling through a potential barrier between Ta₂O₅ insulating layer and cathode or anode, respectively. The potential barriers can be approximated by square or triangular shapes. The triangular shape facilitates an intermolecular electron transfer, since the barrier width at higher fields becomes smaller for the high energy electrons.

The equation describing the I - V characteristic for tunneling current is described by [31]:

$$I = G_T V^n \exp\left(-\frac{U_T}{V}\right) \quad (3.18)$$

Where V is the applied voltage, G_T and U_T are tunneling current constants, and the value of the exponent n depends on the barrier shape (for triangular barrier $n = 2$). The tunneling parameter U_T can be expressed for the energy barrier eF_0 as:

$$U_T = \frac{8\rho\sqrt{2m^*}}{3eh} (eF_0)^{1.5} d \quad (3.19)$$

Here, m^* is the electron effective mass, $h = 6.6 \times 10^{-34}$ J.s is the Planck constant and e is the elementary charge and d is the thickness of the insulating layer [31, 34 – 47].

For the dependence of the tunneling current density J vs. electric field E one can calculate:

$$J = g_T E^2 \exp\left\{-\frac{E_T}{E} \frac{\hbar}{e}\right\} \quad (3.20)$$

Where g_T and E_T are the tunneling current density constants. The value of tunneling parameter G_T and g_T characterizes the energy barrier transparency for charge tunneling. The higher is the value of G_T or g_T the higher is tunneling current component value. The tunneling parameter E_T can be expressed for the energy barrier eF_0 as:

$$E_T = \frac{8\rho\sqrt{2m^*}}{(3eh)} (eF_0)^{1.5} \quad (3.21)$$

Here, m^* is the electron effective mass, $h = 6.6 \times 10^{-34}$ J.s is the Planck constant and e is the elementary charge [31, 34 – 47].

The values of the tunneling parameters U_T and E_T depend on the electron effective mass. In this work the potential barrier eF_0 in eV was estimated for electron effective mass $m^* = 0.1 m_0$, where $m_0 = 9.1 \times 10^{-31}$ kg is the electron rest mass. Using this value for m^* we obtained a good agreement of experimental and theoretical I - V characteristics. [31, 34 – 47]

Figure 3.16 shows the calculated dependences between tunneling parameter E_T and energy barrier height eF_0 and tunneling parameter U_T for dielectric layer thickness 30 nm and energy barrier height eF_0 , respectively. The calculations are done for different electron effective mass values. With increasing electron effective mass value the value of U_T and E_T for given energy barrier increases.

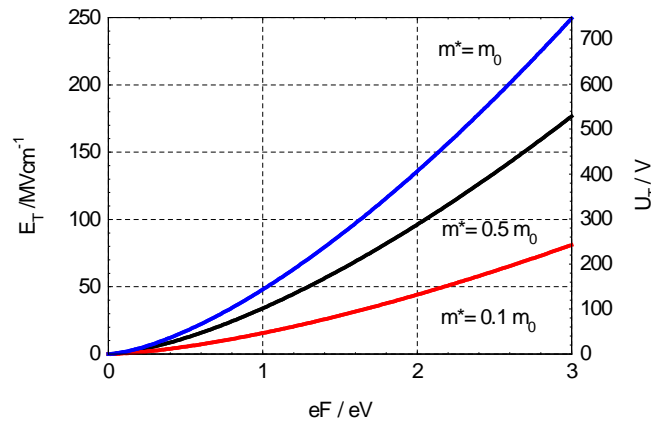


Fig. 3.16 Tunneling parameter E_T and tunneling parameter U_T vs. barrier height calculated for different electron effective mass values for the dielectric layer thickness 30 nm

The effect of tunneling is described as electron movement through the barrier without any change of the energy. For the tunneling probability D it holds:

$$D = D_0 \exp\left\{-\frac{2t_0 \sqrt{(2m^* e F_0)}}{h}\right\} \quad (3.22)$$

Where D_0 is constant and in first approximation $D_0 = 1$, and t_0 is the potential barrier thickness, m^* is effective electron mass, $h = 6.6 \times 10^{-34}$ Js is Planck constant and eF_0 is the barrier energy. It is important that tunneling probability D does not depend on temperature. Tunneling process is in the first approximation temperature independent.

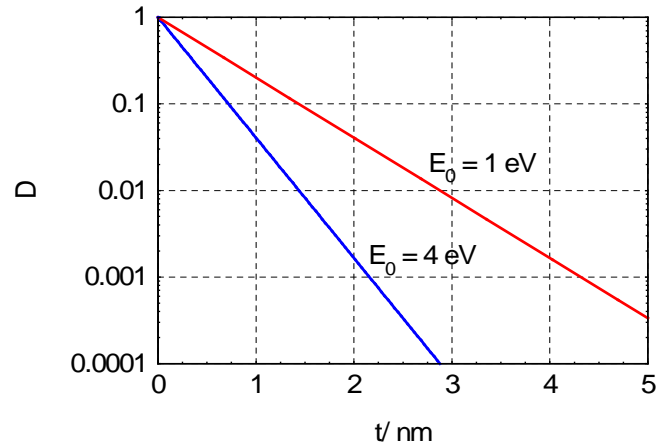


Fig. 3.17 Tunneling probability coefficient D vs. tunneling barrier thickness for different barrier energy values

However for the low temperature region below 50 K probably the electron effective mass dependence on temperature must be taken in account. The tunneling probability D for barrier energy $eF_0 = 1$ eV and 4 eV is shown in Fig. 3.17. For the barrier energy 1 eV and thickness $t_0 = 3$ nm the tunneling probability D is about 10^{-2} , while for barrier energy 4 eV we find the value for hundred times smaller.

For the better interpretation of the triangular potential barrier see in Fig. 3.18, where the potential barrier thickness is t_0 , d is dielectric layer thickness, eF_c is barrier on the cathode side which is pronounced to the charge tunneling in normal mode and V_1 and V_2 are different values of bias voltage. With increasing voltage bias the thickness t_0 of triangular potential barrier decreases which leads to the tunneling probability increase.

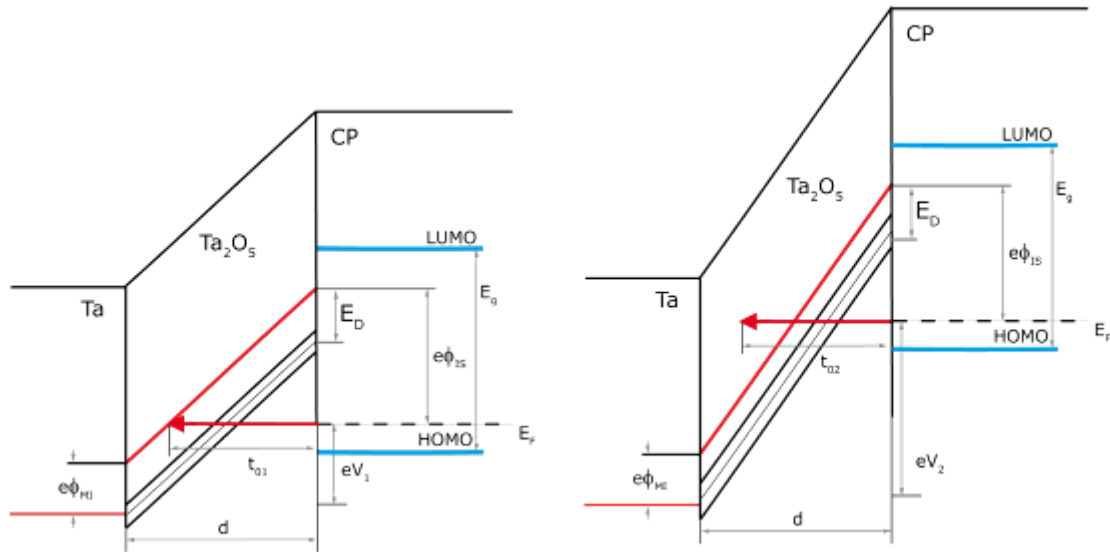


Fig. 3.18 The triangular potential barrier for electron tunneling

Figure 3.19 shows the analytical method for the evaluation of the I - V characteristic for sample KOL2012-05 at temperatures 12 K, where only the ohmic and tunneling current is considered as a source of DCL. Here the tunneling current constants have the values $G_T = 16.9 \text{ AV}^{-2}$ and $U_T = 69.2 \text{ V}$.

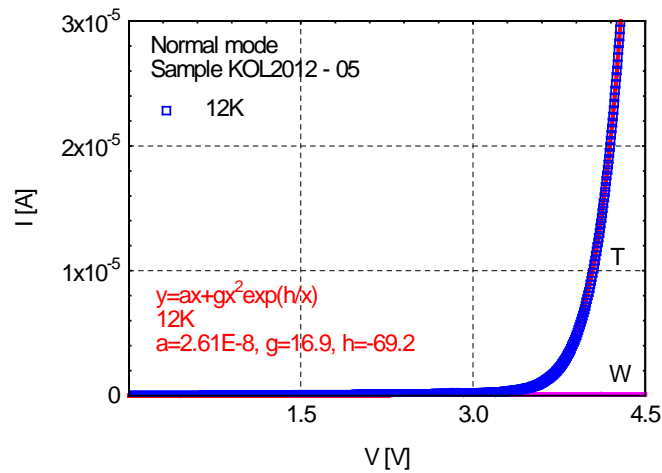


Fig. 3.19 Analytical method for determination of tunneling current component for sample KOL2012-05 at temperature 12 K

Graphical method for the tunneling current component evaluation is called Fowler-Nordheim graph. The y-axis shows the current density divided by the square of electrical field in A.V^{-2} units in the logarithmic scale. The x-axis shows the reciprocal value of electric field in V.m^{-1} units in linear scale [31, 34 – 47]. The graph indicates the tunneling current as a dominant current mechanism for sample KOL2012-05 for the low temperatures. For the temperature 12 K the slope of linear dependence is 7.47 MV/cm .

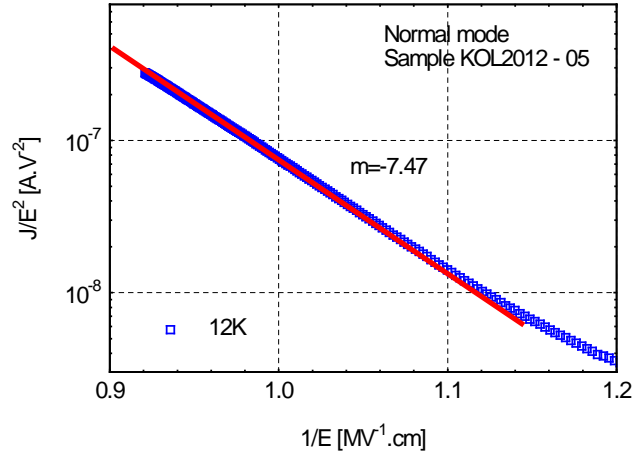


Fig. 3.20 Interpretation of Fowler-Nordheim graph by graphical method for sample KOL2012-05 at temperature 12 K

From the slope of linear dependence the value of tunneling parameter E_T is calculated as:

$$m = E_T \cdot \log e \quad \text{or} \quad E_T = \frac{m}{\log e} \quad (3.23)$$

Where e is Euler's number. Tunneling parameter U_T is calculated as $U_T = E_T d$, where d is the insulating layer thickness.

3.2.6. Thermionic emission limited current over a Schottky barrier

The thermionic emission of charge carriers over the potential barrier is an important mechanism for the charge transfer in the semiconductor devices [2, 57, 58]. The thermionic emission current can be described by Shockley equation:

$$I_T = I_0 (\exp(b_{TE} V) - 1) \quad (3.24)$$

Where thermionic emission current constant I_0 is given by:

$$I_0 = A R T^2 \exp\left(-\frac{e\Phi_s}{kT}\right) \quad (3.25)$$

And thermionic emission parameter β_{TE} is given by:

$$\beta_{TE} = \frac{e}{nkT} \quad (3.26)$$

Where the A is area of electrodes, R is Richardson constant for emission of electrons from metal into the insulator layer or semiconductor, T is thermodynamic temperature, $e\Phi_s$ is Schottky potential barrier and, k is Boltzmann constant, e is elementary charge and n is ideality factor for over-barrier transport. For ideal structure is $n = 1$, for the Schottky diodes and MIS structures it varies in the range 1-2 at the room temperature.

Thermionic emission current component is thermally activated and depends on the energy barrier height. It is observed in tantalum capacitors in the reverse mode only, because the barrier formed between the cathode and Ta₂O₅ is higher than 1 eV and thermal activation over this barrier is negligible even at the room temperature [17, 18, 25, 28, 34, 38]. For the studied temperature range we can evaluate the thermionic emission current component for the temperatures down to 100 K from the reverse mode *I-V* characteristics.

Thermionic emission current component increases exponentially with the applied voltage. In semi-logarithmic scale the thermionic emission current component is shown as the straight line. From the linear approximation of measured data we can determine the value of thermionic emission current constant I_0 from the intersection of approximation line with y-axis. From the slope m of linear approximation the value of β_{TE} is calculated as:

$$m = \beta_{TE} \cdot \log e \quad \beta_{TE} = \frac{m}{\log e} \quad (3.27)$$

From determined value of β_{TE} we can calculate the ideality factor for thermionic emission current from eq. 3.26.

4. Aims of doctoral thesis

- Main aim of this thesis is the study of charge transport mechanisms in the structures of tantalum capacitors with dielectric layer formed by the tantalum pentoxide Ta₂O₅. I will be concerned on the transport mechanisms which are pronounced in the low temperature range 10 to 100 K, and 100 to 250 K, respectively. The electric field range for particular transport mechanisms will be stated.
- I will study the influence of cathode material on the transport characteristics. The comparison of the charge transport mechanisms for capacitors with conducting polymer and manganese dioxide cathode will be performed.
- I will determine the parameters of Ta capacitor MIS model – namely concentration of donor states in the Ta₂O₅ layer and the height of energy barriers formed on the interface Ta₂O₅/cathode and Ta₂O₅/anode, respectively, from the evaluation of C-V characteristics and the parameters of tunneling current components.
- The application of different materials for the capacitor electrodes – the tantalum metal for anode and CP or MnO₂ for cathode – leads to the creation of unipolar device. The energy barriers formed on the interfaces Ta₂O₅/anode and Ta₂O₅/cathode vary for the difference between the work function of tantalum and work function of cathode material. From the evaluation of transport mechanisms employed in normal and reverse mode, respectively, I will assess the temperature dependence of energy barriers height with respect to the electrode material.
- From the evaluation of the space charge limited current component I will estimate the mobility of charge carriers in the capacitor structure for the temperatures below 100 K.

5. Experimental setup and measured samples

5.1. Sample description and preparation

The experiments were carried out on the tantalum SMD capacitors. The measurement and evaluation were performed for the 3 series of the tantalum capacitors with MnO₂ cathode called KM2012, CTSS2012 and with conductive polymer cathode called KOL2012. All parameters were estimated from the acquired results. The samples were prepared by anodic oxidation, which was described in the chapter about manufactory. Table 3 presents the manufacturer description of the samples: the capacity, rated voltage, tolerance and construction of the capacitor.

Tab. 2. Basic description of the samples from manufactory

Description of the samples			KOL2012	CTSS2012	KM2012
Capacity	<i>C</i>	[μF]	150	100	100
Rated voltage	<i>V</i>	[V]	6.3	6.3	6.3
Capacitance tolerance		[%]	20%	20%	20%
Case size	<i>A,B,C</i>	[-]	B	B	B

Figure 5.1 demonstrates the assembly of samples on the testing board with contacts. All samples were soldered on the board and tested separately before their testing in the vacuum cryostat at low temperatures.

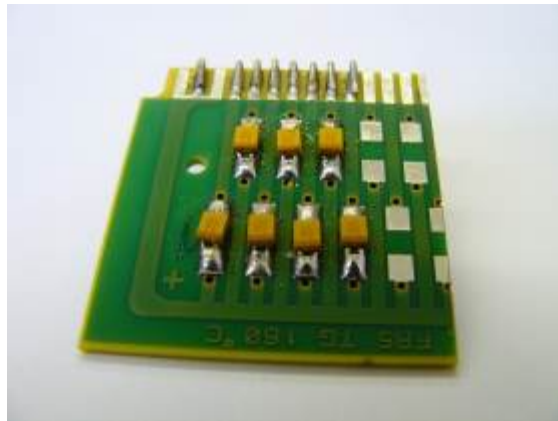


Fig. 5.1 The soldered samples on the testing board

The contacts of testing board were realized by gilt metal wires. The contacts are shown on the Fig. 5.2. The cathode side is separated for particular capacitors while anode side is shared. There are a various types of connections according to the measurement setup.

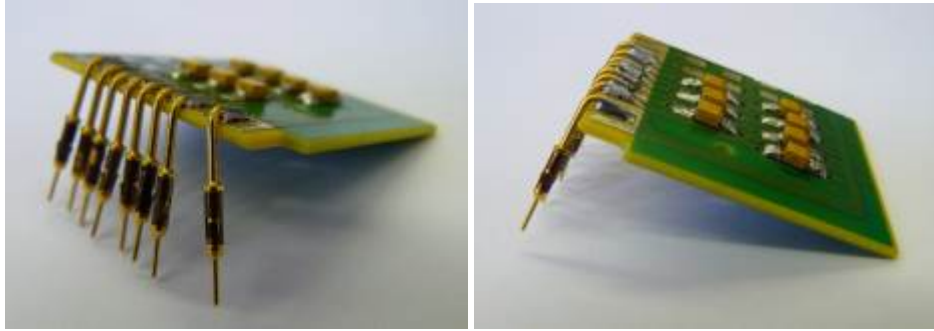


Fig. 5.2 The gilt metal wires connected for the each capacitor

Table 4 summarizes estimated parameters calculated from the measurement. The dielectric thickness is denoted by d , effective area of dielectric surface A , capacity C , relative permittivity ϵ_r , maximum voltage in normal mode and reverse mode $V_{max\ n,r}$, measuring temperature range T .

Tab. 3. Calculated parameters from measuring

Measured	Mark	Unit	KOL2012	CTSS2012	MK2012
Cathode type	-	-	CP	MnO ₂	MnO ₂
Capacity (low-high)	C	$[\mu F]$	149-154	99-103	98-104
Dielectric thickness	D	$[nm]$	42	35	45
Effective area of anode surface	A	$[cm^2]$	271	146	186
Relative permittivity	ϵ_r	$[-]$	27	27	27
Maximum voltage NM ¹	$V_{max\ n}$	$[\Omega]$	6.5	11	12
Maximum voltage RM ²	$V_{max\ r}$	$[-]$	2.7	1.8	3.5
temperature range	T	$[K]$	12-200		

¹ The maximum measuring voltage for the normal mode – anode is positive

² The maximum measuring voltage for the normal mode – anode is negative

5.2. SEM analysis of the structures

SEM analysis was performed for a sample of each series of tantalum capacitors. The samples were grinded to the half of their size and then were polished. The samples were placed in the epoxy resin, which is shown in the Fig. 5.3. Consequently the thin graphite layer was deposited on the surface to avoid structure charging during the SEM microscopy. The main goal of the SEM analysis was to calculate the thickness of Ta₂O₅ layers inside the capacitor. The thickness was calculated as a mean value from the measurement in 5 different points within each sample.



Fig. 5.3 Prepared samples for the SEM microscopy in epoxy resin

Fig. 5.4 presents cross-sections of whole capacitor structure in the case of samples CTS2012 and KOL2012.

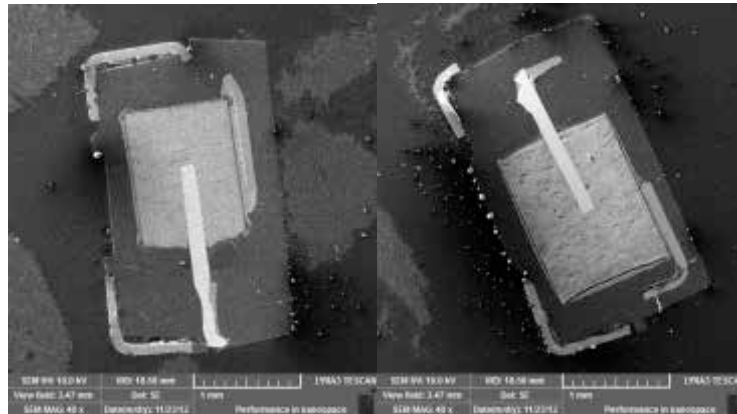


Fig. 5.4 SEM figures of whole capacitor structure cross-section for the samples CTS2012 and KOL2012

Fig. 5.5 demonstrates the sponge structure of tantalum capacitor anode where the sintered tantalum particles are covered by dielectric and conductive polymer layer.

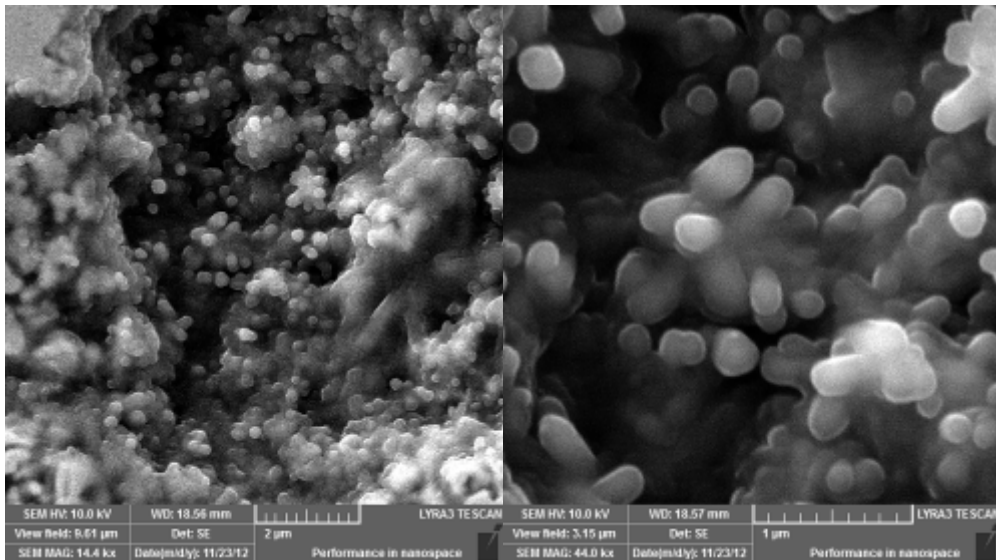


Fig. 5.5 SEM picture of porous tantalum anode for sample KOL2012

The thickness of the Ta₂O₅ layer depends on the anodic oxidation process. The thickness of dielectric layers was evaluated for all tested samples. Figures 5.6 to 5.8 show the analyzed samples where the thickness of Ta₂O₅ layer and cathode layer is pointed out.

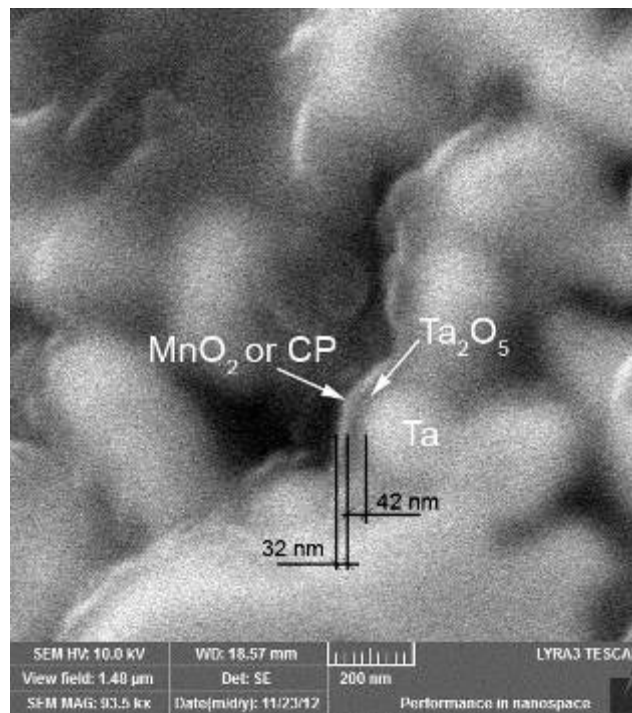


Fig. 5.6 SEM picture for sample KOL2012 for the determination of Ta₂O₅ and CP layer thickness

The calculated average thickness of Ta₂O₅ layer for sample KOL2012 is $d = 42$ nm, for sample CTS2012 $d = 35$ nm, and for sample MK2012 $d = 45$ nm. These values are summarized in Tab. 3 and are used for the calculation of other capacitor parameters as capacitor electrode area, electric field, etc.

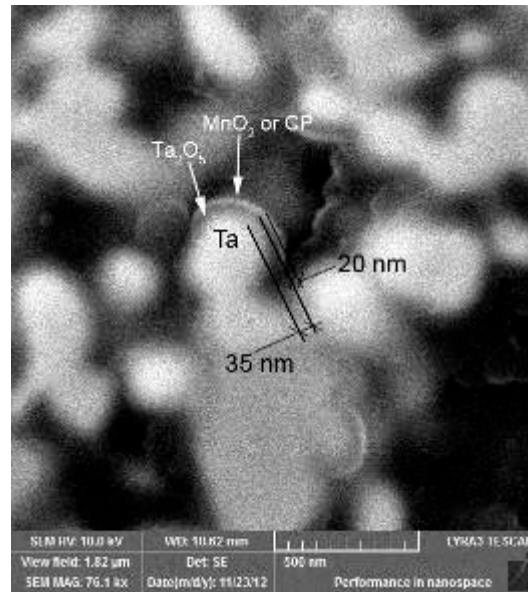


Fig. 5.7 SEM picture for sample CTS2012 for the determination of Ta₂O₅ and MnO₂ layer thickness

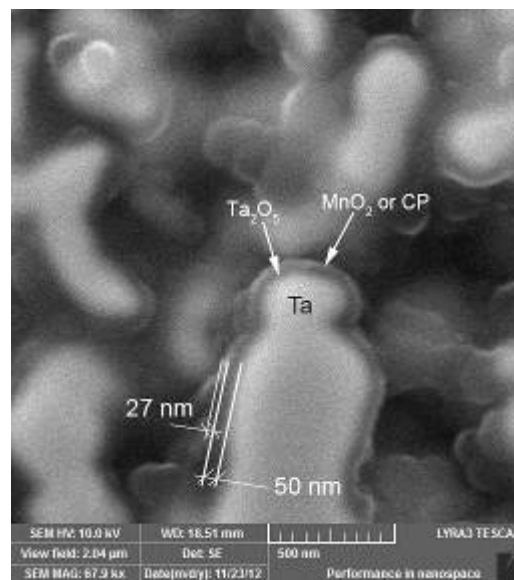


Fig. 5.8 SEM picture for sample MK2012 for the determination of Ta₂O₅ and MnO₂ layer thickness

5.3. *I-V* characteristics

The measurement of *I-V* characteristics gives the necessary data for analysis of transport mechanisms in the sample structures. The blocks scheme in Fig. 5.9 shows the experimental set-up for measuring *I-V* characteristics. The experiments were performed for temperature range from 10 to 300 K for the three series of the 7 samples in helium cryostat, and for temperature range from 80 to 300 K for 3 series for the 7 samples in nitrogen cryostat. The results were analyzed by the software developed in LabView environment. Power supplies HP4140B or Keithley 4400 were used as accurate power sources for precise setting voltage across the particular samples. During the experiments, the samples were located in the cryostat system. The values of signals were acquired by Agilent or Keithley, which were controlled by computer via GPIB bus. Relay arrays is controlled by RS232 and is used for measurement multiple samples (charging and discharging). Vacuum pump and helium pump are involved in experiments for the temperature range from 10 – 400 K. The temperature is set via the temperature controller (manufactured by company Lakeshore) and the sampling rate is setup in the range 0 to 100 K/min. The vacuum pump makes the vacuum inside the cryostat subsequently the helium pump pumping the gaseous helium inside the cryostat. The temperature stability is crucial for demand accuracy of measurements. The advantage of the system is measuring 7 samples inside the cryostat. For the slow charging or discharging of the samples it takes couple of days or weeks.

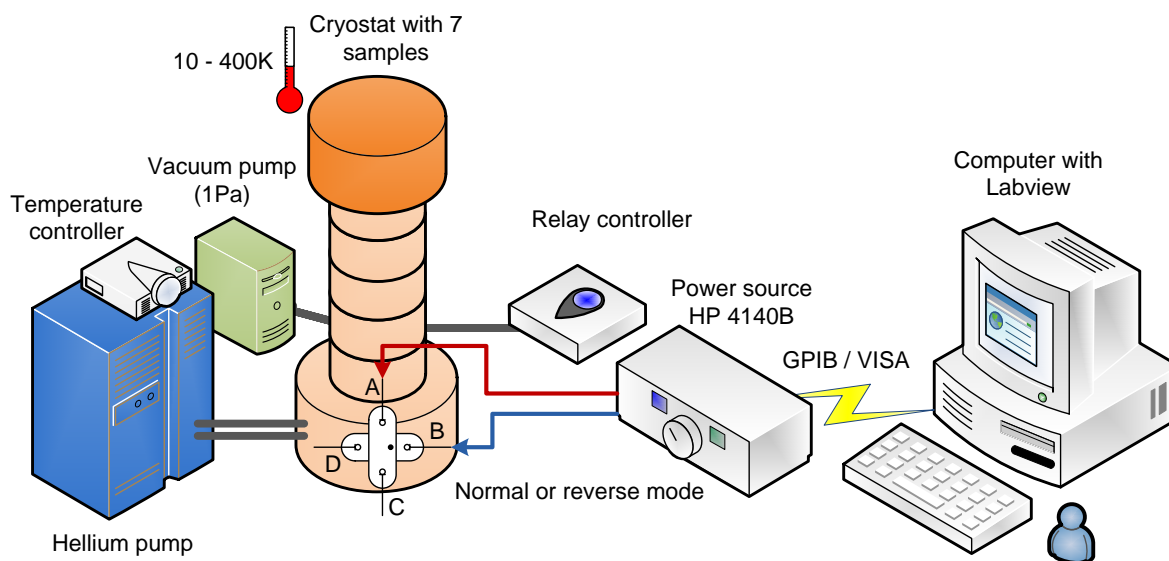


Fig. 5.9 The block scheme of *I-V* or *I-t* characteristics

To measure more than 7 samples simultaneously, the multiplexer Agilent 34970A could be used but the more connection places are needed on the cryostat system.

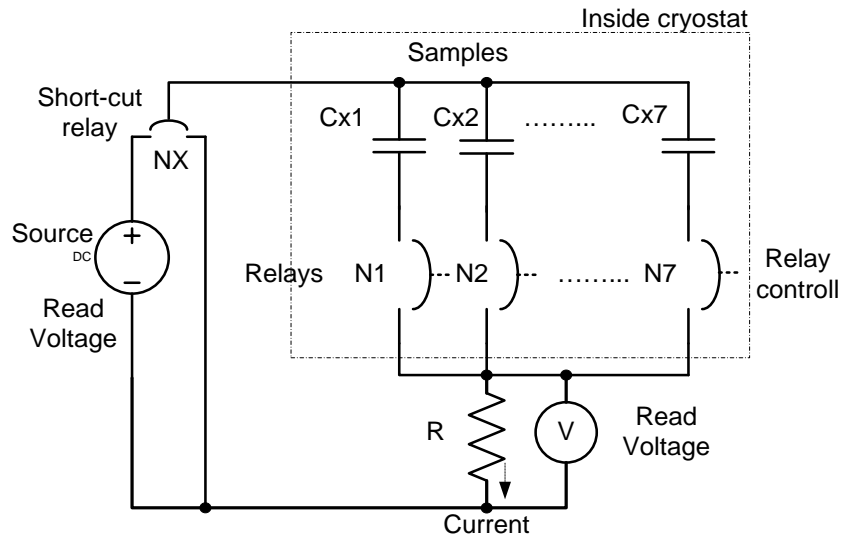


Fig. 5.10 The electrical circuit inside the cryostat system

Fig. 5.10 shows the electrical scheme inside the cryostat system. The measurement electrical circuit consists of DC source of resolution $1 \mu\text{V}$ up to 100 V, the relays NX, N1-N7 for the measuring the each sample, samples Cx1-Cx7 and loading resistance R_{load} . The voltage across particular capacitor is estimated by acquisition of R_{load} voltage and calculation in the software.

The relays N1, NX are switched on and the sample Cx1 is charged and on the load resistor is obtaining voltage. The time constant of charging (RC) may play crucial role during the I-V measurement, thus the time delay between measurements was set to be 5-10 times of time constant to avoid polarization current influence.



Fig. 5.11 Real connections of the cryostat system

The different types of measuring I - V characteristics were provided with this experimental setup. I - V characteristics were measured both in steady state and under quasi-stationary conditions:

- The steady state was realized by applying the step voltage across the sample. The time dependence of the leakage current was measured during the capacitor charging and discharging. Charging characteristics give information about the charge carrier transport and storage ability for high electric field, while discharging characteristics give information about low electric field transport.
- Quasi-stationary state was realized by the application of slowly varying ramp of small-step voltages ($\Delta V = 0.1$ V) and the electrical current was measured after 10 s. Equilibrium is assumed to be achieved under these conditions. However, the measured leakage current was slightly higher than that in stationary state due to the polarization current component. Leakage current error was less than 0.3 mA.

At low electrical fields the charge carrier mobility is constant because scattering relaxation constant is field independent. At high fields the charge carriers do not lose their excess energy in scattering events and their mean energy increases (so called hot carriers). As a consequence the scattering relaxation constant becomes electrical field dependent as well as the sample conductivity. I - V characteristic can be divided into three regions. In the first region (low fields) the Ohm's law is valid because the charge carrier mobility is constant and drift velocity is proportional to electric field strength. In the intermediate region, conductivity decreases due to the decrease of the mobility. Corresponding drift velocity approaches the value of thermal velocity v_{ds} about 10⁵ m.s⁻¹. I suppose that critical electric field is about 10 MV.m⁻¹. This electric field would correspond to the voltage 1 V applied to capacitor with the insulating layer of thickness $d = 100$ nm. From this reason I - V characteristic is not ohmic and current is decreasing function of applied voltage. In the last region the conductivity decreases with increasing voltage and current reaches its saturation value. This knowledge is verified by the experimental results.

Fig. 5.12 shows experimental data where sample KOL2012 - 02 was measured for the temperature range from 12 K up to 150 K for both directions of current throw the structure means normal and reverse mode.

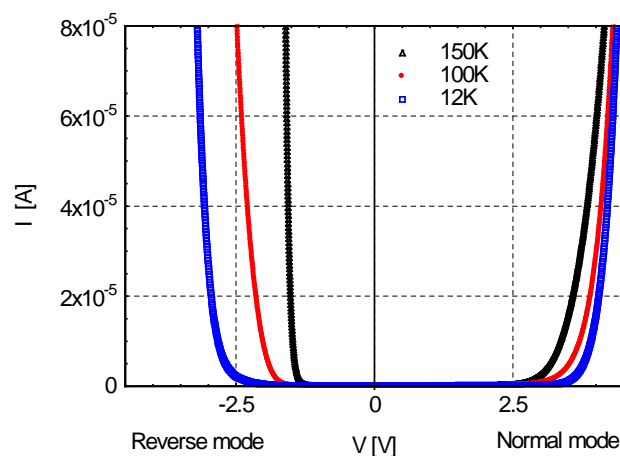


Fig. 5.12 I - V characteristics for sample KOL2012 -02 for the normal and reverse mode from 12 K up to 150 K

5.4. *C-V* characteristics

The dependence for capacitance on DC bias voltage at different temperatures was measured according the scheme in Fig. 5.13. The same cryostat system, which was used for the *I-V* characteristics measurements, was involved in the *C-V* measurements at the wide temperature range. The measurement set-up includes also LCR meter Agilent HP E4980A for *C-V* characteristics measuring. The RLC meter measures series capacitance, and is adjustable in the frequency range from 20 Hz up to 2 MHz and for the DC voltage up to ± 40 V. For the parallel measuring of more samples the switching relays are included. The connections are realized with coaxial cables. Special software in the LabVIEW was developed for measurement and evaluation of acquired data.

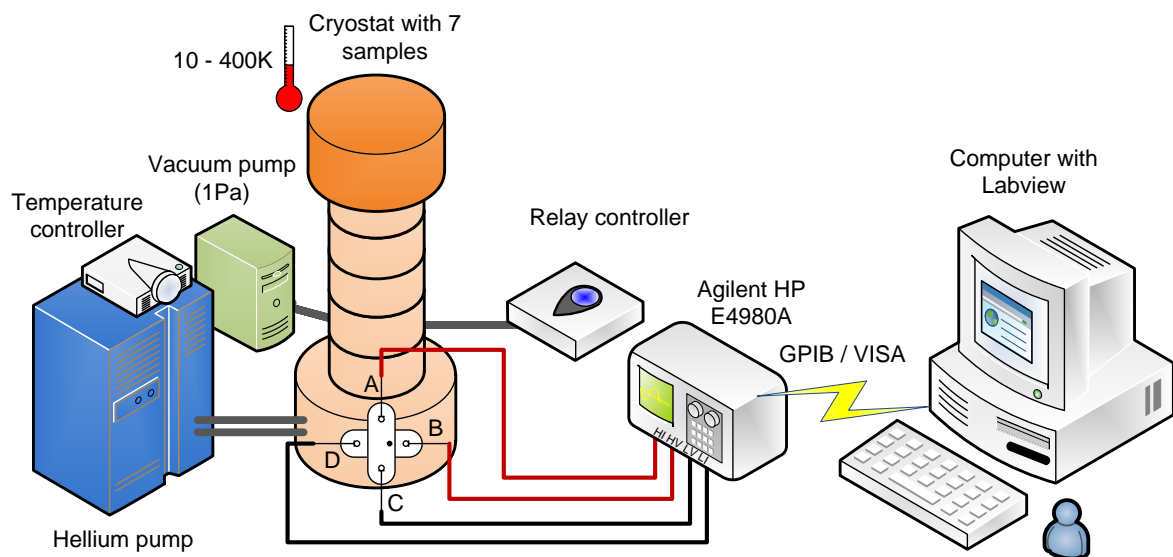


Fig. 5.13 Block scheme of the *C-V* measurement

The electric circuit inside in the cryostat system is shown in Fig. 5.14. RLC meter is connected via the relays and the capacity is measured successively on the each sample C_{x1} - C_{x7} . The relays are denoted as N1-N7. The relay is connected on the measured capacitor, then the voltage is applied on the sample and subsequently the RLC meter read the capacity. The temperature was changed and stabilized and then the capacity was measured for the required voltage range.

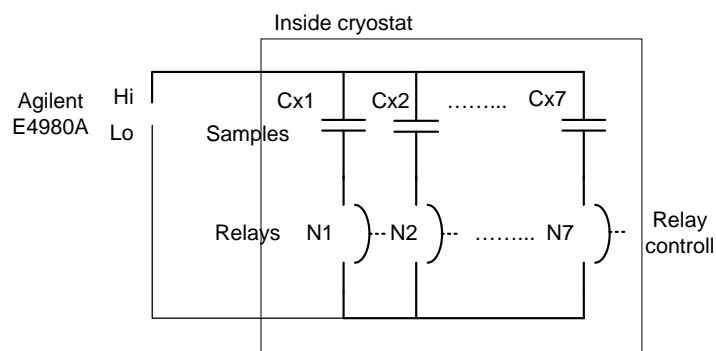


Fig. 5.14 Electric circuit inside in the cryostat system for *C-V* characteristics measurements

The concentrations of localized-energy states in insulating layer can be determined from C-V characteristics measured for reverse bias voltage (reverse bias mode). The capacitance of Ta capacitors is in normal mode slightly dependent on applied voltage while in the reverse bias mode there is a strong capacitance change with applied voltage as shown in Fig. 5.15. This effect depends on temperature dependent where capacitance increases with increasing temperature.

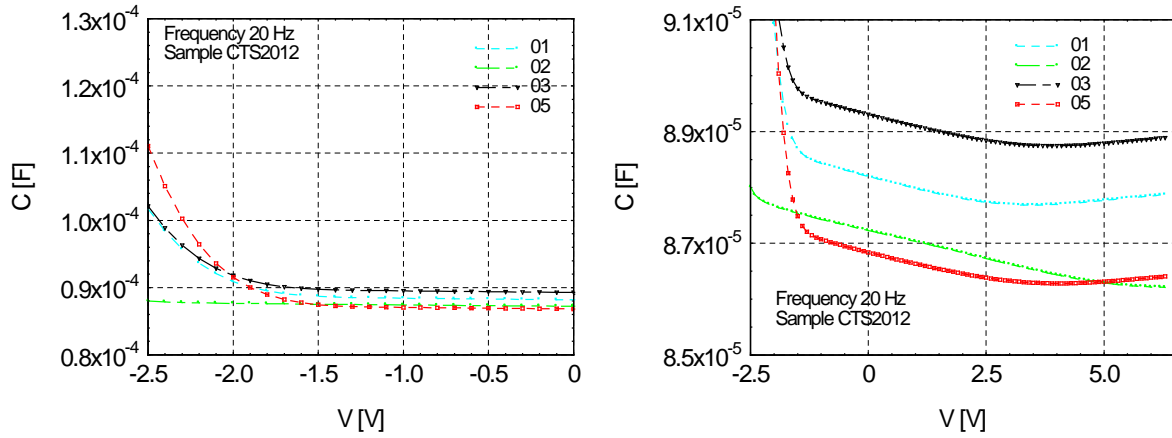


Fig. 5.15 C-V characteristics for 5 samples of CTS2012 series measured at frequency 20 Hz for temperature 300 K

Increase of capacitance in the reverse bias mode can be explained under the assumption of a potential barrier existence in the capacitor system. For the voltage lower than diffusion potential U_D , the current is controlled by barrier on interface MnO₂ – Ta₂O₅, or CP – Ta₂O₅ respectively. The capacitance of the system is influenced by the depletion region in Ta₂O₅ layer.

The capacitance C vs. applied voltage U in the reverse mode is given by a formula:

$$C = A \frac{\epsilon e e_r e_0 N_D}{\epsilon^2 (U_D + U)} U^{1/2} \quad (5.1)$$

Where e is elementary charge, ϵ is the electric permittivity, N_D is the donor concentration, U_D is the diffusion voltage and A is the capacitor area. In this case the square of inverse capacitance $1/C^2$ is a linear function of applied voltage U as is shown in Fig. 5.16. From the experimental results diffusion voltage U_D and donor concentration N_D can be determined.

Diffusion voltage V_D is determined from the intersection between fitting line and x-axis for inverse capacitance $1/C^2 = 0 \text{ F}^{-2}$. The value of diffusion voltage increases with decreasing temperature (see Fig. 5.16). Diffusion voltage value corresponds to the potential barrier on the interface between Ta₂O₅ and cathode.

Donor concentration is determined using the slope of fitting line from the formula (derived from equation 5.1):

$$m = \frac{2}{A^2 e e_r e_0 N_D} \quad \text{and} \quad N_D = \frac{2}{mA^2 e e_r e_0} \quad (5.2)$$

Having these parameters: area $A = 146 \text{ cm}^2$, $\epsilon_r = 27$ and the slope of $1/C^2 = f(U)$, $m = 1 \times 10^8 \text{ F}^{-2} \text{ V}^{-1}$. Calculated donor concentration is $N_D = 2.6 \times 10^{18} \text{ cm}^{-3}$ in this case. It is supposed

that donors are oxygen vacancies and their concentration depends on anodic oxidation conditions.

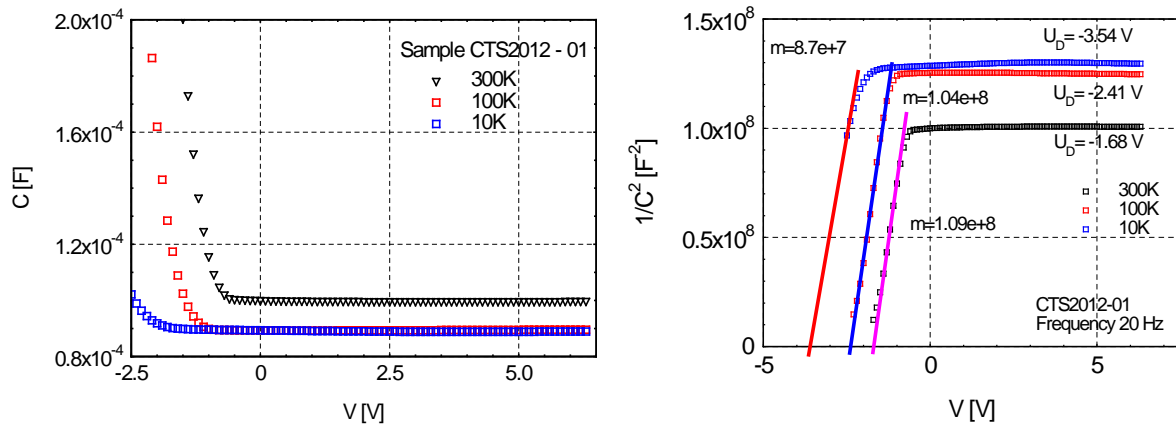


Fig. 5.16 $1/C^2$ vs. voltage for sample CTS2012-01 for temperatures 10 K, 100 K, 300 K

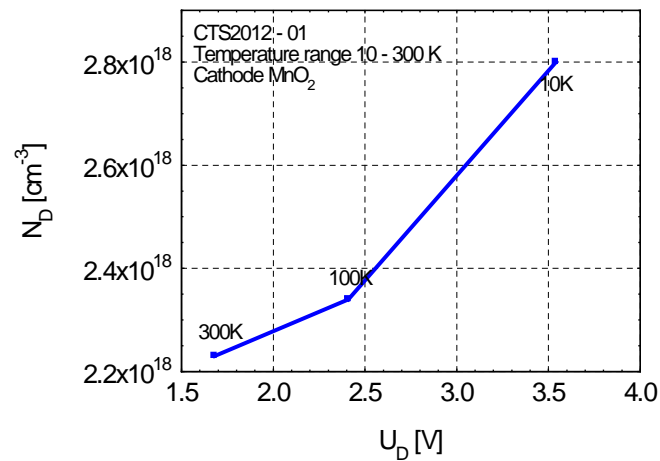


Fig. 5.17 N_b vs. U_b for sample CTS2012-01 for temperatures 10 K, 100 K, 300 K

Figure 5.17 shows the correlation between the diffusion voltage and donor concentration for sample CTS2012 – 01 for different temperature range. Diffusion voltage and the value of the donor concentration are both inversely proportional to the temperature.

6. Experimental results

6.1. Analysis of C - V characteristics for 10 K up to 300 K

The capacity measurements were performed on 4 samples from each series. C - V characteristics for these samples were measured for the temperatures 10 K, 100 K and 300 K for series CTS2012 and MK2012, and at temperature 300 K for samples of KOL2012. The capacitance of tantalum capacitors is slightly dependent on the DC bias voltage in the normal mode while strong dependence on DC bias voltage is observed in the reverse mode. DC bias voltage was set in the range -3 V up to 6.3 V and the capacitance was measured for frequency 20 Hz. The C - V characteristics at room temperature for 4 samples for series CTS2012 are shown in Fig. 5.15. The C - V characteristics at temperatures 10 K, 100 K and 300 K for samples for CTS2012-03 and CTS2012-05 are shown in Figs. 6.1 and 6.2.

From C - V characteristics the dependence of square of inverse capacitance vs. bias voltage where calculated. $1/C^2$ vs. voltage plot for samples CTS2012 - 01, CTS2012 - 03 and CTS2012 - 05 for temperatures 10 K, 100 K, 300 K are shown in Figs. 5.16, 6.1 and 6.2. We can see that inverse capacitance value in normal mode increases with decreasing temperature, i.e. capacitance value decreases with temperature.

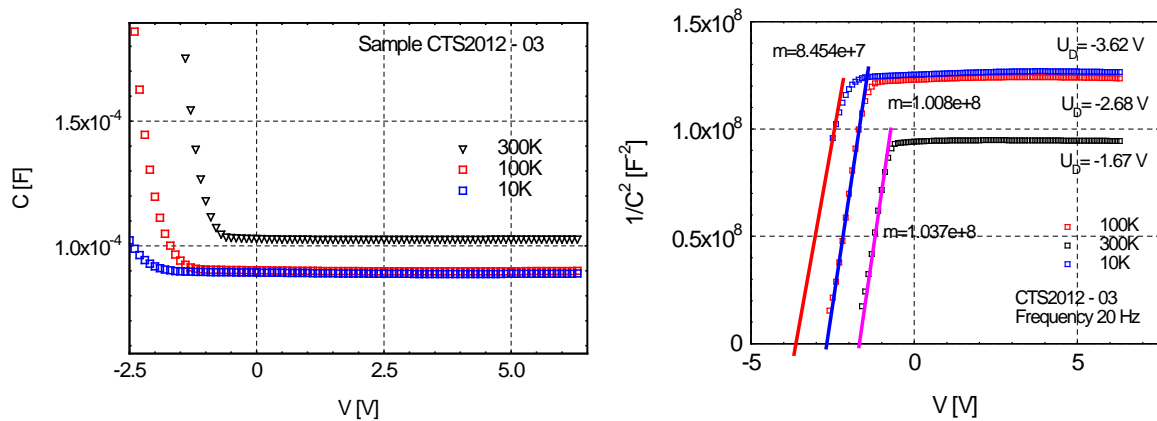


Fig. 6.1 Measured dependence C vs. voltage and calculated dependence $1/C^2$ vs. voltage for sample CTS2012-03 for temperatures 10 K, 100 K, 300 K

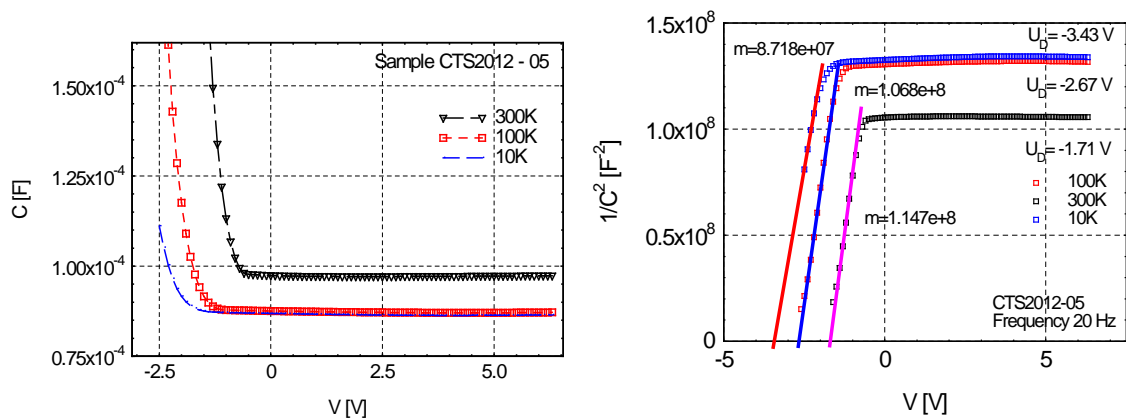


Fig. 6.2 Measured dependence C vs. voltage and calculated dependence $1/C^2$ vs. voltage for sample CTS2012-05 for temperatures 10 K, 100 K, 300 K

From these plots the diffuse voltage value U_D and the slope of $1/C^2$ vs. V for reverse mode was determined. According the equation 5.2 the donor concentration was calculated from the slope of fitting line.

The correlation between the diffuse voltage, donor concentration and temperature was found; with decreasing temperature the value of both diffusion voltage and the value of the donor concentration increase (see Figs. 5.17, 6.3 and 6.4).

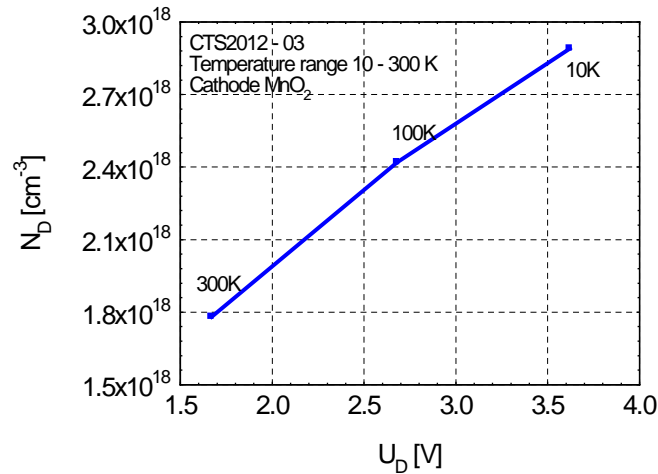


Fig. 6.3 Donor concentration N_D vs. U_D for sample CTS2012-03 for temperatures 10 K, 100 K, 300 K

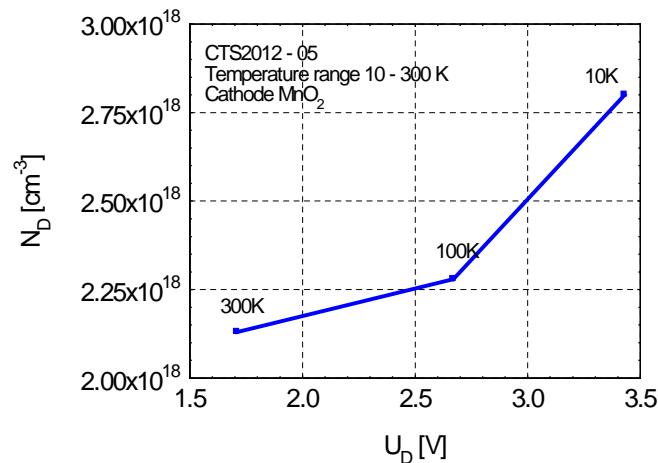


Fig. 6.4 Donor concentration N_D vs. U_D for sample CTS2012-05 for temperatures 10 K, 100 K, 300 K

Measured C - V characteristics and calculated $1/C^2$ vs. voltage plot for samples MK2012 – 01, MK2012 – 02 and MK2012 – 03 for temperatures 10 K, 100 K, 300 K are shown in Figs. 6.5, 6.6 and 6.7, respectively. The value of diffusion voltage and concentration of donors was possible to determine only from the characteristic measured at temperature 300 K.

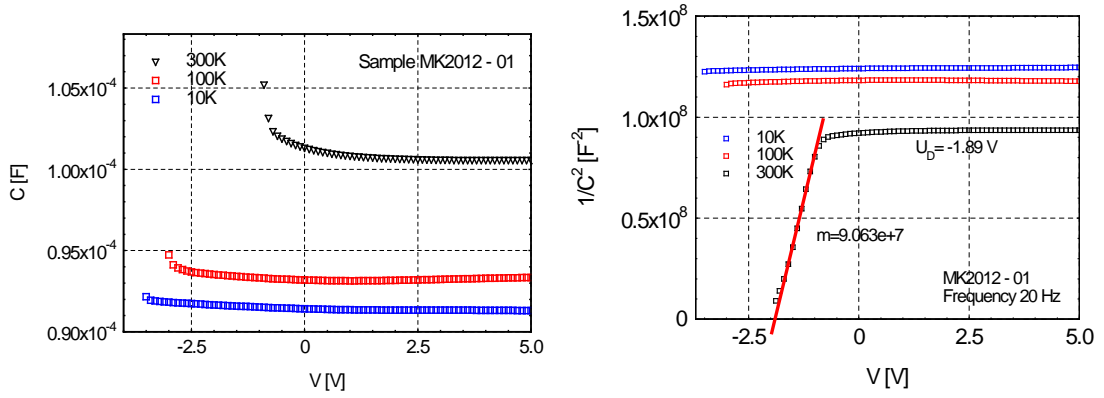


Fig. 6.5 Measured dependence C vs. voltage and calculated dependence $1/C^2$ vs. voltage for sample MK2012-01 for temperatures 10 K, 100 K, 300 K

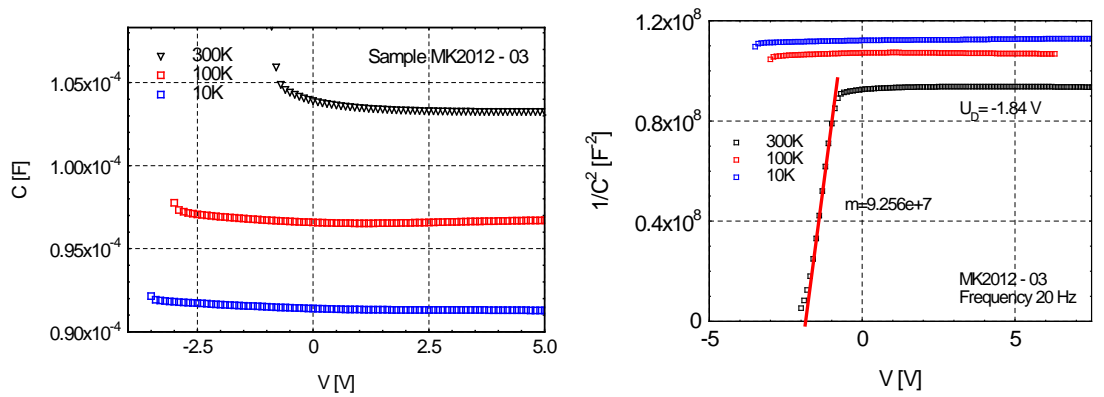


Fig. 6.6 Measured dependence C vs. voltage and calculated dependence $1/C^2$ vs. voltage for sample MK2012-03 for temperatures 10 K, 100 K, 300 K

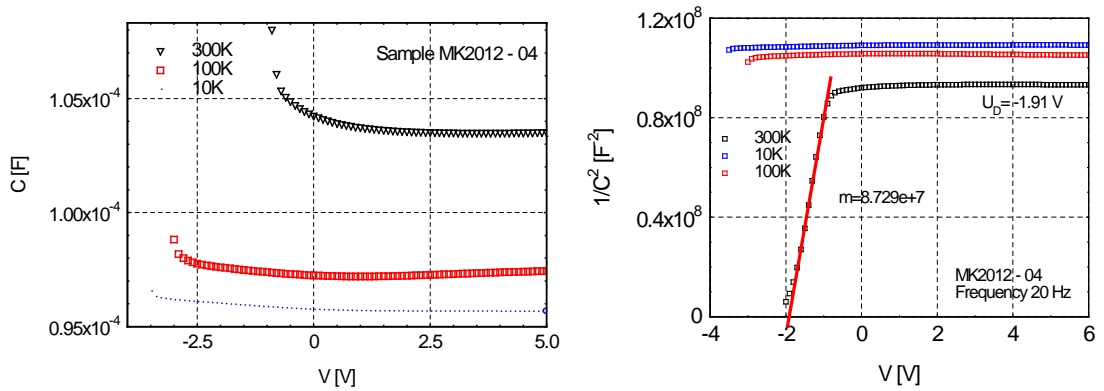


Fig. 6.7 Measured dependence C vs. voltage and calculated dependence $1/C^2$ vs. voltage for sample MK2012-04 for temperatures 10 K, 100 K, 300 K

The dependence of the diffuse voltage on donor concentration for temperature 300 K is shown in Fig. 6.8. We can see that diffuse voltage increases with increasing donor concentration value for different samples within this series.

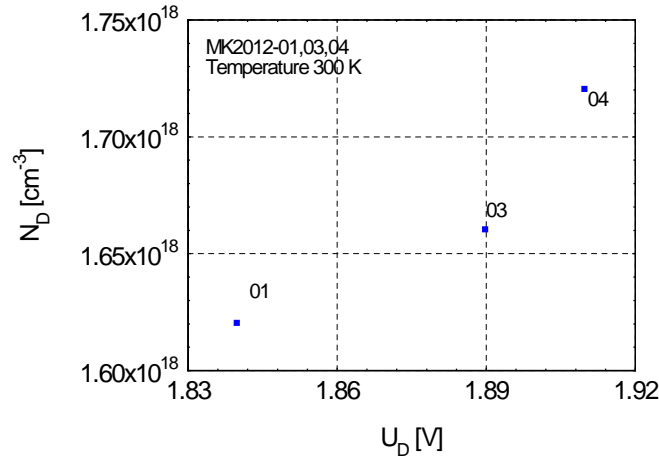


Fig. 6.8 Donor concentration N_D vs. U_D for sample MK2012-01, MK2012-03, MK2012-04 for temperature 300 K

Measured dependence C vs. voltage and calculated dependence $1/C^2$ vs. voltage for samples KOL2012 – 01, MK2012 – 03 and MK2012 – 05 for temperature 300 K is shown in Fig. 6.9. The measurements on temperatures 10 K and 100 K were not performed.

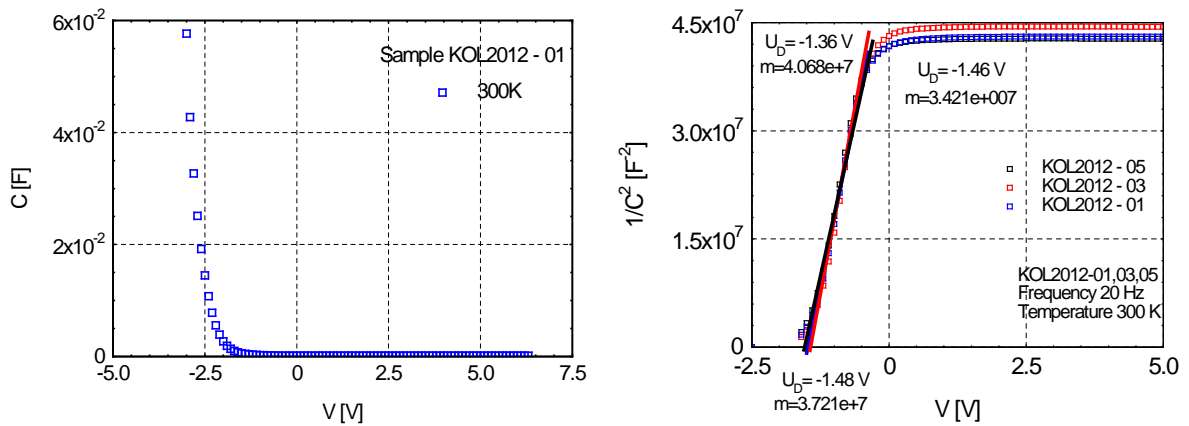


Fig. 6.9 Measured dependence C vs. voltage and calculated dependence $1/C^2$ vs. voltage for samples KOL2012 – 01, KOL2012 – 03, KOL2012 – 05 for temperature 300 K

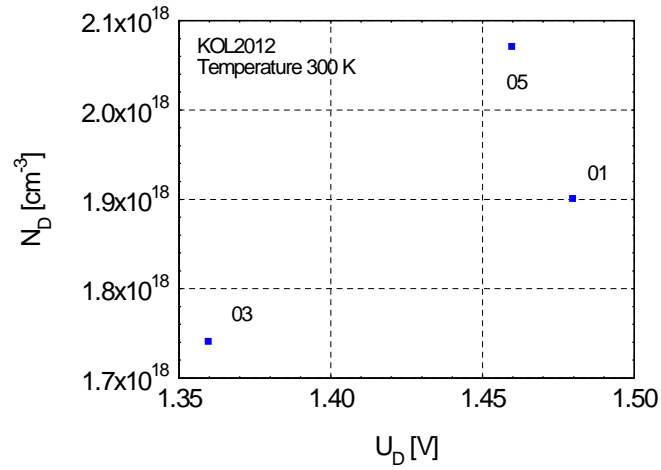


Fig. 6.10 Donor concentration N_D vs. U_D for sample KOL2012-01, KOL2012-03, KOL2012-05 for temperature 300 K

The correlation between the diffuse voltage and donor concentration for temperature 300 K is shown in Figs. 6.10. In the first approximation the donor concentration increases with diffuse voltage value.

We mentioned that capacitance decreases with decreasing temperature probably due to permittivity dependence on temperature.

6.2. Analysis of I - V measurements

Measured I - V characteristics were evaluated firstly by fitting with analytical function corresponding to considered charge transport mechanism and secondly by graphical method suitable for appropriate current component analysis. The evaluation of these results was verified by comparison of mentioned methods.

For each studied series of capacitors 3 samples were measured in the temperature range from 12 K up to 250 K.

I - V characteristics in normal and reverse mode for the sample KOL2012 – 02 with CP cathode in temperature range from 12 K up to 150 K are shown in Fig. 6.11.

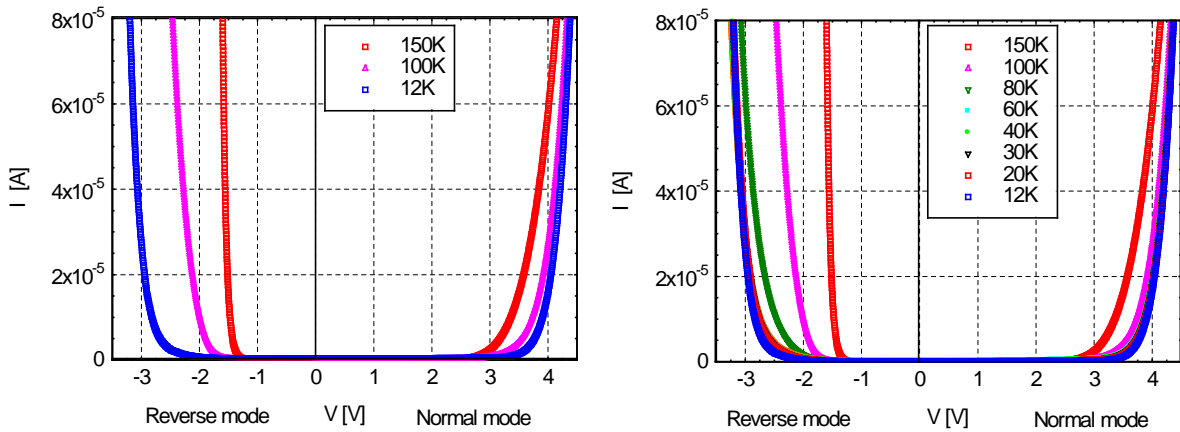


Fig. 6.11 I - V characteristics for sample KOL2012 – 02 in the temperature range from 12 K up to 150 K for the normal and reverse mode, left graph shows I - V characteristics for selected temperatures

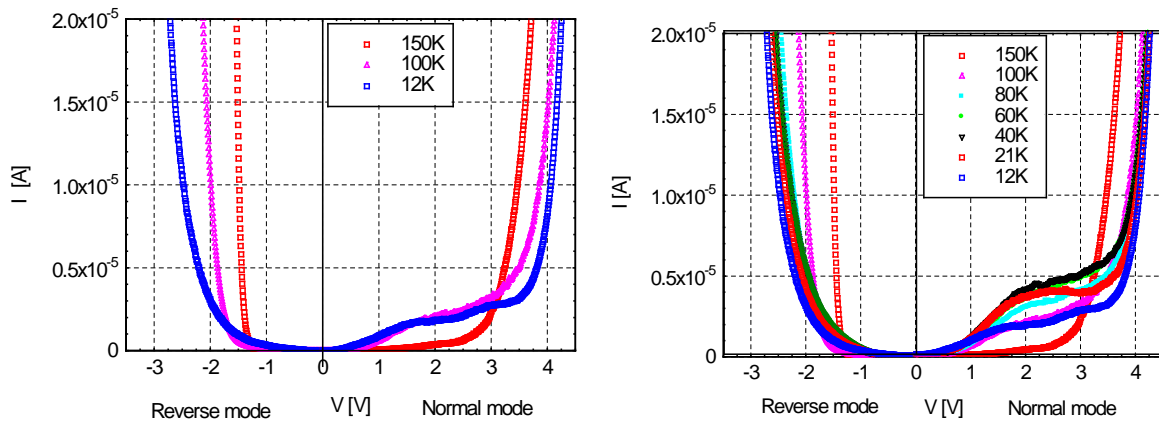


Fig. 6.12 I - V characteristics for sample KOL2012 – 03 in the temperature range from 12 K up to 150 K for the normal and reverse mode, left graph shows I - V characteristics for selected temperatures

I - V characteristics in normal and reverse mode for the sample KOL2012 – 03 with CP cathode in temperature range from 12 K up to 150 K are shown in Fig. 6.12. This sample exhibits trap assisted tunneling current pronounced at the low electric field. This current behavior is discussed further in Chapter 6.2.3.

I - V characteristics in normal and reverse mode for the sample KOL2012 – 05 with CP cathode in temperature range from 12 K up to 150 K are shown in Fig. 6.13. The measurements of I - V characteristics performed on tantalum capacitors with CP cathode show that DCL decreases with decreasing temperature both in normal and reverse modes.

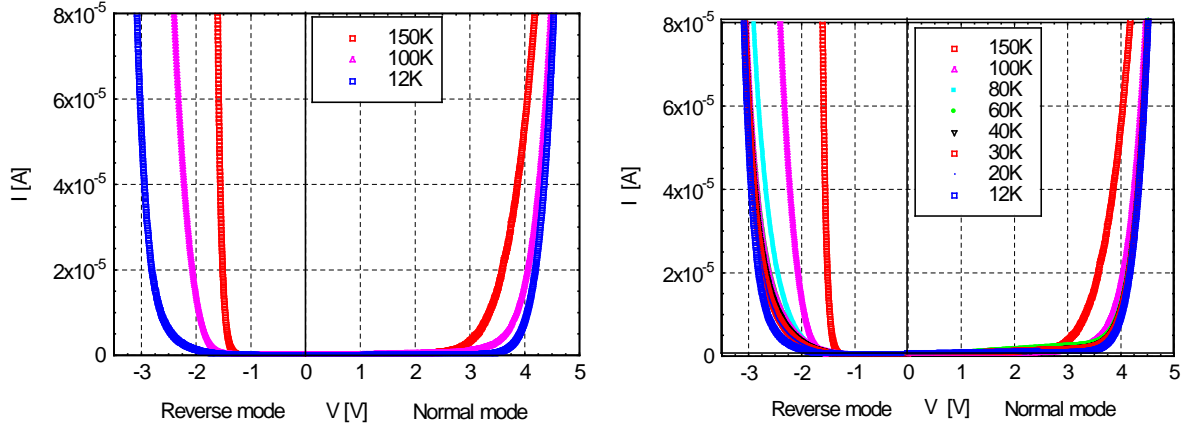


Fig. 6.13 I - V characteristics for sample KOL2012 – 05 in the temperature range from 12 K up to 150 K for the normal and reverse mode, left figure shows I - V characteristics for selected temperatures

I - V characteristics in normal and reverse mode for the samples with MnO₂ cathode CTS2012 – 01 and CTS2012 - 04 for the temperatures 12 K, 100 K and 150 K are shown in Figs. 6.14 and 6.15.

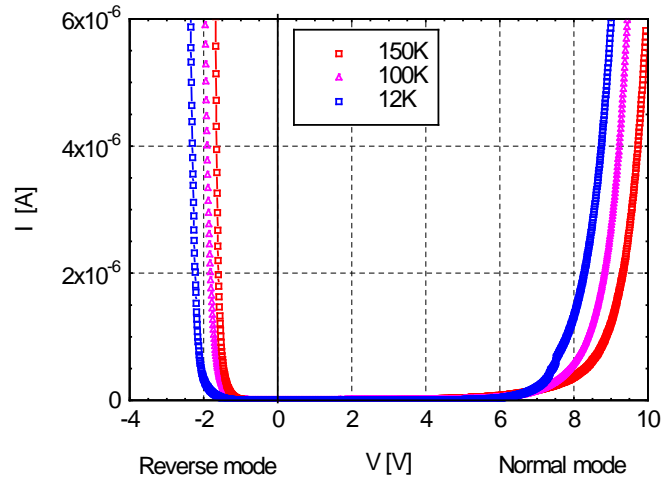


Fig. 6.14 I - V characteristics for sample CTS2012 – 01 for the temperatures 12 K, 100 K and 150 K for the normal and reverse mode

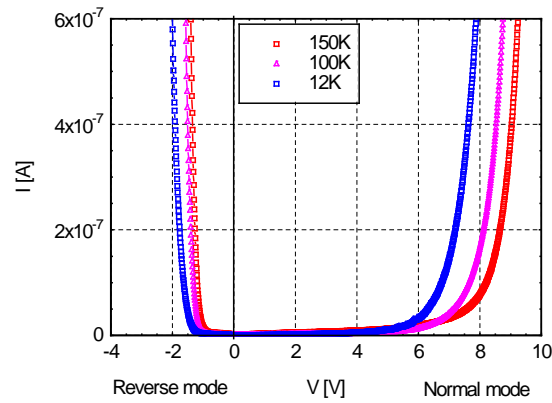


Fig. 6.15 *I - V* characteristics for sample CTS2012 – 04 for the temperatures 12 K, 100 K and 150 K for the normal and reverse mode

I-V characteristics in normal and reverse mode for the samples with MnO₂ cathode MK2012 – 01, MK2012 – 02 and MK2012 – 03 for the temperatures 12 K, 100 K and 150 K are shown in Figs. 6.16 to 6.18.

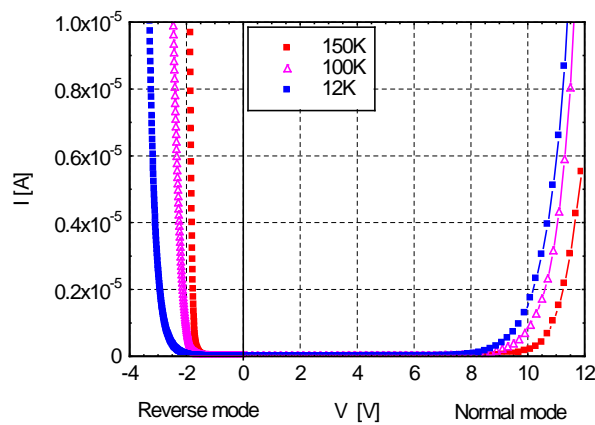


Fig. 6.16 *I - V* characteristics for sample MK2012 – 01 in the temperature range from 12 K up to 150 K for the normal and reverse mode

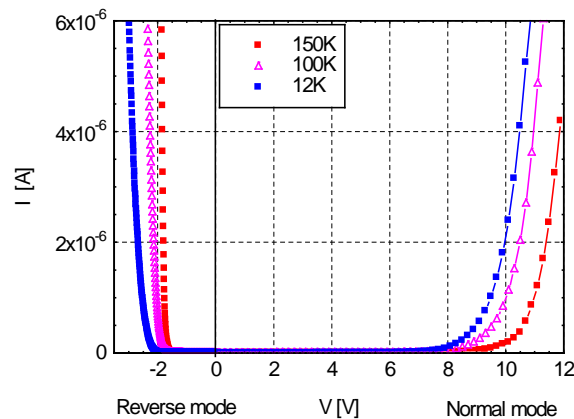


Fig. 6.17 *I - V* characteristics for sample MK2012 – 02 in the temperature range from 12 K up to 150 K for the normal and reverse mode

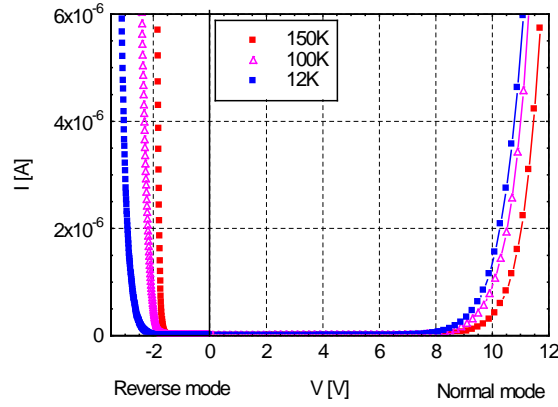


Fig. 6.18 I - V characteristics for sample MK2012 – 03 in the temperature range from 12 K up to 150 K for the normal and reverse mode

We can see that the leakage current value increases with decreasing temperature for voltage bias in normal, while for the reverse bias the DCL decreases with decreasing temperature. This behavior is observed for the samples with MnO₂ cathode, both from series CTS2012 and MK2012.

6.2.1. Analytical method for DCL components determination in normal mode

Measured *I-V* characteristics were evaluated using analytical method in order to estimate the contribution of particular charge transport mechanisms to the total DCL value at different temperatures. It is supposed, that at temperature below 100 K only ohmic and tunneling current components are involved, while at higher temperatures the contribution of Poole-Frenkel component must be also taken into account. However the contribution of PF current to the DCL was very small even for temperatures 100 K and 150 K for the evaluated samples and measured data were successfully approximated considering ohmic and tunneling current only.

Figures 6.19 and 6.20 show analytical method for the analysis of data measured for samples KOL2012 – 02 and KOL2012 – 05 for the normal mode for temperature range from 12K up to 150 K. An equation covering the ohmic and tunneling current components was used for measured dependence fitting.

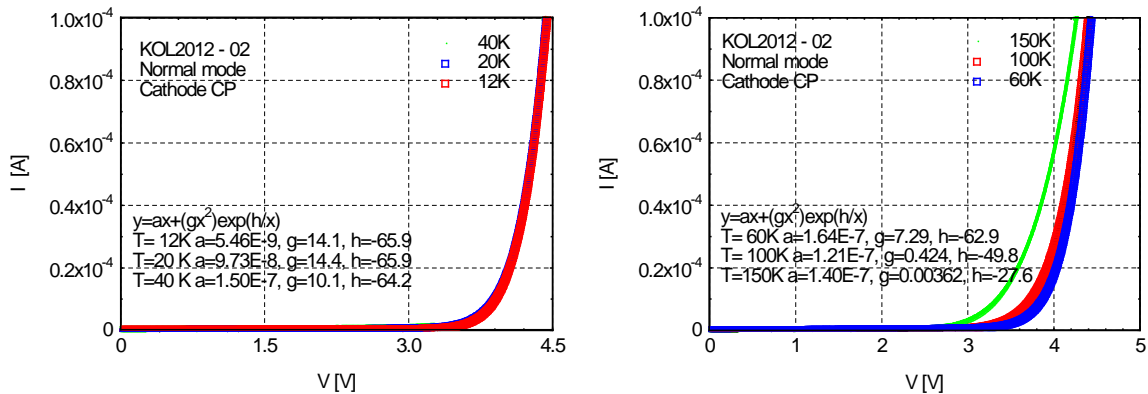


Fig. 6.19 Analytical method for the analysis of data measured for sample KOL2012 - 02 in normal mode for temperature range from 12 K up to 150 K

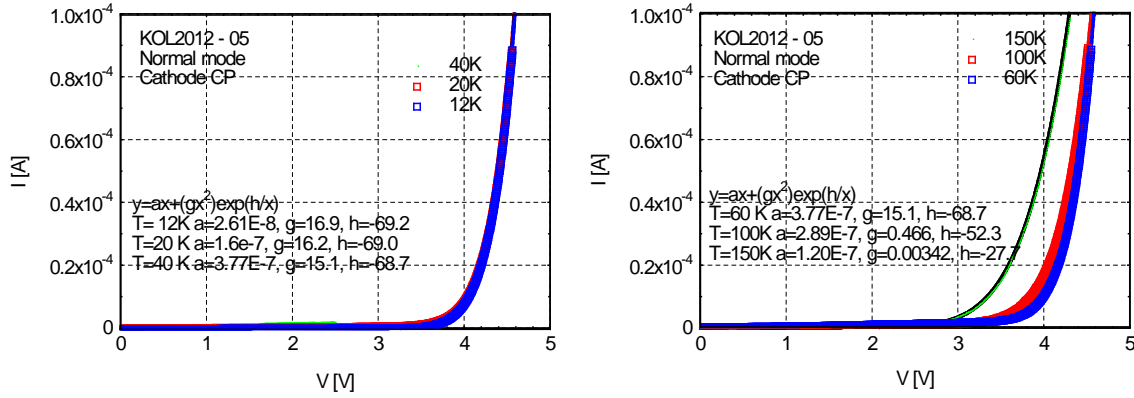


Fig. 6.20 Analytical method for the analysis of data measured for sample KOL2012 - 05 in normal mode for temperature range from 12 K up to 150 K

The analytical method by fitting was performed for all samples. Figures 6.21 and 6.22 show analytical method for the analysis of data measured for samples CTS2012 – 01 and CTS2012 – 04 for the normal mode for temperature range from 12K up to 150 K.

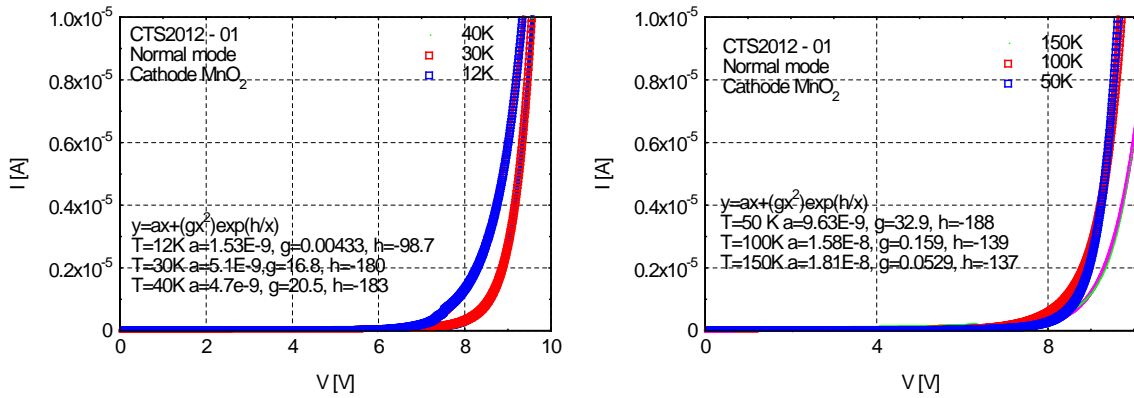


Fig. 6.21 Analytical method for the analysis of data measured for sample CTS2012 - 01 in normal mode for temperature range from 12 K up to 150 K

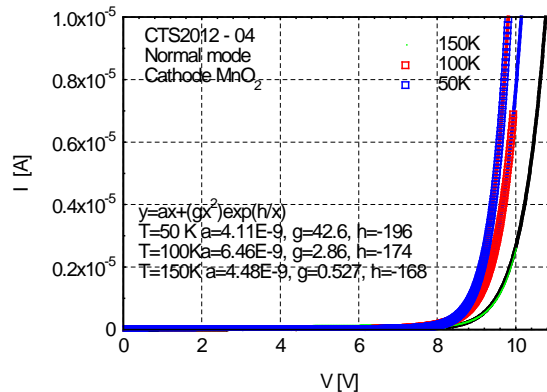


Fig. 6.22 Analytical method for the analysis of data measured for sample CTS2012 - 04 in normal mode for temperature range from 12 K up to 150 K

Figures 6.23, 6.24 and 6.25 show analytical method for the analysis of data measured for samples MK2012 - 01, MK2012 - 02, and MK2012 - 03 for the normal mode for temperature range from 12K up to 150 K.

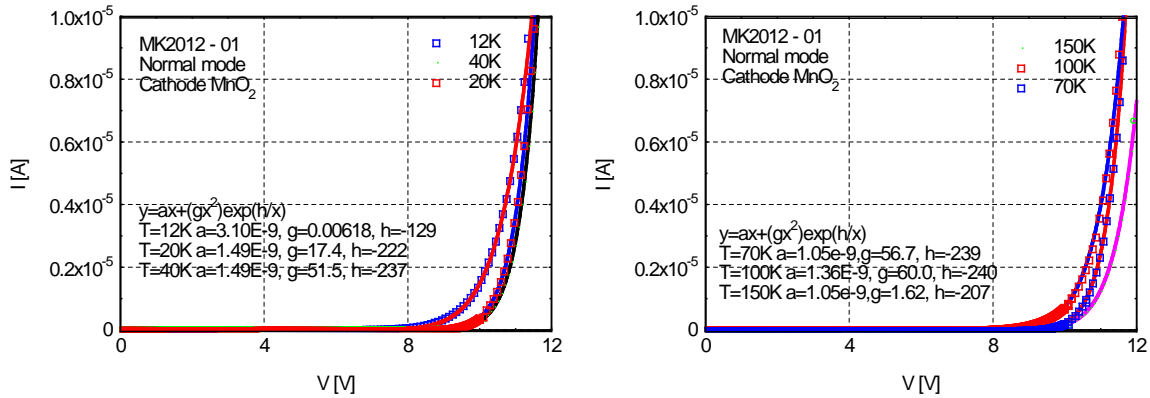


Fig. 6.23 Analytical method for the MK2012 - 01 in normal mode for temperature range from 12 K up to 150 K

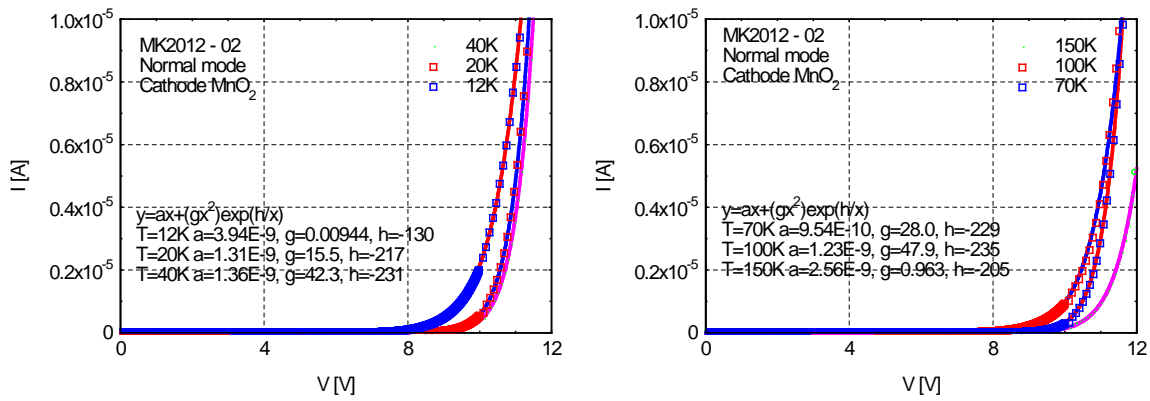


Fig. 6.24 Analytical method for the analysis of data measured for sample MK2012 - 02 in normal mode for temperature range from 12 K up to 150 K

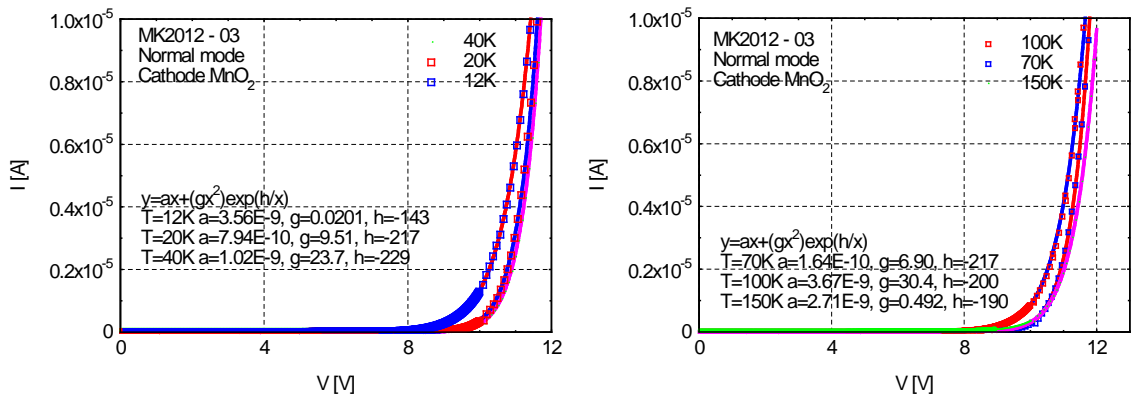


Fig. 6.25 Analytical method for the analysis of data measured for sample MK2012 - 03 in normal mode for temperature range from 12 K up to 150 K

The parameters of tunneling current component in normal mode obtained from the analytical method shown in Figs. 6.19 to 6.25 will be evaluated further in Chapter 6.2.4.1.

6.2.2. Analytical method for DCL components determination in reverse mode

Measured I - V characteristics in reverse mode were evaluated using analytical method in order to estimate the contribution of particular charge transport mechanisms to the total DCL value at different temperatures. We consider only the ohmic and tunneling current components at temperatures below 100 K, while at higher temperatures the contribution of thermionic emission limited current component must be also taken into account.

Figures 6.26, 6.27 and 6.28 show analytical method for the analysis of data measured for samples KOL2012 - 02, KOL2012 - 03 and KOL2012 - 05 for the reverse mode for temperature range from 12K up to 100 K. An equation covering the ohmic and tunneling current components was used for measured dependence fitting.

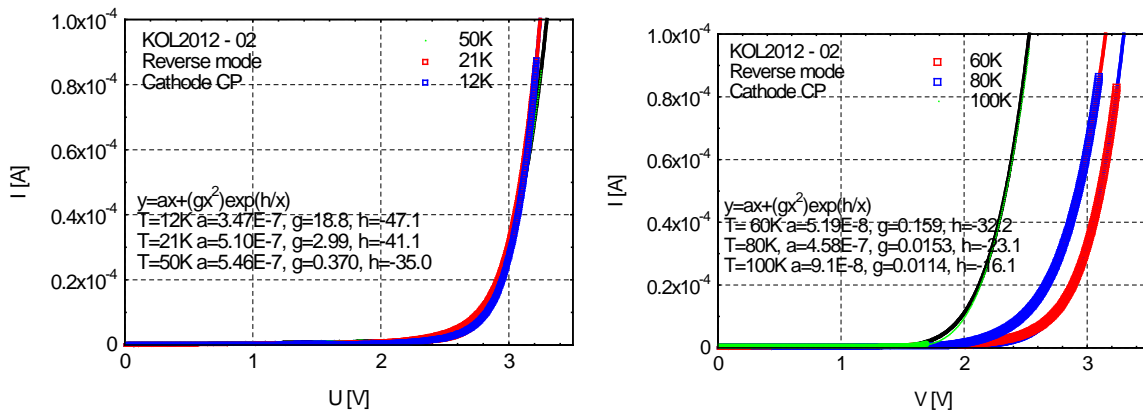


Fig. 6.26 Analytical method for the analysis of data measured for sample KOL2012 - 02 in reverse mode for temperature range from 12 K up to 100 K

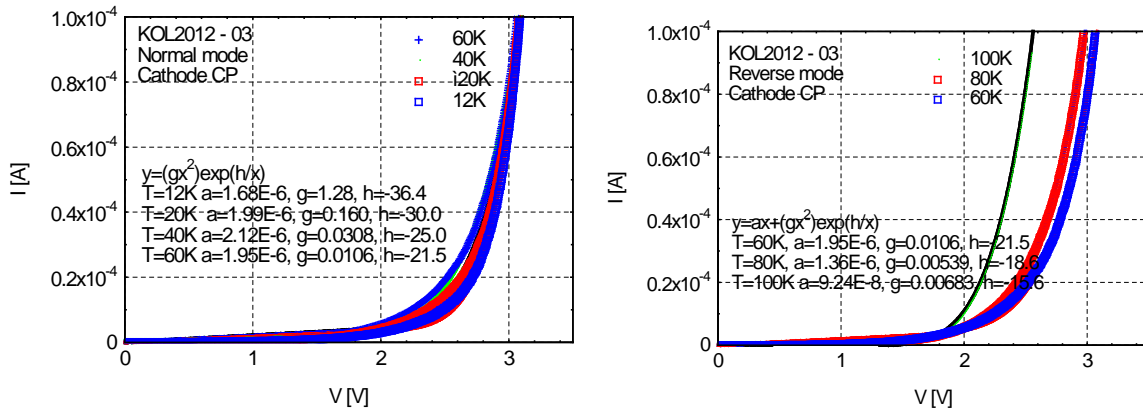


Fig. 6.27 Analytical method for the analysis of data measured for sample KOL2012 - 03 in reverse mode for temperature range from 12 K up to 200 K

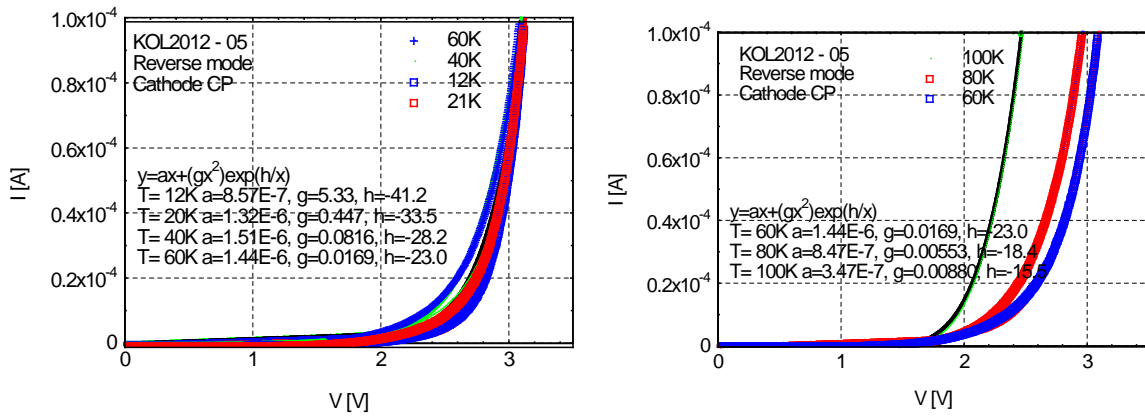


Fig. 6.28 Analytical method for the analysis of data measured for sample KOL2012 - 05 in reverse mode for temperature range from 12 K up to 100 K

Figures 6.29 and 6.30 show analytical method for the analysis of data measured for samples CTS2012 – 01 and CTS2012 – 04 for the reverse mode for temperature range from 12K up to 100 K.

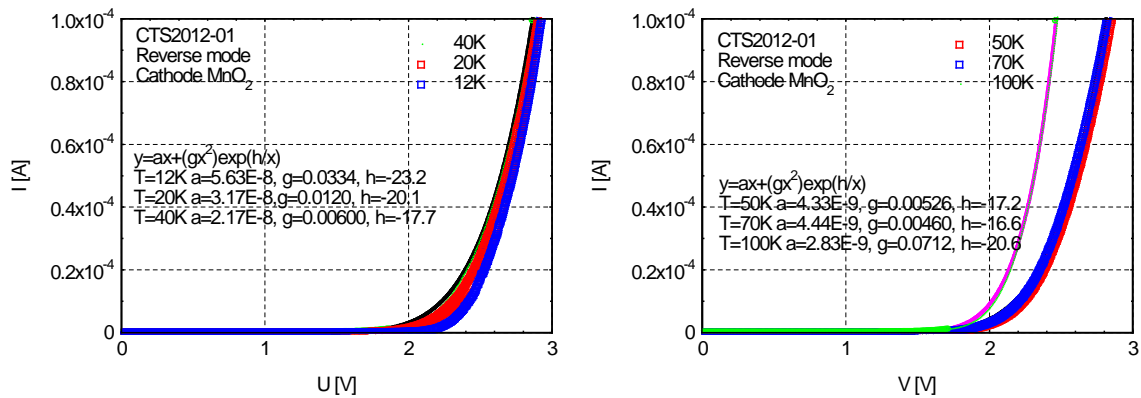


Fig. 6.29 Analytical method for the analysis of data measured for sample CTS2012 - 01 in reverse mode for temperature range from 12 K up to 100 K

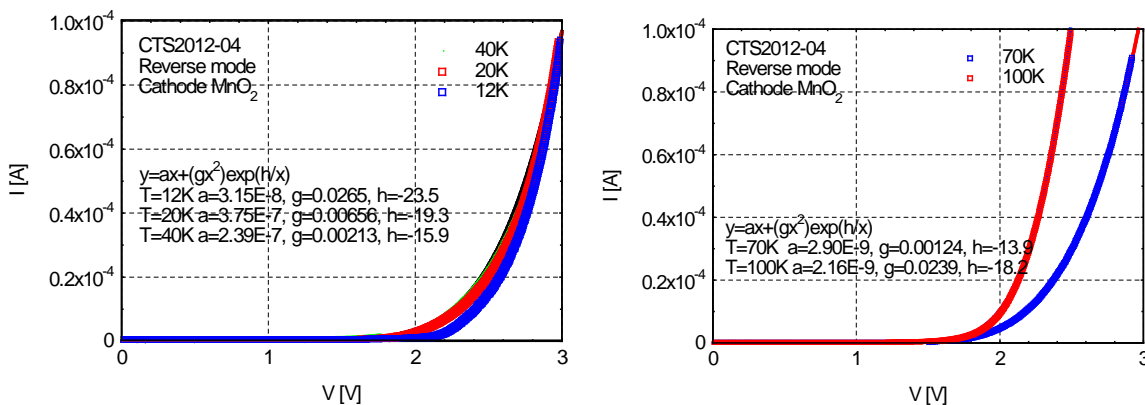


Fig. 6.30 Analytical method for the analysis of data measured for sample CTS2012 - 04 in reverse mode for temperature range from 12 K up to 100 K

Figures 6.31, 6.32 and 6.33 show analytical method for the analysis of data measured for samples MK2012 – 01, MK2012 – 02, and MK2012 – 03 for the reverse mode for temperature range from 12K up to 100 K.

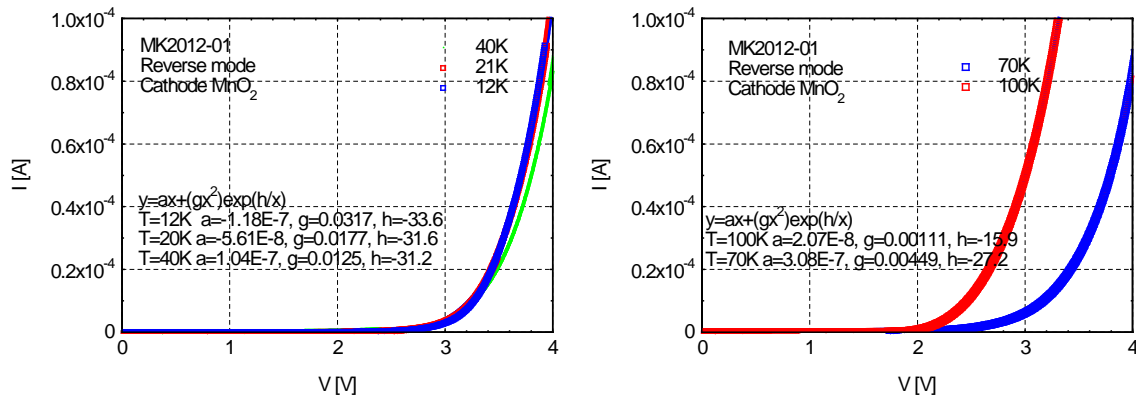


Fig. 6.31 Analytical method for the analysis of data measured for sample MK2012 - 01 in reverse mode for temperature range from 12 K up to 100 K

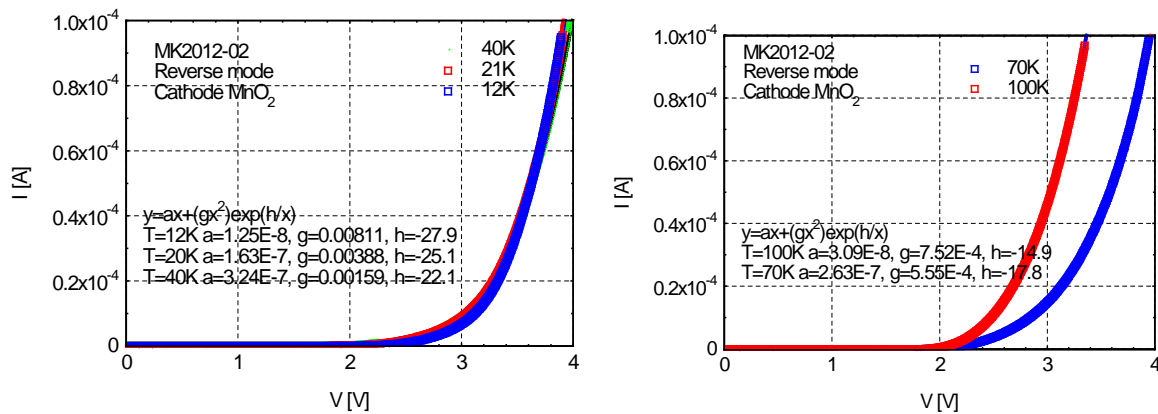


Fig. 6.32 Analytical method for the analysis of data measured for sample MK2012 - 02 in reverse mode for temperature range from 12 K up to 100 K

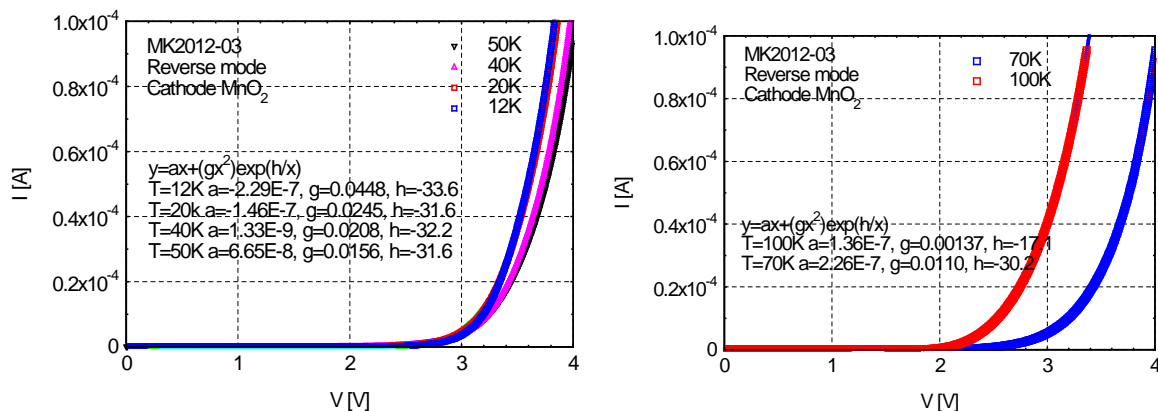


Fig. 6.33 Analytical method for the analysis of data measured for sample MK2012 - 03 in reverse mode for temperature range from 12 K up to 100 K

The parameters of tunneling current component in reverse mode obtained from the analytical method shown in Figs. 6.26 to 6.33 will be evaluated further in Chapter 6.2.4.2.

6.2.3. Tunneling from HOMO level of conducting polymer

I-V characteristics in normal mode measured for sample KOL2012 – 3 are shown in Fig. 6.12 and the details of the low voltage region of *I-V* characteristics are shown in Fig. 6.34. We can see that the characteristic is N-type with additional current component observed in the voltage range 0.5 V to 4 V. This current component depends on temperature – the highest value is observed for the temperature between 40 K and 60 K while about 10times lower value is observed at temperature 150 K. Figures 6.35 to 6.40 show the analysis of *I-V* curve with respect to the particular current components assessment. I consider here the Fowler-Nordheim tunneling component pronounced for the voltage above 3.5 V, and the second current component which I suppose is the tunneling from HOMO level in CP into the defect bands in the Ta₂O₅ layer. It is supposed that with increasing voltage in NM the HOMO level in CP coincide with the energy level of defect band in Ta₂O₅ layer. Then the direct tunneling appears in between these two energy levels. With additional voltage increase this tunneling component disappears.

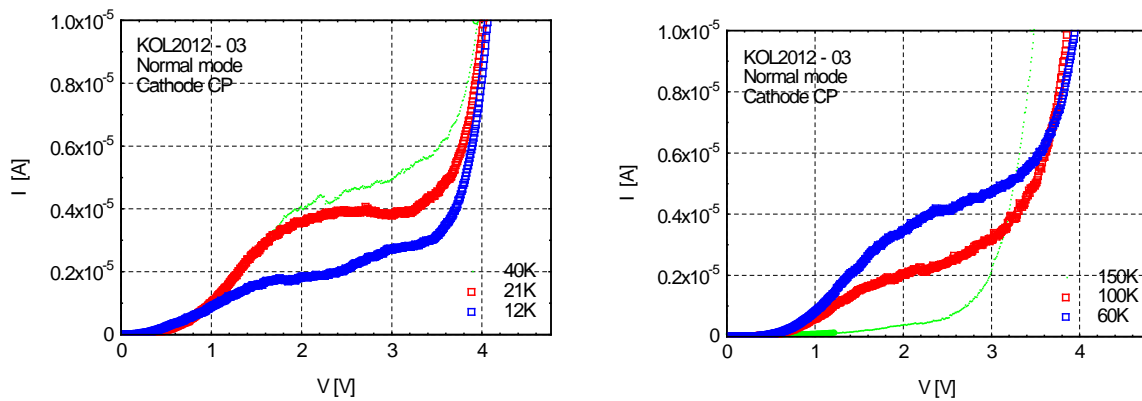


Fig. 6.34 *I-V* characteristic for sample KOL2012 – 03 sample in normal mode for temperature from 12 K up to 150 K in detailed view

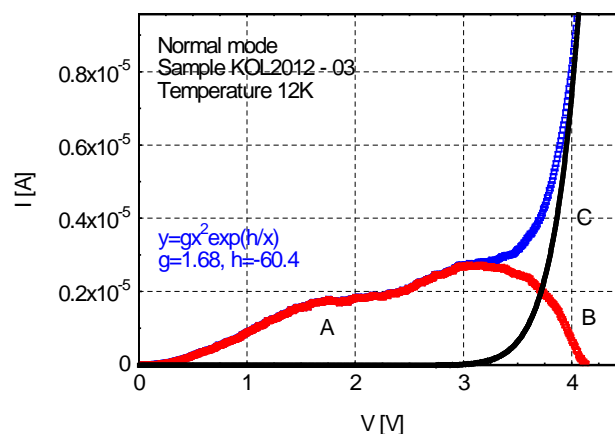


Fig. 6.35 *I-V* characteristic in normal mode analysis for sample KOL2012 - 03 for temperature 12 K. Blue curve – measured dependence (A), red curve – trap assisted tunneling from HOMO level (B), black curve – Fowler-Nordheim tunneling component (C)

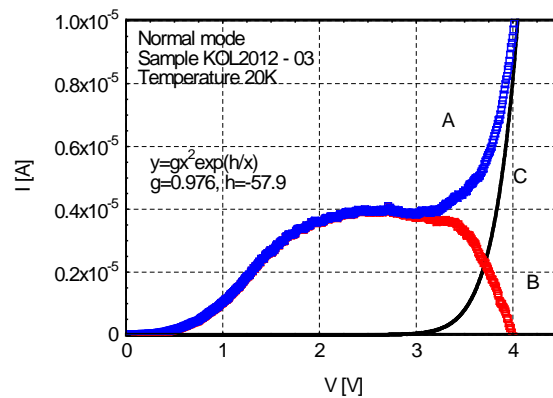


Fig. 6.36 *I-V* characteristic in normal mode analysis for sample KOL2012 - 03 for temperature 20 K. Blue curve – measured dependence (A), red curve – trap assisted tunneling from HOMO level (B), black curve – Fowler-Nordheim tunneling component (C)

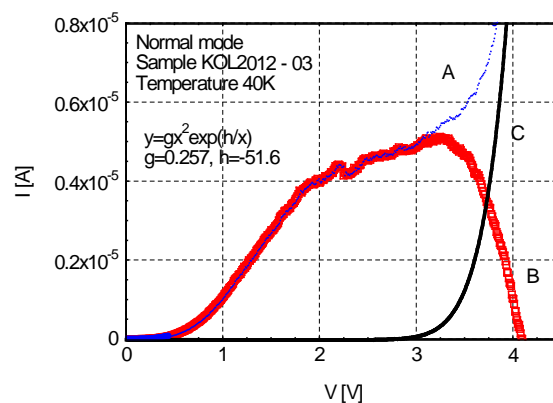


Fig. 6.37 *I-V* characteristic in normal mode analysis for sample KOL2012 - 03 for temperature 40 K. Blue curve – measured dependence (A), red curve – trap assisted tunneling from HOMO level (B), black curve – Fowler-Nordheim tunneling component (C)

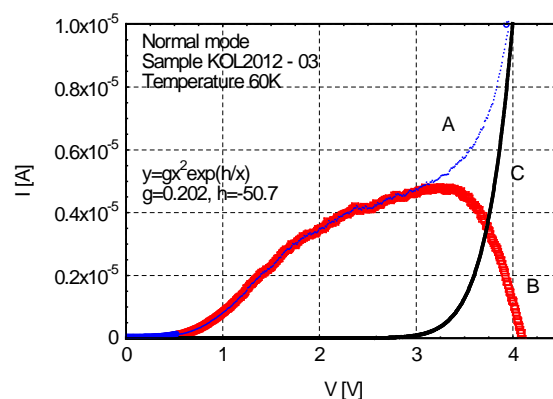


Fig. 6.38 *I-V* characteristic in normal mode analysis for sample KOL2012 - 03 for temperature 60 K. Blue curve – measured dependence (A), red curve – trap assisted tunneling from HOMO level (B), black curve – Fowler-Nordheim tunneling component (C)

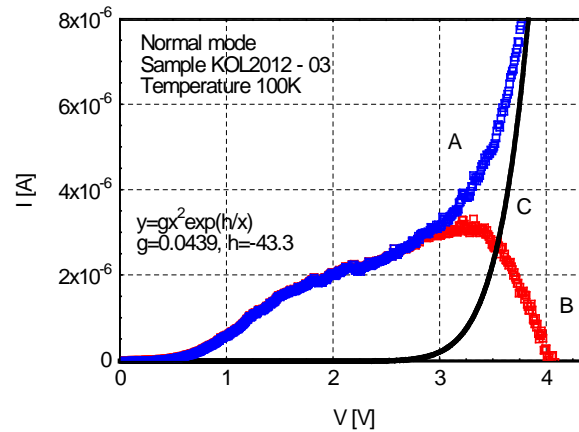


Fig. 6.39 *I-V* characteristic in normal mode analysis for sample KOL2012 - 03 for temperature 100 K. Blue curve – measured dependence (A), red curve – trap assisted tunneling from HOMO level (B), black curve – Fowler-Nordheim tunneling component (C)

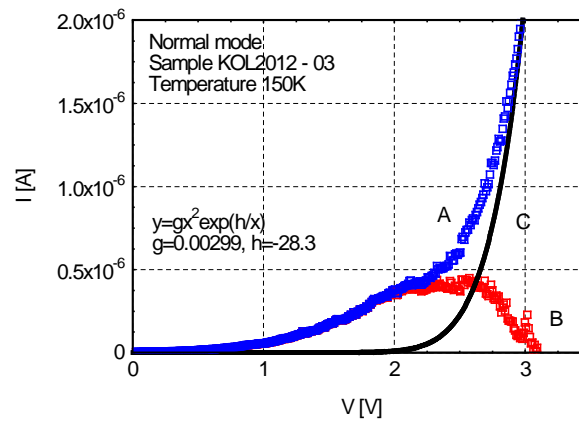


Fig. 6.40 *I-V* characteristic in normal mode analysis for sample KOL2012 - 03 for temperature 150 K. Blue curve – measured dependence (A), red curve – trap assisted tunneling from HOMO level (B), black curve – Fowler-Nordheim tunneling component (C)

In fact two maxima are observed on the curve characterizing the trap assisted tunneling current component – one for the bias voltage about 1.8 V and the second one for the bias voltage about 3.2 V. The presence of two maxima shows that at least two defect bands are present in the Ta₂O₅ structure.

6.2.4. Potential barrier estimation

Tunneling current component is dominant electron transport mechanism at very low temperature. In this case all temperature dependent processes are not involved in charge current transport. From the tunneling current component parameter U_T obtained by fitting experimental *I-V* curves the potential barrier height can be calculated. Results for the tantalum capacitors with both MnO₂ and CP cathode are shown in following chapter. From the *I-V* characteristics in normal mode I receive the values for estimation of potential barrier on the Ta₂O₅ – cathode interface while from the *I-V* characteristics in the reverse mode the value of

potential barrier on Ta – Ta₂O₅ interface is obtained. Tunneling current component is further characterized by the tunneling barrier transparency G_T which is determined directly from the I - V characteristic fit.

6.2.4.1. Potential barrier between Ta₂O₅ and cathode

The potential barrier energy is given as (calculated from equation 3.18):

$$ef_0 = \frac{\pi U_T 3eh}{6d8\rho\sqrt{2m^*}} \frac{\phi^2}{\phi} \quad (6.1)$$

Where U_T is the parameter obtained from fit of I - V characteristic, $e = 1.6 \times 10^{-19}$ C is elementary charge, $h = 6.626 \times 10^{-34}$ J is Planck constant, d is the dielectric thickness and $m^* = 0.1m_e = 9.1 \times 10^{-32}$ kg is considered value of electron effective mass.

Figures 6.41, 6.43 and 6.45 show the dependences of the tunneling barrier transparency on the temperatures for samples of series KOL2012, CTS2012 and MK2012, respectively. We can see that barrier transparency increases with decreasing temperature in the range 150 to 50 K and stabilizes in the low temperature range for samples KOL2012 with CP cathode. Different behavior is observed for samples with MnO₂ cathode. Here the tunneling barrier transparency exhibit maximum for the temperature about 50 K, while the value strongly decreases with decreasing temperature in the range 20 to 12 K.

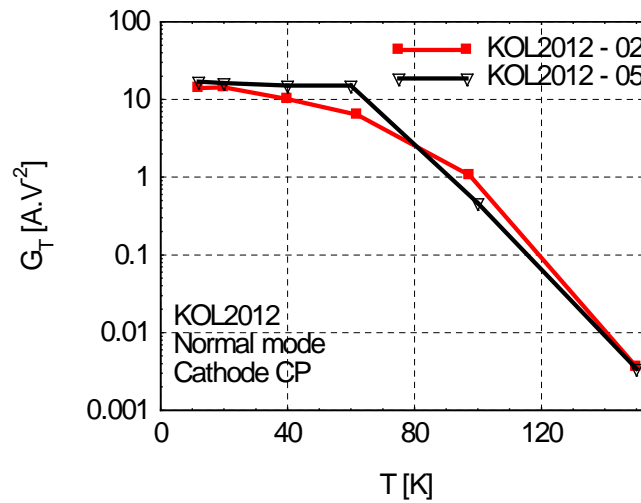


Fig. 6.41 Transparency of the barrier for electron tunneling vs. temperature for the series KOL2012 in normal mode in the temperature range from 12 K up to 150 K

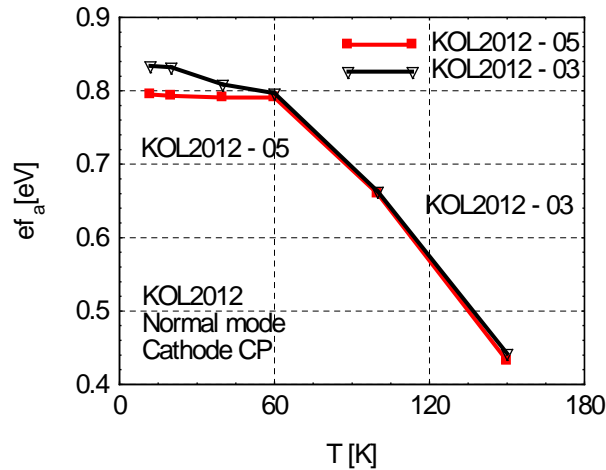


Fig. 6.42 Energy of the barrier for electron tunneling vs. temperature for the series KOL2012 in normal mode in the temperature range from 12 K up to 150 K

The dependences of calculated energy of the barrier for electron tunneling on temperature are shown in Figures 6.42, 6.44 and 6.46 for samples of series KOL2012, CTS2012 and MK2012, respectively. We can see that energy of the barrier for electron tunneling increases for about 0.3 eV with decreasing temperature in the range 150 to about 50 K. This increase can be induced by the shift of Fermi level with temperature – with decreasing temperature the Fermi level moves close to the defect band energy level, while at the room temperature it is placed approximately in the middle between the defect band and the conduction band in Ta₂O₅. The tunneling barrier energy value is constant for the temperatures below 50 K for samples with CP cathode while strongly decrease with temperature 20 and 12 K. The energy of the barrier for electron tunneling value decreasing is improbably in this temperature range – this tunneling barrier energy value decreasing can be caused by the change of value of electron effective mass. Considered value $0.1m_e$ is probably not valid in extra low temperature range for samples with MnO₂ cathode.

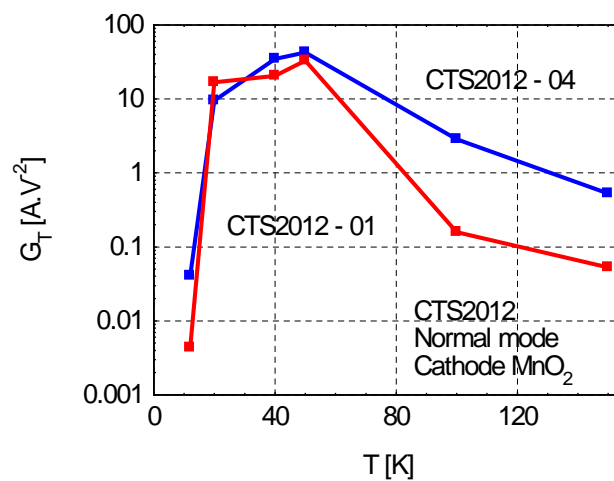


Fig. 6.43 Transparency of the barrier for electron tunneling vs. temperature for the series CTS2012 in normal mode in the temperature range from 12 K up to 150 K

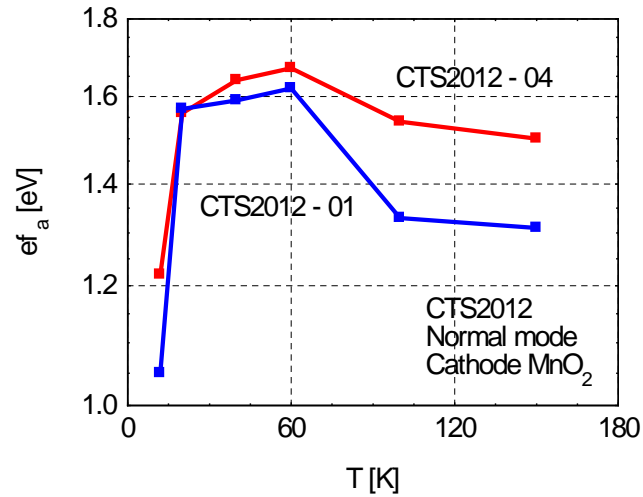


Fig. 6.44 Energy of the barrier for electron tunneling vs. temperature for the series CTS2012 in normal mode in the temperature range from 12 K up to 150K

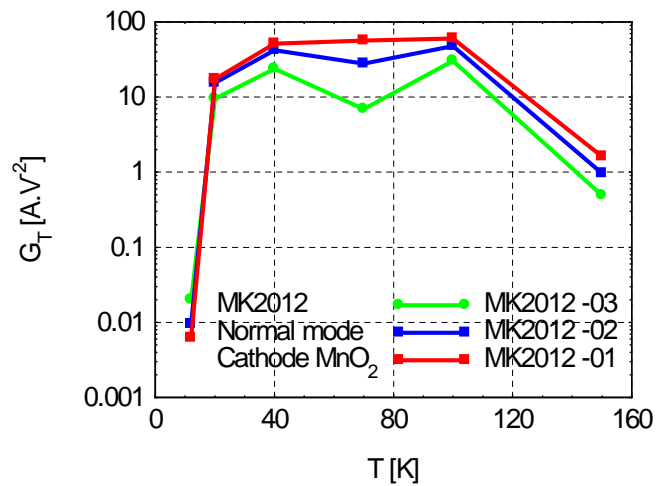


Fig. 6.45 Transparency of the barrier for electron tunneling vs. temperature for the series MK2012 in normal mode in the temperature range from 12 K up to 150 K

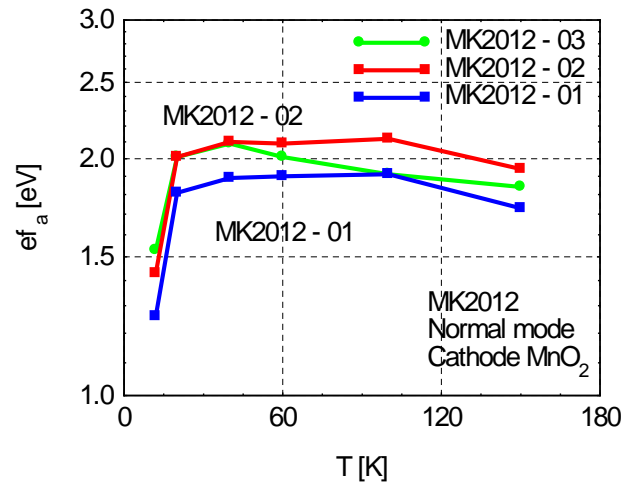


Fig. 6.46 Energy of the barrier for electron tunneling vs. temperature for the series MK2012 in normal mode in the temperature range from 12 K up to 150K

6.2.4.2. Potential barrier between anode and Ta₂O₅

Figures 6.47, 6.49 and 6.51 show the dependences of the transparency of the barrier for electron tunneling on the temperatures for samples of series KOL2012, CTS2012 and MK2012, respectively. We can see that transparency of the barrier for electron tunneling increases with decreasing temperature in the range 100 to 12 K for samples KOL2012 and MK2012. Different behavior is observed for samples with CTS2012. Here the transparency of the barrier for electron tunneling show high value for the temperature 100 K, then the value drops down and in the temperature range 70 K to 12 K it increases with decreasing temperature.

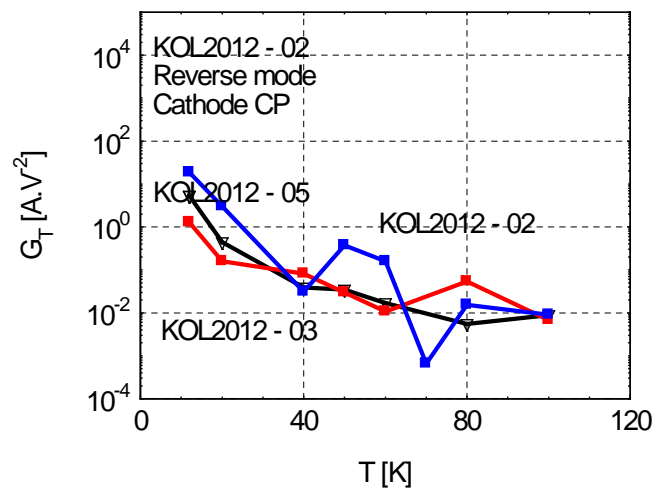


Fig. 6.47 Transparency of the barrier for electron tunneling vs. temperature for the series KOL2012 in reverse mode in the temperature range from 12 K up to 100 K

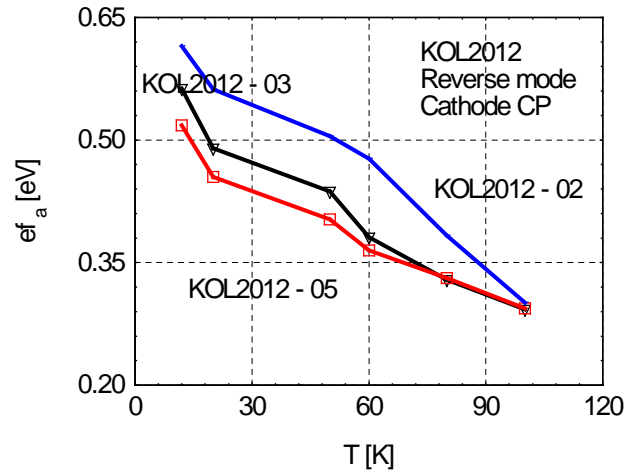


Fig. 6.48 Energy of the barrier for electron tunneling vs. temperature for the series KOL2012 in reverse mode in the temperature range from 12 K up to 100 K

The dependences of calculated energy of the barrier for electron tunneling on temperature are shown in Figures 6.48, 6.50 and 6.52 for samples of series KOL2012, CTS2012 and MK2012, respectively. We can see that the energy of the barrier for electron tunneling increases for about 0.3 eV with decreasing temperature in the range 100 to 12 K for samples of series KOL2012 and MK2012. The energy of the barrier for electron tunneling increases for about 0.1 eV with decreasing temperature in the range 70 to 12 K for samples of series CTS2012. This increase can be induced by the shift of Fermi level with temperature.

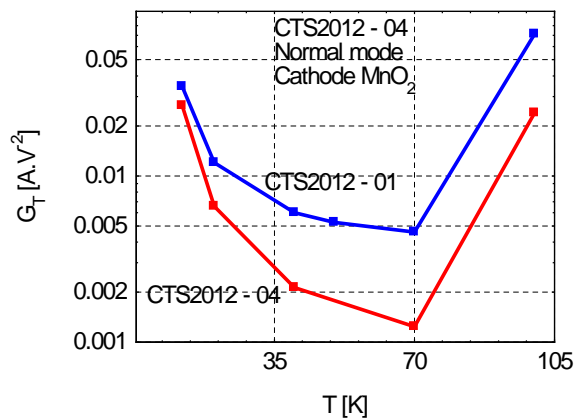


Fig. 6.49 Transparency of the barrier for electron tunneling vs. temperature for the series CTS2012 in reverse mode in the temperature range from 12 K up to 100 K

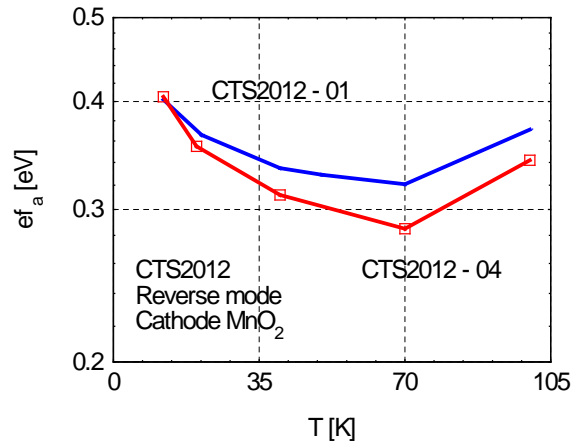


Fig. 6.50 Energy of the barrier for electron tunneling vs. temperature for the series CTS2012 in reverse mode in the temperature range from 12 K up to 100 K

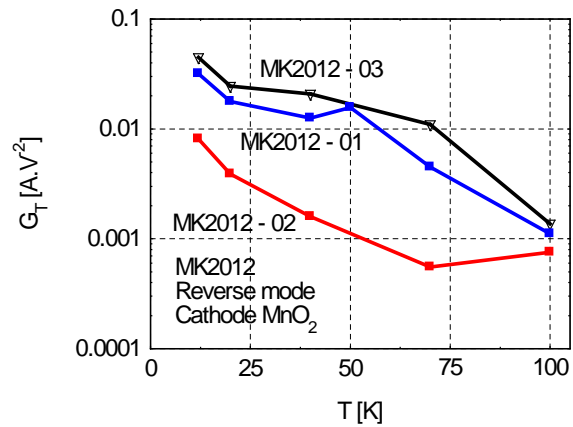


Fig. 6.51 Transparency of the barrier for electron tunneling vs. temperature for the series MK2012 in reverse mode in the temperature range from 12 K up to 100 K

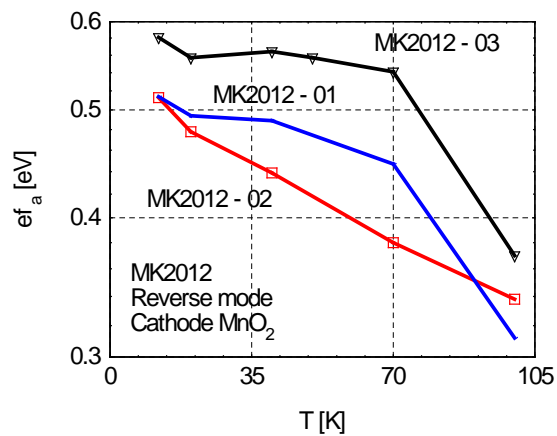


Fig. 6.52 Energy of tunneling barrier vs. temperature for the series MK2012 in reverse mode in the temperature range from 12 K up to 100 K

6.2.5. Graphical method for the ohmic current component analysis

Graphical analysis of ohmic current component was performed for samples of all series. Figures 6.53, 6.55, and 6.57 show the dependences of current density on the electric field for the sample KOL2012 – 05, sample CTS2012 - 01 and sample MK2012 – 01, respectively, for different temperatures. We can see that the conductance of all evaluated samples increases with temperature and it varies in the range 10^{-15} to 10^{-14} Sm⁻¹. These dependences in logarithmic scale are shown in Figs. 6.54, 6.56, and 6.58. From the dependences in logarithmic scale the electric field range, where the ohmic component is dominant, can be determined. This component is dominant up to the electric field 0.05 MV.cm⁻¹ for sample of series KOL2012, and up to the electric field 0.8 MV.cm⁻¹ for samples of series CTS2012 and MK2012.

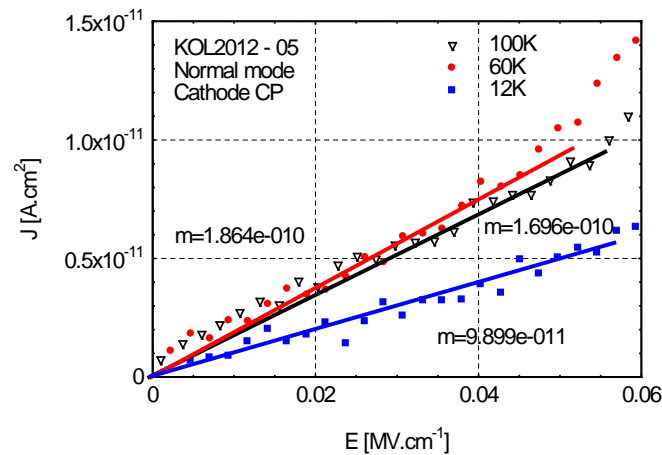


Fig. 6.53 Current density J vs. electric field E characteristic for sample KOL2012 - 05 for temperature 12 K, 60 K and 100 K for the normal mode

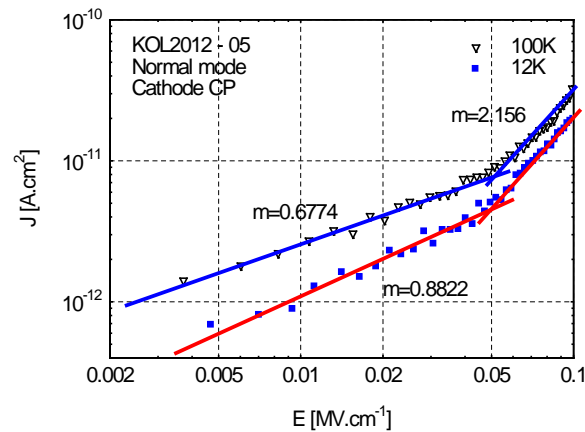


Fig. 6.54 Current density J vs. electric field E characteristic in logarithmic scale for sample KOL2012 - 05 for temperature 12 K and 80 K for the normal mode

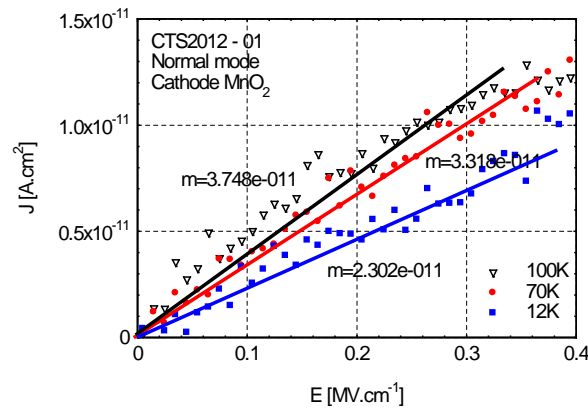


Fig. 6.55 Current density J vs. electric field E characteristic for sample CTS2012 - 01 for temperature 12 K, 70 K and 100 K for the normal mode

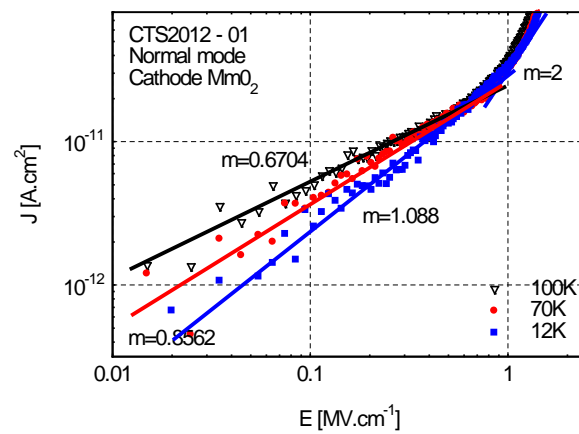


Fig. 6.56 Current density J vs. electric field E characteristic in logarithmic scale for sample CTS2012-01 for temperature 12 K, 70 K and 100 K for the normal mode

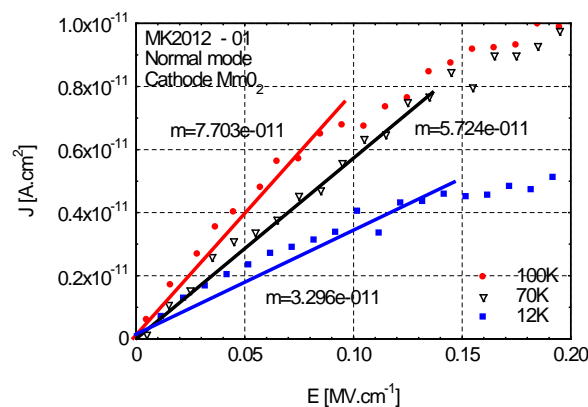


Fig. 6.57 Current density J vs. electric field E characteristic for sample MK2012 - 01 for temperature 12 K, 70 K and 100 K for the normal mode

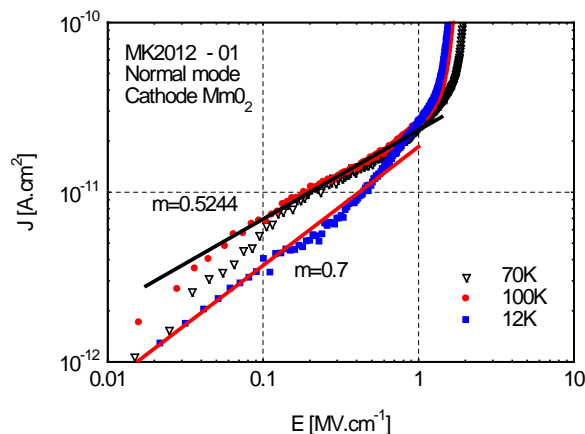


Fig. 6.58 Current density J vs. electric field E characteristic in logarithmic scale for sample MK2012 - 01 for temperature 12 K, 70 K and 100 K for the normal mode

6.2.6. Graphical method for the PF current component analysis

The evaluation of experimentally obtained data by Poole-Frenkel plot is shown in Fig. 3.15 for sample KOL2012-05 for temperature 150 K. PF current component is observed in the range 0.1 to 0.6 MVcm⁻¹. Here the slope of linear approximation is determined as 4.42 MV^{-0.5}cm^{0.5} and from this the Poole-Frenkel coefficient value is calculated as $\beta_{PF} = 4.78$ V^{-0.5}. That is close to the theoretical value $\beta_{PF} = 5.50$ V^{-0.5} for temperature 150 K. Theoretical values of Poole-Frenkel coefficient for different temperatures, theoretical values of the slope of linear approximation in PF plot $m_{PF(\text{theory})}$ and experimentally obtained values the slope of linear approximation $m_{PF(\text{measured})}$ are shown in Table 4. We can see that only the experimental value for 150 K is comparable with the theoretical one. For lower temperature this current component is negligible.

Tab. 4. Theoretical values of Poole-Frenkel coefficient for different temperatures, theoretical values of the slope of linear approximation in PF plot $m_{PF(\text{theory})}$ and experimentally obtained values the slope of linear approximation $m_{PF(\text{measured})}$ in normal mode for sample KOL2012 - 05

T [K]	12	20	30	40	60	80	100	150
$m_{PF(\text{measured})}$ [MV ^{-0.5} cm ^{0.5}]	2.44	1.96	2.14	2.06	1.65	1.58	2.42	4.42
$m_{PF(\text{theory})}$ [MV ^{-0.5} cm ^{0.5}]	61.26	36.76	24.51	18.39	12.25	9.19	7.35	4.90
$b_{PF(\text{theory})}$ [V ^{-0.5}]	68.85	41.31	27.54	20.65	13.80	10.33	8.26	5.51

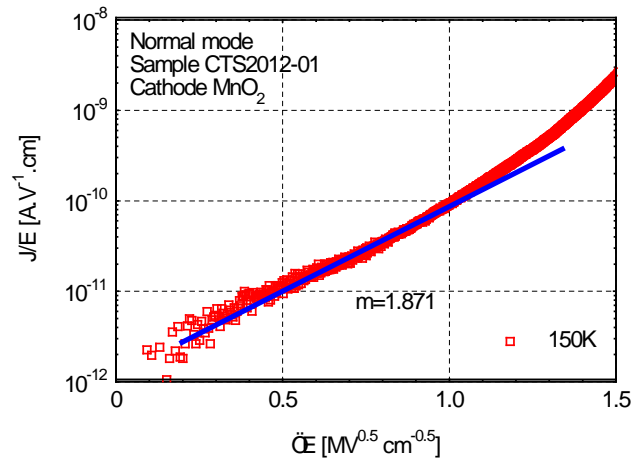


Fig. 6.59 Poole-Frenkel plot for the sample CTS2012 - 01 for the temperature 150 K

Figures 6.59, 6.60 and 6.61 show the PF plot for samples CTS2012-01 and CTS2012-04 for temperature 150 K and for sample MK2012-01 for temperatures 100 K, 150 K and 250 K. For all these samples the determined values the slope of linear approximation $m_{PF(\text{measured})}$ are very low comparing to the expected theoretical value. For the temperature 250 K the value $m_{PF(\text{theory})} = 2.94 \text{ MV}^{-0.5}\text{cm}^{0.5}$ which is about three times the value determined from the experimental data. The PF current component is negligible even at temperature 150 K for series CTS2012 and at temperature 250 K for series MK2012.

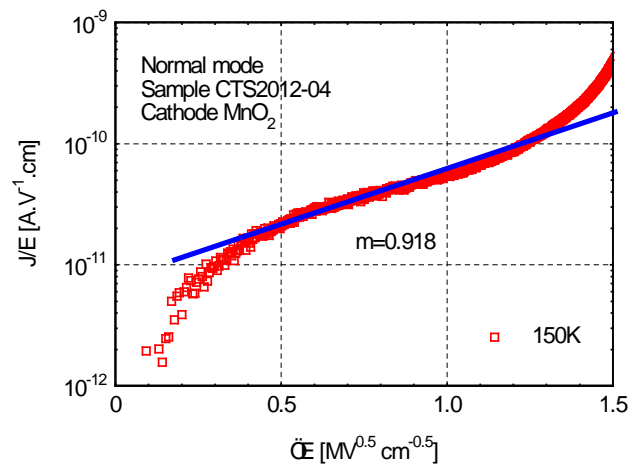


Fig. 6.60 Poole-Frenkel plot for the sample CTS2012 - 04 for the temperature 150 K

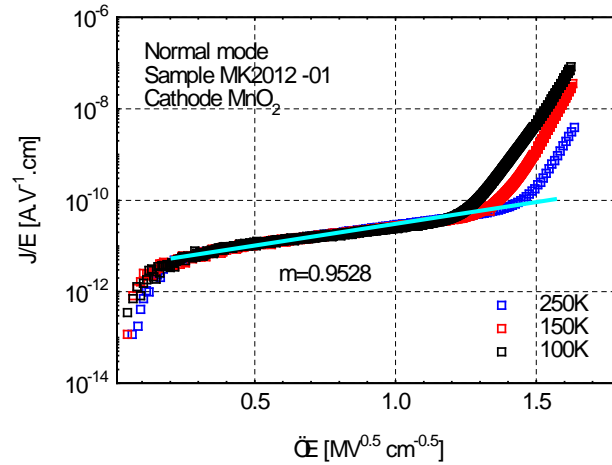


Fig. 6.61 Poole-Frenkel plot for the sample MK2012 - 01 for the temperatures 100 K, 150 K and 250 K

6.2.7. Graphical method for the Schottky current component

The Schottky current component can be determined from the Schottky plot – i.e. from the linear part of $\log J$ vs. \sqrt{E} characteristic.

As mentioned before in Chapter 3, from equations 3.11 and 3.15 we can derive the relation between Poole-Frenkel and Schottky constants $b_{PF} = 2b_S$. These constants characterize the barrier lowering due to the Poole-Frenkel or Schottky effect, respectively. Then also the value of slope of linear approximation in Schottky plot is connected with the slope of PF plot as: $m_{PF(\text{theory})} = 2m_{S(\text{theory})}$.

Schottky current component could be observed in the range 0.1 to 0.6 MVcm⁻¹. The expected slope of linear approximation is calculated as $m_{S(\text{theory})}(T=150\text{ K}) = 2.45\text{ MV}^{-0.5}\text{cm}^{0.5}$ for temperature 150 K and $m_{S(\text{theory})}(T=100\text{ K}) = 3.68\text{ MV}^{-0.5}\text{cm}^{0.5}$ for temperature 100 K. Figures 6.62 to 6.65 show the Schottky plot for samples KOL2012-05, CTS2012-01, CTS2012-04 and MK2012-01 for temperature 150 K for all the samples and temperature 100 K for MK2012-01. The slope of linear approximation determined for sample KOL2012-05 is about twice higher comparing to the theoretical value (see Fig. 6.62). This indicates that Poole-Frenkel current is pronounced in this sample while the Schottky current contribution is negligible. The slope of Schottky plot for samples CTS2012-01, CTS2012-04 and MK2012-01 is shown in Figs. 6.63 to 6.65. For all these samples the determined values of the slope of linear approximation $m_{S(\text{measured})}$ are very low comparing to the expected theoretical value. Schottky current contribution is negligible even for temperature 150 K.

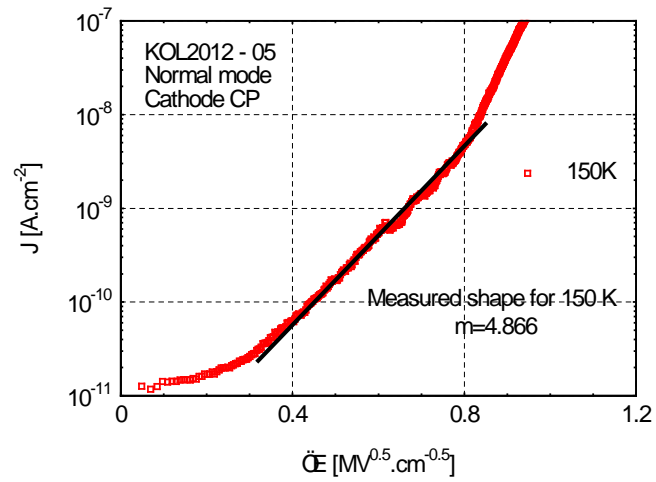


Fig. 6.62 Schottky plot for the sample KOL2012 – 05 for temperature 150 K

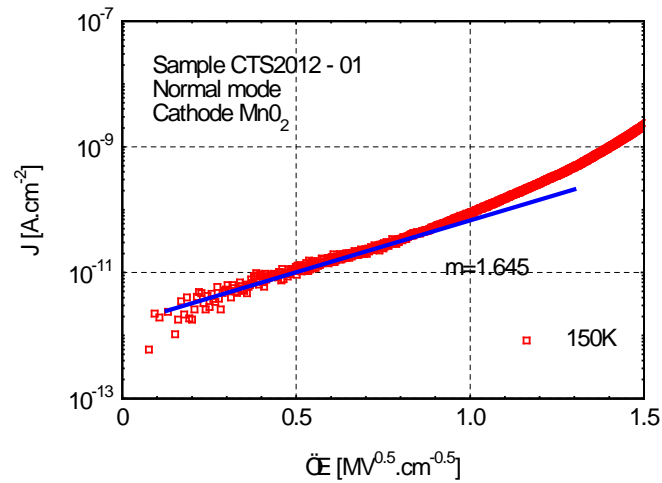


Fig. 6.63 Schottky plot for the sample CTS2012 - 01 for temperature 150 K

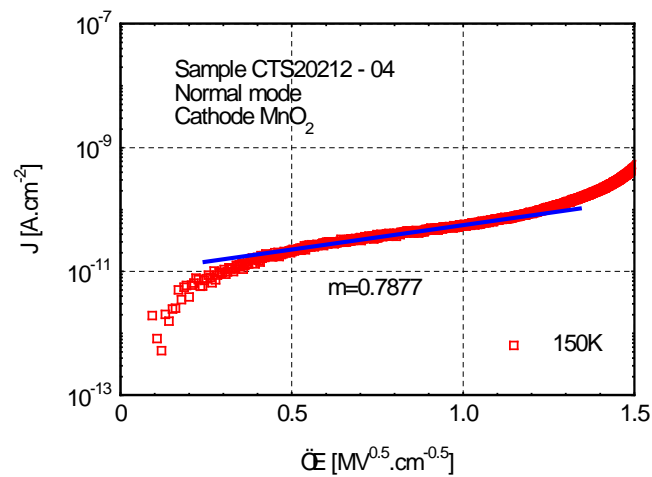


Fig. 6.64 Schottky plot for the sample CTS2012 - 04 for temperature 150 K

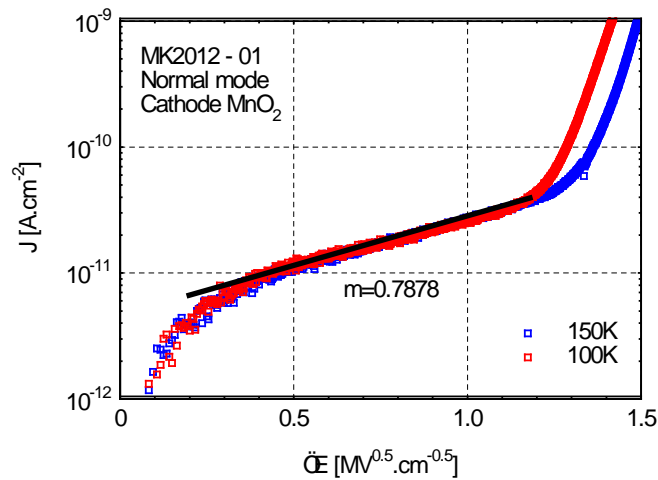


Fig. 6.65 Schottky plot for the sample MK2012 - 01 for temperatures 150 K and 100 K

Schottky current component is not pronounced in studied structures in all evaluated temperature range.

6.2.8. Graphical method for the Fowler-Nordheim tunneling for normal mode

The tunneling current component is possible to determine by graphical method with Fowler-Nordheim graph. The slope of linear approximation of measured data for high electric field range is determined from Fowler Nordheim graph. From the slope m the value of tunneling parameter E_T could be calculated according to Eq. 3.23.

Figures 6.66 to 6.68 show the Fowler-Nordheim graph in normal mode for 3 samples of KOL2012 series for the temperatures 12 K, 60 K and 100 K, respectively. Linear approximation is performed for the measured data for the electric field above 0.9 MVcm⁻¹. Absolute value of the slope of linear approximation decreases with increasing temperature and varies in the range 8.152 MVcm⁻¹ to 5.569 MVcm⁻¹.

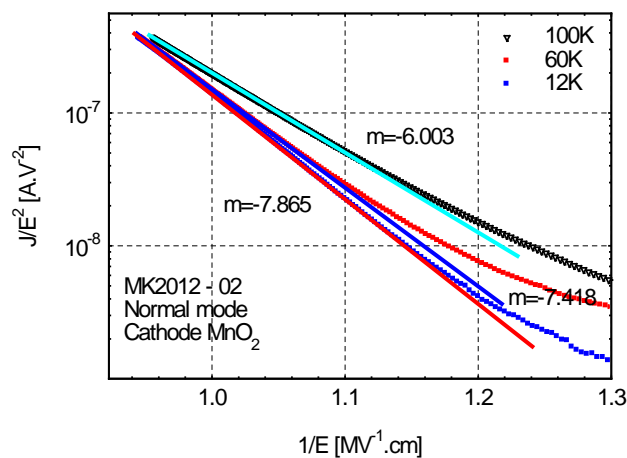


Fig. 6.66 Fowler-Nordheim plot in normal mode for the sample KOL2012 - 02 for the temperatures 12 K, 60 K and 100 K

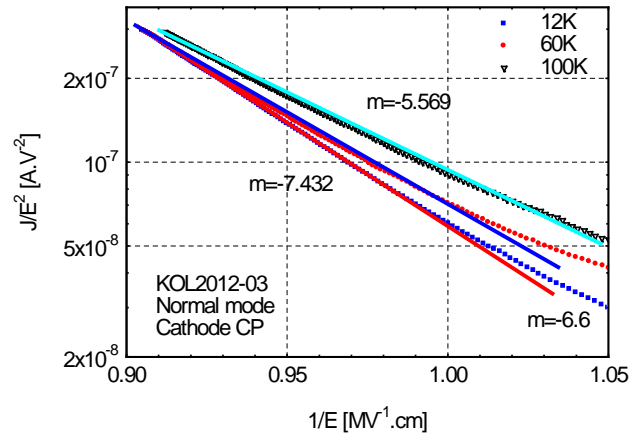


Fig. 6.67 Fowler-Nordheim plot in normal mode for the sample KOL2012 – 03 for the temperatures 12 K, 60 K and 100 K

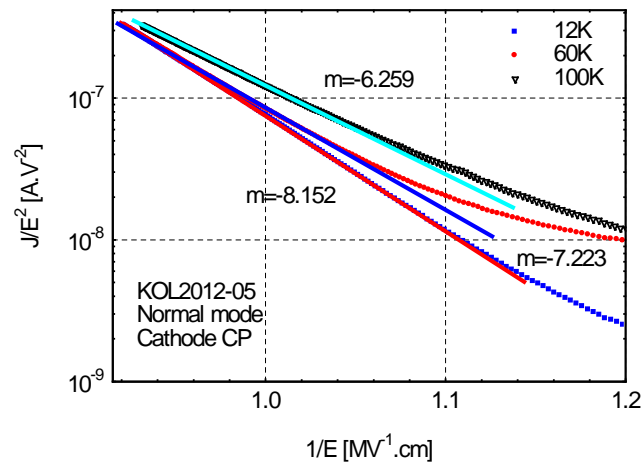


Fig. 6.68 Fowler-Nordheim plot in normal mode for the sample KOL2012 – 05 for the temperatures 12 K, 60 K and 100 K

Figures 6.69 and 6.70 show the Fowler-Nordheim graph in normal mode for 2 samples of CTS2012 series for the temperatures 12 K, 70 K and 100 K, respectively. Linear approximation is performed for the measured data for the electric field above 2.5 MVcm⁻¹. Absolute value of the slope of linear approximation varies in the range 23.93 MVcm⁻¹ to 15.07 MVcm⁻¹ and the maximum value is determined for 70 K for both samples.

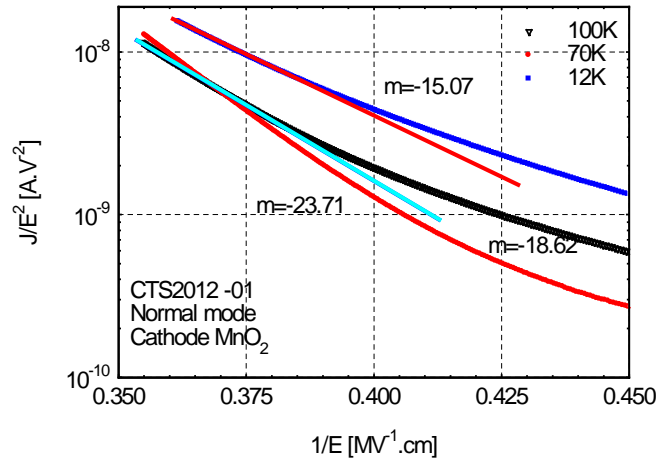


Fig. 6.69 Fowler-Nordheim plot in normal mode for the sample CTS2012 - 01 for the temperatures 12 K, 70 K and 100 K

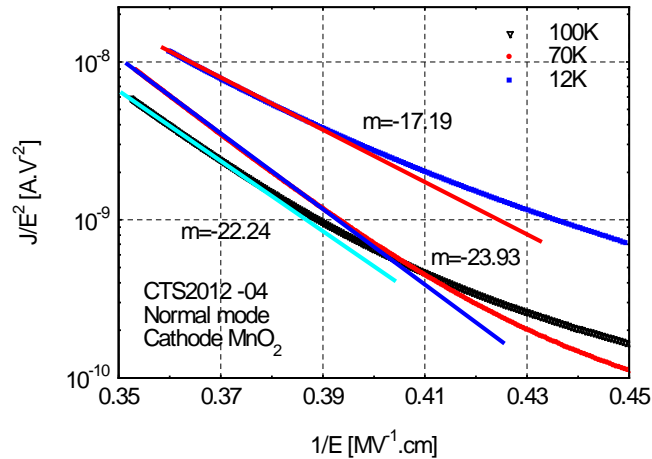


Fig. 6.70 Fowler-Nordheim plot in normal mode for the sample CTS2012 - 04 for the temperatures 12 K, 70 K and 100 K

Figures 6.71 to 6.73 show the Fowler-Nordheim graph in normal mode for 3 samples of MK2012 series for the temperatures 12 K, 70 K and 100 K, respectively. Linear approximation is performed for the measured data for the electric field above 2.1 MVcm⁻¹. Absolute value of the slope of linear approximation varies in the range 22.61 MVcm⁻¹ to 13.39 MVcm⁻¹ and the maximum value is determined for 70 K for all evaluated samples.

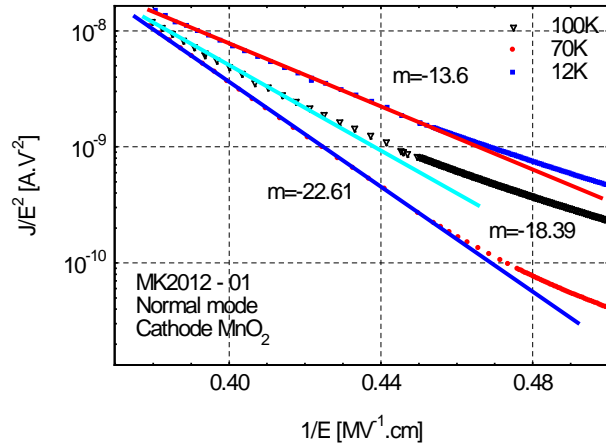


Fig. 6.71 Fowler-Nordheim plot in normal mode for the sample MK2012-01 for the temperatures 12 K, 70 K and 100 K

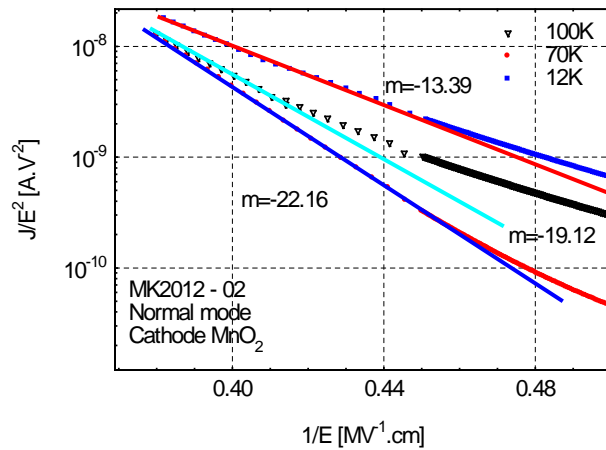


Fig. 6.72 Fowler-Nordheim plot in normal mode for the sample MK2012-02 for the temperatures 12 K, 70 K and 100 K

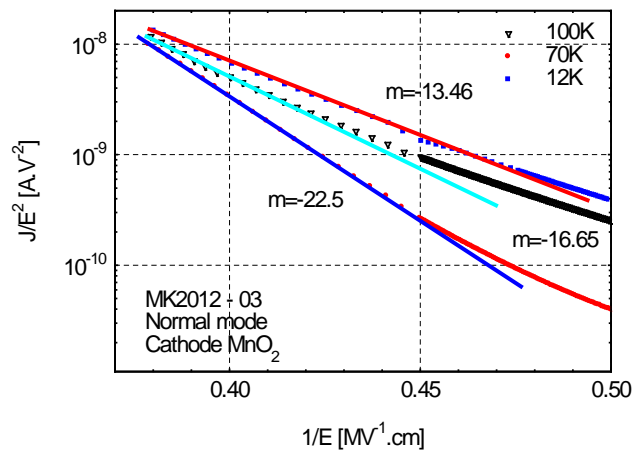


Fig. 6.73 Fowler-Nordheim plot in normal mode for the sample MK2012-03 for the temperatures 12 K, 70 K and 100 K

The results for electron tunneling current component in normal mode evaluation are discussed further in chapter 7.

6.2.9. Graphical method for the Fowler-Nordheim tunneling for reverse mode

Figures 6.74 to 6.76 show the Fowler-Nordheim graph in reverse mode for 3 samples of KOL2012 series for the temperatures 12 K, 60 K and 80 K, respectively. Linear approximation is performed for the measured data for the electric field above 0.65 MVcm⁻¹. Absolute value of the slope of linear approximation decreases with increasing temperature and varies in the range 4.798 MVcm⁻¹ to 2.068 MVcm⁻¹.

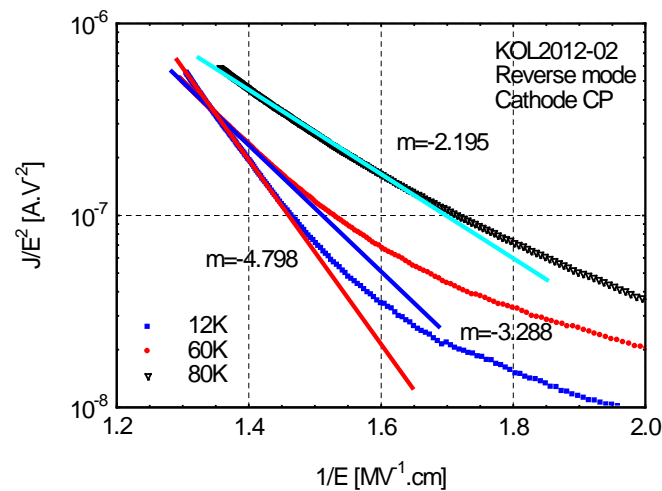


Fig. 6.74 Fowler-Nordheim plot in reverse mode for the sample KOL2012 – 02 for the temperatures 12 K, 60 K and 80 K

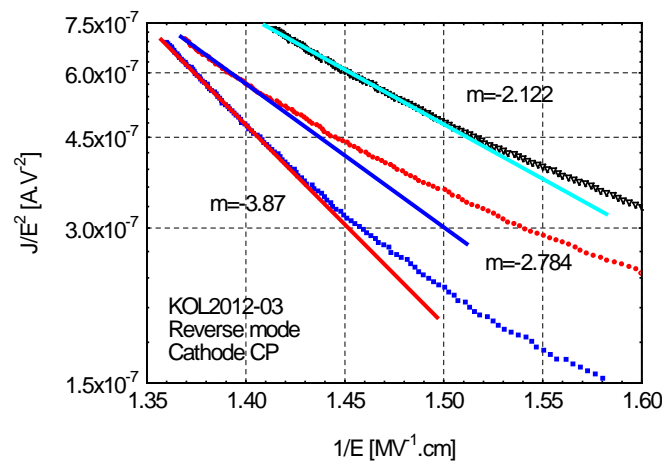


Fig. 6.75 Fowler-Nordheim plot in reverse mode for the sample KOL2012 – 03 for the temperatures 12 K, 60 K and 80 K

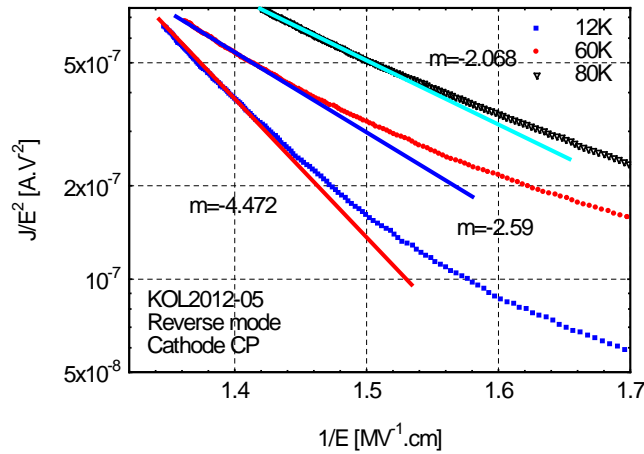


Fig. 6.76 Fowler-Nordheim plot in reverse mode for the sample KOL2012 – 05 for the temperatures 12 K, 60 K and 80 K

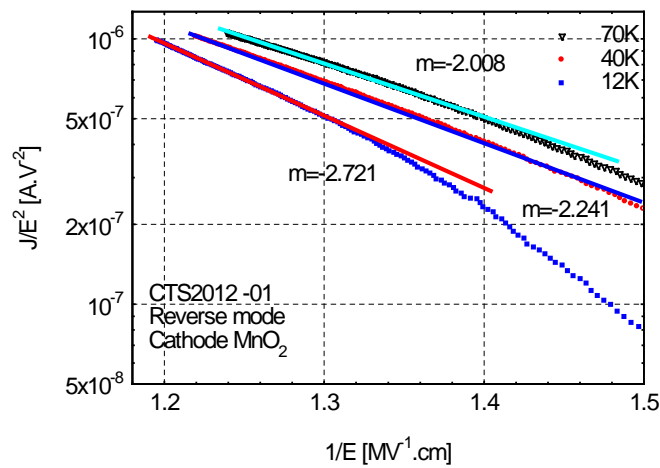


Fig. 6.77 Fowler-Nordheim plot in reverse mode for the sample CTS2012-01 for the temperatures 12 K, 40 K and 70 K

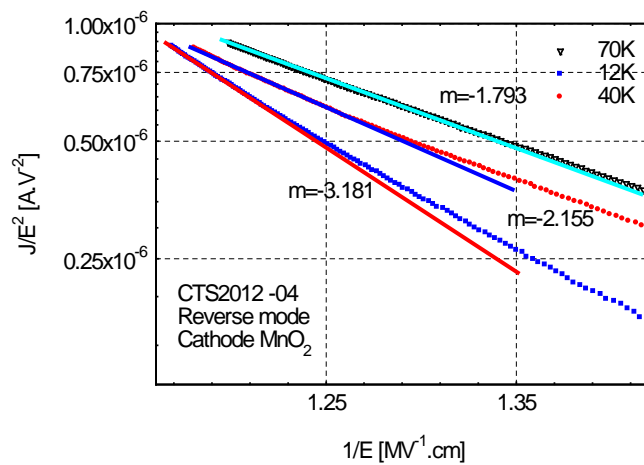


Fig. 6.78 Fowler-Nordheim plot in reverse mode for the sample CTS2012-04 for the temperatures 12 K, 40 K and 70 K

Figures 6.77 and 6.78 show the Fowler-Nordheim graph in reverse mode for 2 samples of CTS2012 series for the temperatures 12 K, 40 K and 70 K, respectively. Linear approximation is performed for the measured data for the electric field above 0.75 MVcm⁻¹. Absolute value of the slope of linear approximation decreases with increasing temperature and varies in the range 3.18 MVcm⁻¹ to 1.793 MVcm⁻¹.

Figures 6.79 to 6.81 show the Fowler-Nordheim graph in reverse mode for 3 samples of MK2012 series for the temperatures 12 K, 50 K and 70 K, respectively. Linear approximation is performed for the measured data for the electric field above 0.75 MVcm⁻¹. Absolute value of the slope of linear approximation decreases with increasing temperature and varies in the range 3.167 MVcm⁻¹ to 1.948 MVcm⁻¹.

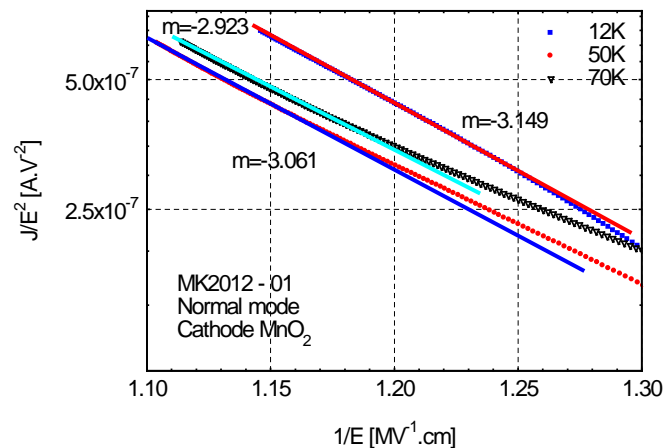


Fig. 6.79 Fowler-Nordheim plot in reverse mode for the sample MK2012-01 for the temperatures 12 K, 50 K and 70 K

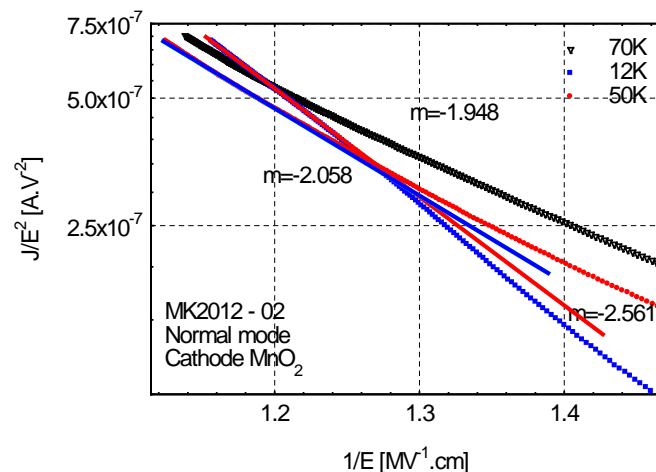


Fig. 6.80 Fowler-Nordheim plot in reverse mode for the sample MK2012-02 for the temperatures 12 K, 50 K and 70 K

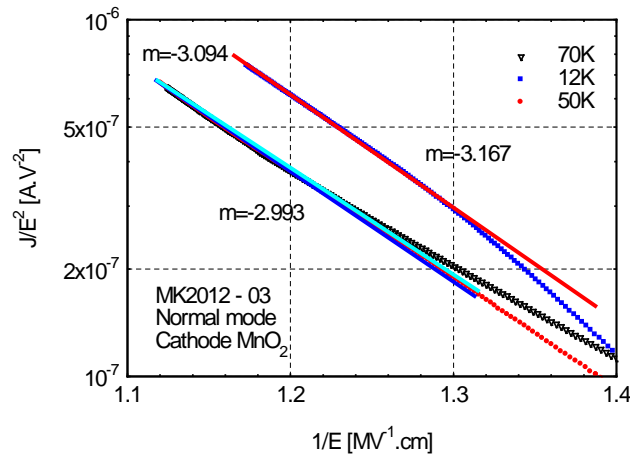


Fig. 6.81 Fowler-Nordheim plot in reverse mode for the sample MK2012-03 for the temperatures 12 K, 50 K and 70 K

The results for electron tunneling current component in reverse mode evaluation are discussed further in chapter 7.

6.2.10. Thermionic emission limited current over the Schottky barrier

Thermionic emission current component increases exponentially with the applied voltage. Then the in the semi-logarithmic scale the thermionic emission current component is shown as the straight line. From the linear approximation of measured data we can determine the value of thermionic emission current constant I_0 from the intersection of approximation line with y-axis and from the slope of line m the value of thermionic emission parameter β_{TE} can be calculated according to Eq. 3.27. Figure 6.82 shows the evaluation of $I-V$ characteristic for sample KOL2012-02 for the temperatures 100 K, 150 K and 200 K, respectively. Determined values of thermionic emission current constant I_0 vs. temperature and inverse temperature $1000/T$, respectively are shown in Fig. 6.83. From the value of I_0 the Schottky barrier energy $e\Phi_s$ can be calculated from Eq. 3.25.

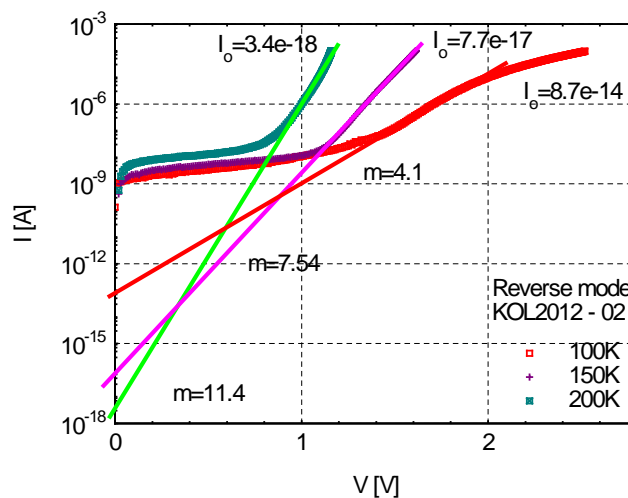


Fig. 6.82 $I-V$ characteristic in reverse mode in semi-logarithmic scale with linear approximation for the thermionic emission current component analysis for sample KOL2012 - 02 for temperatures 100 K, 150 K and 200 K

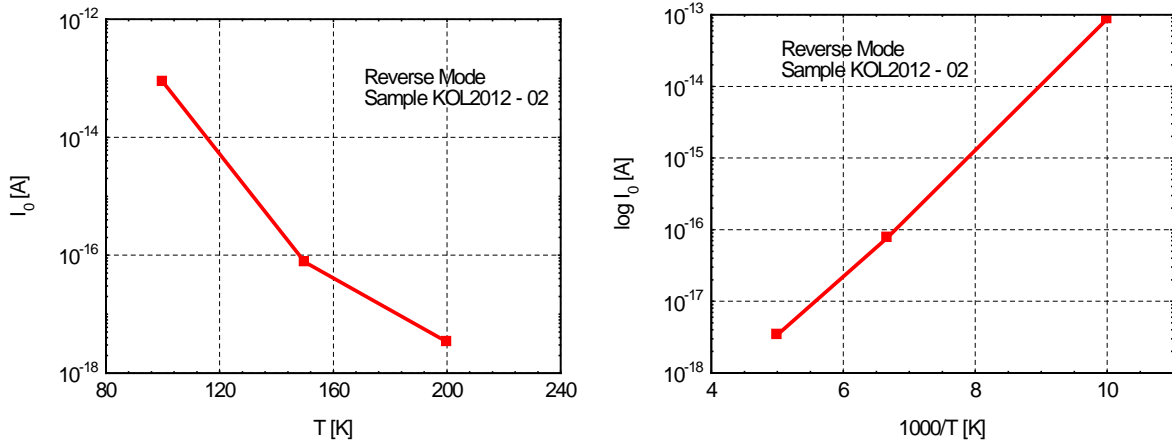


Fig. 6.83 Thermionic emission current constant I_0 vs. temperature (left) and thermionic emission current constant vs. $1000/T$ (right) for sample **KOL2012 - 02**

Values of the slope m of linear approximation, calculated values of β_{TE} (from Eq. 3.27) and the ideality factor for thermionic emission current determined from β_{TE} (from Eq. 3.26) for sample KOL2012-02 for temperatures 100 K, 150 K and 200 K are shown in Tab. 5.

Tab. 5. Values of m , β_{TE} and ideality factor n calculated for sample KOL2012 - 02 for temperatures 100 K, 150 K and 200 K

Temperature [K]	m [V ⁻¹]	β_{TE} [V ⁻¹]	n [-]
200	11.4	26.24	2.21
150	7.54	17.36	4.45
100	4.1	9.44	12.2

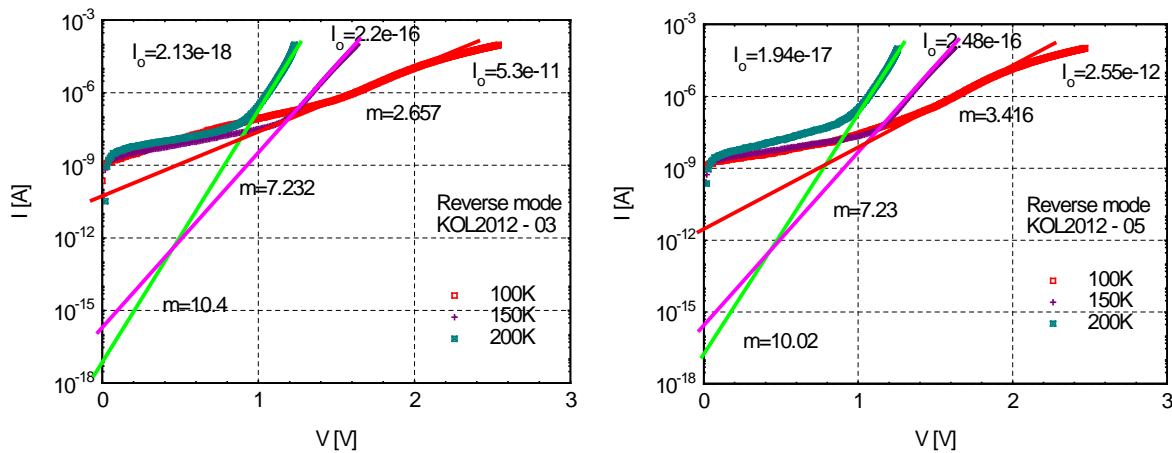


Fig. 6.84 I - V characteristic in reverse mode in semi-logarithmic scale with linear approximation for the thermionic emission current component analysis for samples KOL2012-03 and 05 for temperatures 100 K, 150 K and 200 K

Figure 6.84 shows the evaluation of I - V characteristic for samples KOL2012-03 (left) and KOL2012-05 (right) for the temperatures 100 K, 150 K and 200 K, respectively. Values of the slope m of linear approximation, calculated values of β_{TE} and the ideality factor for thermionic emission current determined from β_{TE} for samples KOL2012-03 and KOL2012-05 for temperatures 100 K, 150 K and 200 K are shown in Tabs. 6 and 7.

Tab. 6. Values of m , β_{TE} and ideality factor n calculated for sample KOL2012 – 03 for temperatures 100 K, 150 K and 200 K

Temperature [K]	m [V ⁻¹]	β_{TE} [V ⁻¹]	n [-]
200	10.4	23.93	2.42
150	7.232	16.64	4.65
100	2.657	6.11	18.98

Tab. 7. Values of m , β_{TE} and ideality factor n calculated for sample KOL2012 – 05 for temperatures 100 K, 150 K and 200 K

Temperature [K]	m [V ⁻¹]	β_{TE} [V ⁻¹]	n [-]
200	10.02	23.05	2.51
150	7.23	16.64	4.65
100	3.416	7.86	14.75

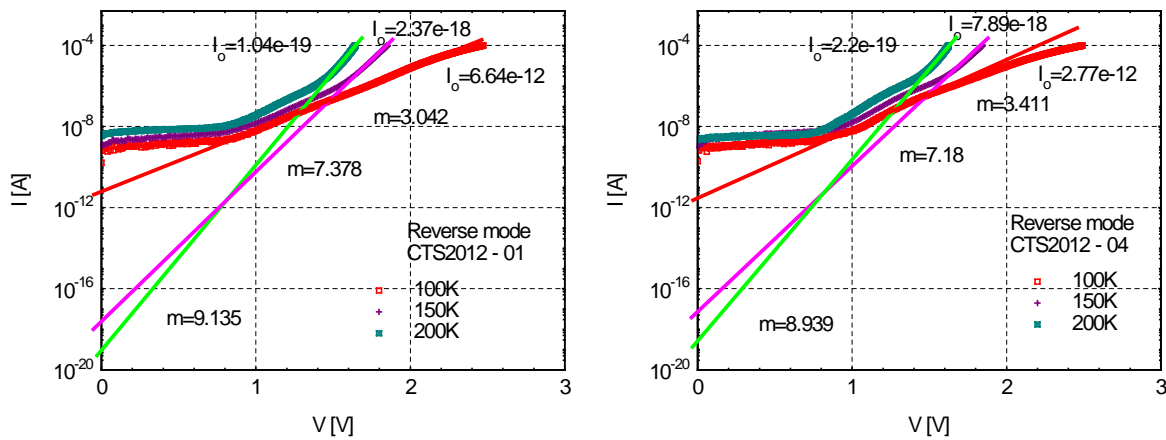


Fig. 6.85 I - V characteristic in reverse mode in semi-logarithmic scale with linear approximation for the thermionic emission current component analysis for samples CTS2012 – 01 and 04 for temperatures 100 K, 150 K and 200 K

Figure 6.85 shows the evaluation of I - V characteristic for samples CTS2012-01 (left) and CTS2012-04 (right) for the temperatures 100 K, 150 K and 200 K, respectively. Values of the slope m of linear approximation, calculated values of β_{TE} and the ideality factor for thermionic emission current determined from β_{TE} for samples CTS2012-01 and CTS2012-04 for temperatures 100 K, 150 K and 200 K are shown in Tabs. 8 and 9.

Tab. 8. Values of m , β_{TE} and ideality factor n calculated for sample CTS2012 – 01 for temperatures 100 K, 150 K and 200 K

Temperature [K]	m [V ⁻¹]	β_{TE} [V ⁻¹]	n [-]
200	9.135	21.02	2.76
150	7.378	16.98	4.55
100	3.042	7.00	16.56

Tab. 9. Values of m , β_{TE} and ideality factor n calculated for sample CTS2012 – 04 for temperatures 100 K, 150 K and 200 K

Temperature [K]	m [V ⁻¹]	β_{TE} [V ⁻¹]	n [-]
200	8.939	20.56	2.82
150	7.18	16.52	4.68
100	3.411	7.85	14.76

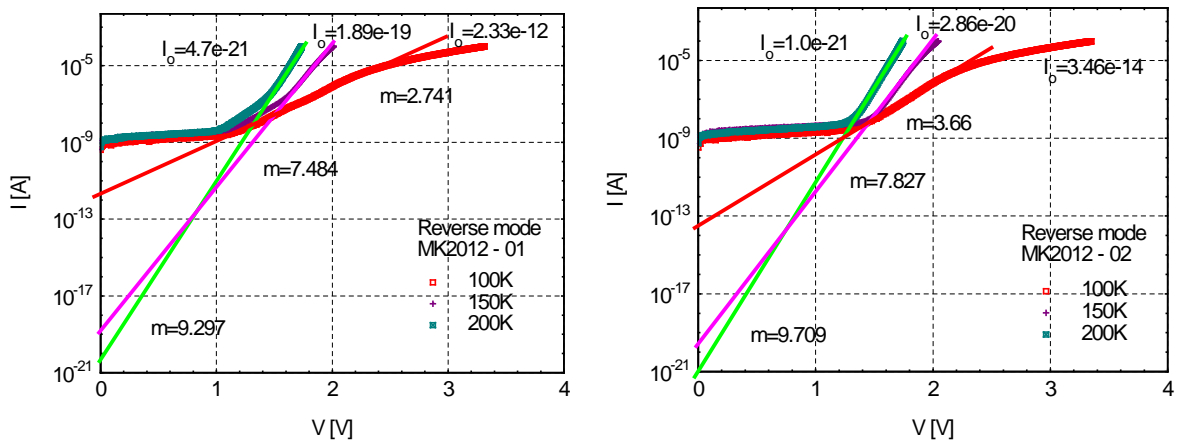


Fig. 6.86 I - V characteristic in reverse mode in semi-logarithmic scale with linear approximation for the thermionic emission current component analysis for samples MK2012 – 01 and 02 for temperatures 100 K, 150 K and 200 K

Tab. 10. Values of m , β_{TE} and ideality factor n calculated for sample MK2012 – 01 for temperatures 100 K, 150 K and 200 K

Temperature [K]	m [V ⁻¹]	β_{TE} [V ⁻¹]	n [-]
200	9.297	21.39	2.71
150	7.484	17.22	4.49
100	2.741	6.31	18.4

Tab. 11. Values of m , β_{TE} and ideality factor n calculated for sample MK2012 – 02 for temperatures 100 K, 150 K and 200 K

Temperature [K]	m [V ⁻¹]	β_{TE} [V ⁻¹]	n [-]
200	9.709	22.34	2.59
150	7.827	18.01	4.29
100	3.66	8.42	13.8

We can see that ideality factor value is in the range 2 to 3 at temperature 200 K for all the samples which is close to the theoretical value published for Schottky diodes and MIS structures [57], [58]. The ideality factor value strongly increases with decreasing temperature. This high value of ideality factor can be caused by the considerable contribution of tunneling current component to the total current.

6.2.11. Space charge limited current

Space charge limited current component was observed for several samples of KOL 2012 series in both normal and reverse mode voltage bias. Moreover the trap-charge-limited current was observed at low bias voltage in normal mode.

Current density J dependence on the electric field E in logarithmic scale for sample KOL2012-03 in reverse mode for temperature 12 K and 80 K, respectively, is shown in Fig. 6.87. We can see that measured data for temperature 12 K fit to the quadratic approximation in the electric field range from 0.02 to 0.3 MVcm⁻¹(Fig. 6.87 left graph). This corresponds to the space charge limited current when current density increases toward the square law [56, 57]. Space charge limited current component became negligible when increasing the temperature above 20 K for this sample in reverse mode. Figure 6.87 (right graph) shows the $\log J$ vs. $\log E$ dependence for temperature 80 K, where the ohmic current component is dominant up to the electric field 0.06 MVcm⁻¹. For higher electric field range 0.06 to 0.3 MVcm⁻¹ the current density increases with the power 3 which can cover the charge transport via the trap-charge-limited current. For

electric field above 0.3 MVcm⁻¹ the thermionic emission limited current and Fowler Nordheim tunneling is pronounced. Figures 6.88 (right graph) and 6.90 (right graph) show the log J vs. log E dependence in reverse mode for sample KOL2012-05 for temperatures 12 K and 60 K, respectively. Here the charge limited current component is negligible, ohmic current is dominant up to electric field 0.08 and for electric field above 0.3 the thermionic emission limited current and Fowler Nordheim tunneling is pronounced. For electric field range 0.08 to 0.3 MVcm⁻¹ the current density increases with the power 3 which can cover the charge transport via the trap-charge-limited current similarly as for sample KOL2012-03 at temperature above 20 K.

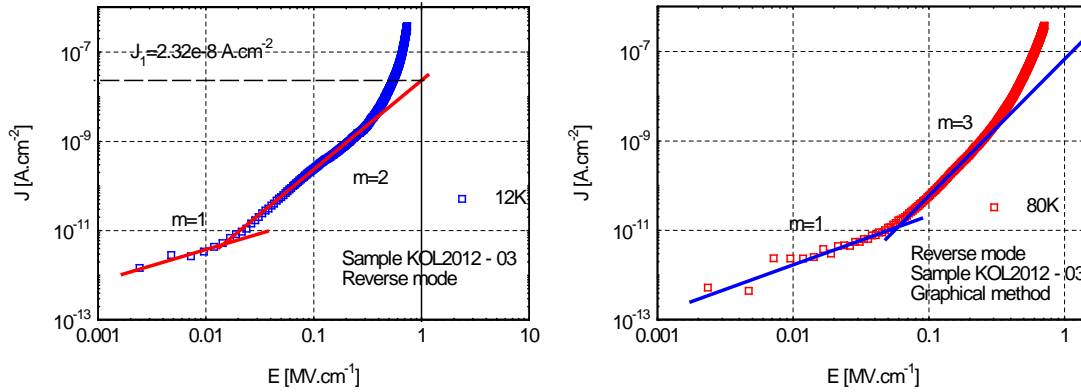


Fig. 6.87 Current density (log J) vs. electric field (log E) for sample KOL2012 – 03 for reverse mode at temperatures 12 K (left) and 80 K (right)

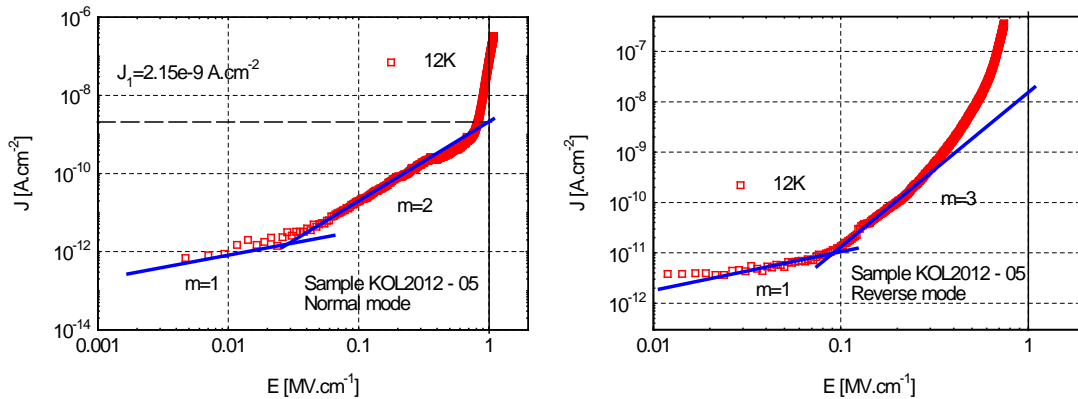


Fig. 6.88 Current density (log J) vs. electric field (log E) for sample KOL2012 – 05 in normal mode and in reverse mode at temperature 12 K

Current density J dependence on the electric field E in logarithmic scale for sample KOL2012-05 in normal mode for temperature 12 K is shown in Fig. 6.88 (left graph). We can see that measured data for temperature 12 K fit to the quadratic approximation in the electric field range from 0.03 to 0.8 MVcm⁻¹. This corresponds to the space charge limited current component. For electric field above 0.9 MVcm⁻¹ the Fowler-Nordheim tunneling current component is dominant (see Chapter 6.2.8). Figures 6.89 and 6.90 (left graph) show the log J vs. log E dependences in normal mode for temperatures 20 K, 30 K and 60 K, respectively. We can see that for lower electric field in the range 0.04 to 0.3 MVcm⁻¹ the charge transport is governed by the trap-charge-limited current (the slope in log-log graph is $m = 3$). For higher electric field in the range 0.3 to 0.8 MVcm⁻¹ the trapping sites are already filled and all additionally injected

carriers contribute to the space-charge-limited current (the slope in log-log graph is $m = 2$). From the values of current density J_{SC1} obtained from the intersection of quadratic approximation with the line $E = 1 \text{ MVcm}^{-1}$ we can calculate the mobility of charge carriers from Eq. 3.9. Table 12 shows the calculated value for sample KOL2012 – 03 for reverse mode at temperatures 12 K, and for sample KOL2012 – 05 for normal mode at temperatures 12 K, 20 K, 30 K and 60 K.

Tab. 12. Mobility of charge carriers m for sample KOL2012 – 03 for reverse mode at temperatures 12 K and for sample KOL2012 – 05 for normal mode at different temperatures

Sample No.	Temperature [K]	Mode	$J_{SC1} [\text{Acm}^{-2}]$	$m[\text{m}^2\text{V}^{-1}\text{s}^{-1}]$
KOL2012-03	12	reverse	2.32E-08	4.59E-06
KOL2012-05	12	normal	2.15E-09	4.25E-07
KOL2012-05	20	normal	5.40E-09	1.07E-06
KOL2012-05	30	normal	8.40E-09	1.66E-06
KOL2012-05	60	normal	1.17E-08	2.31E-06

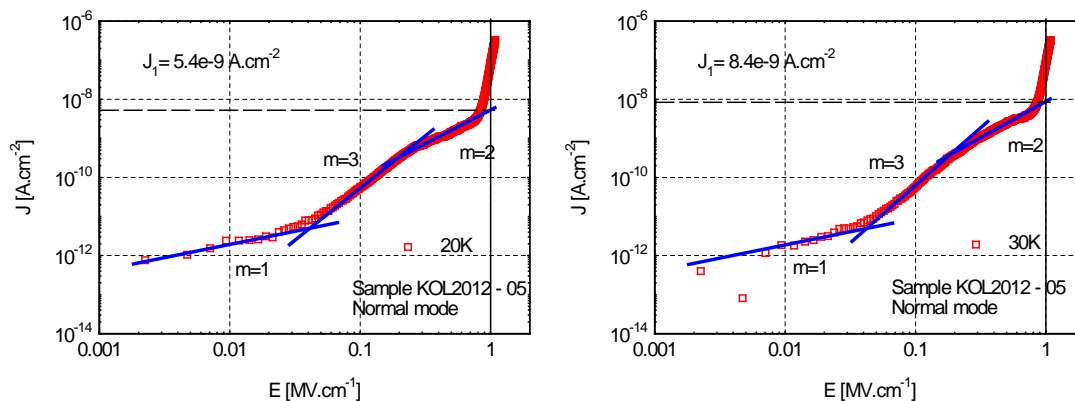


Fig. 6.89 Current density ($\log J$) vs. electric field ($\log E$) for sample KOL2012 – 05 in normal mode at temperatures 20 K and 30 K

Figures 6.91 and 6.92 show the $\log J$ vs. $\log E$ dependences in normal mode for samples MK2012 – 02 (temperatures 12 K and 150 K) and CTS2012 – 04 for temperatures 20 K, 200, and 250 K, respectively. We can see that only ohmic current component and Fowler-Nordheim tunneling current component is observed for sample MK2012-02. For sample CTS2012-04 the space charge limited current is observed in the electric field 0.5 to 2.0 MVcm^{-1} for $T = 250 \text{ K}$. The value of mobility of charge carriers is $3.8 \times 10^{-8} \text{ m}^2\text{V}^{-1}\text{s}^{-1}$ (determined for sample CTS2012-04 for $T = 250 \text{ K}$ for determined value $J_{SC1} = 2.3 \text{ Acm}^{-2}$).

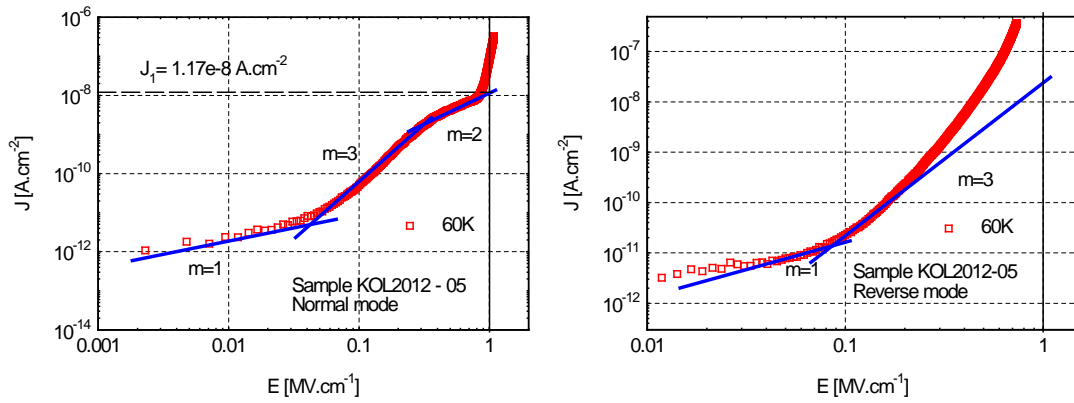


Fig. 6.90 Current density (log J) vs. electric field (log E) for sample KOL2012 – 05 in normal mode and in reverse mode at temperature 60 K

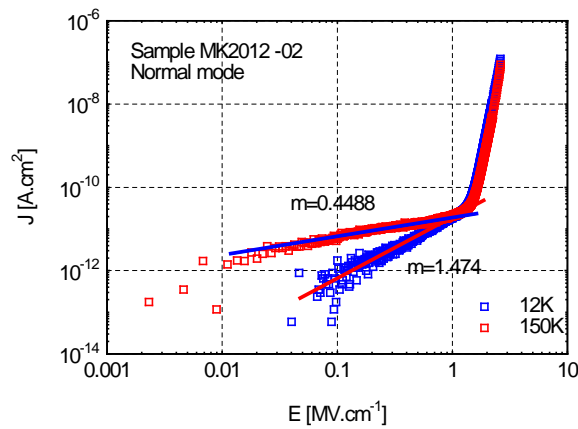


Fig. 6.91 Current density (log J) vs. electric field (log E) for sample MK2012 – 02 in normal mode for temperature 12 K and 150 K

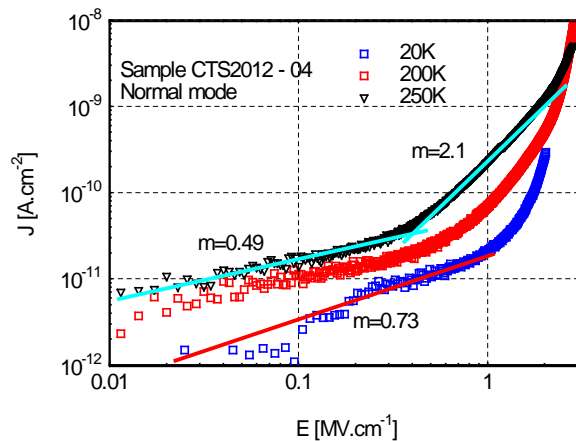


Fig. 6.92 Current density (log J) vs. electric field (log E) for sample CTS2012 – 04 in normal mode for temperature 20 K, 200 K and 250 K

7. Discussion

The correlation between diffuse voltage and donor concentration for all evaluated samples is shown in Fig. 7.1 for temperature 300 K. We can see that the lowest diffuse voltage value is observed for samples of KOL2012 series. This is an agreement with the assumption that potential barrier formed on the Ta₂O₅ – cathode interface is lower comparing to the potential barrier in capacitors with MnO₂ cathode. The highest value of U_D is determined for samples of MK2012 series. We can see in Chapter 6.2 that leakage current value is lowest for this series. Donor concentration is in the range $1.6 \times 10^{18} \text{ cm}^{-3}$ to $2.3 \times 10^{18} \text{ cm}^{-3}$ for all measured samples while the lowest donor concentration was observed for sample of series MK2012. The lowest donor concentration and highest value of diffuse voltage determined for series MK2012 is in agreement with assumption that the tantalum pentoxide prepared with lower concentration of oxygen vacancies exhibit lower value of electron affinity and higher barriers on the Ta₂O₅/anode and Ta₂O₅/cathode interfaces.

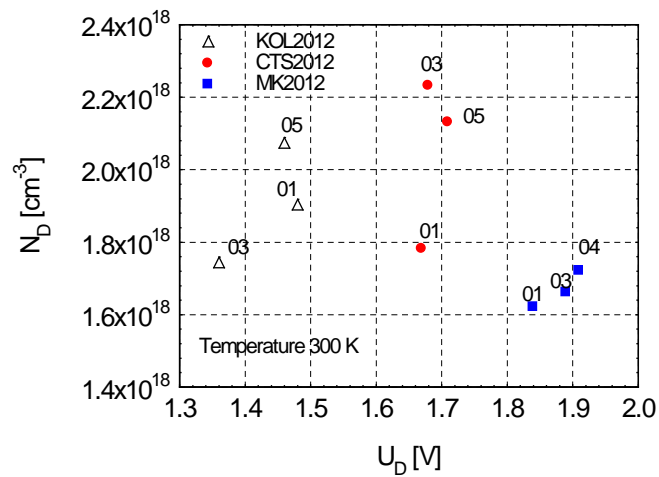


Fig. 7.1 Donor concentration N_D vs. diffuse voltage U_D for all series and selected samples for temperature 300 K

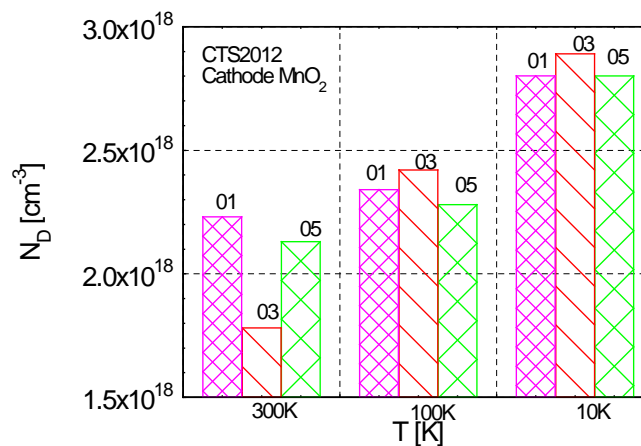


Fig. 7.2 Donor concentration for different temperatures for samples CTS2012 – 01, CTS2012 – 03, CTS2012 – 05

Figure 7.2 shows the calculated values of donor concentration for the samples of CTS2012 series for different temperatures. We can conclude that with decreasing temperature the effective concentration of donors in Ta₂O₅ layer increases.

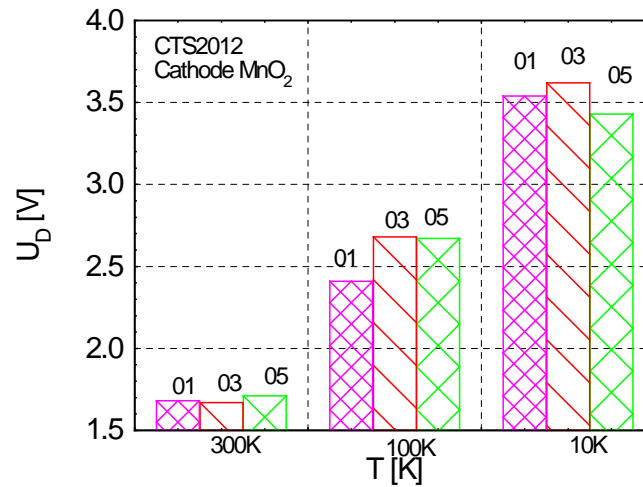


Fig. 7.3 Diffuse voltage U_b vs. temperature for series CTS2012

Figure 7.3 show the determined values of diffuse voltage for the samples of CTS2012 series for different temperatures. Diffuse voltage value increases with decreasing temperature reaching value about 3.5 V for temperature 10 K. Diffuse voltage value corresponds to the potential barrier formed on the interface between cathode and tantalum pentoxide. This barrier was published to be in the range from 1.8 – 2.4 eV for capacitors with MnO₂ cathode [15 – 18]. This value is in agreement with our results measured for temperatures 300 to 100 K while the value determined for 10 K is about 1 V higher.

The measurements of I - V characteristics were performed in the temperature range 12 K to 250 K. The results on tantalum capacitors with CP cathode show that DCL decreases with decreasing temperature both in normal and reverse modes. The results measured for the samples with MnO₂ cathode, both from series CTS2012 and MK2012 show, that the leakage current value increases with decreasing temperature for voltage bias in normal mode, while the reverse bias the DCL decreases with decreasing temperature.

Both analytical and graphical methods were used for the I - V characteristics evaluation. From both methods it follows that ohmic and tunneling current components are dominant in the temperature range below 100 K. For samples KOL2012 with CP cathode also additional current components, tunneling from HOMO level and space charge limited current, respectively, were observed in this temperature range; however they are pronounced only in the electric field range approx. 0.05 to 0.8 MVcm⁻¹ in normal mode and 0.02 to 0.3 MVcm⁻¹ in reverse mode, respectively.

Tunneling current parameter U_T and tunneling current density parameter E_T were determined from analytical and graphical evaluation of measured I - V characteristics. These parameters are summarized in Figs. 7.4 and 7.5 for normal mode characteristics and in Figs. 7.7 and 7.8 for reverse mode characteristics. From equations 3.19 and 3.21 it follows, that the relation between U_T and E_T is given as $U_T = d \cdot E_T$, where d is the thickness of Ta₂O₅ layer.

Figure 7.4 shows the temperature dependence of parameters U_T determined from analytical evaluation of I - V characteristics in normal mode. We can see that U_T value increases with decreasing temperature in the whole studied temperature range for samples of series KOL2012 with CP cathode. For the samples of series CTS2012 and MK2012 with MnO₂ cathode U_T value increases with decreasing temperature in the range 150 to 60 K. With further temperature decrease U_T value slightly decreases and U_T value fall down in between temperatures 20 to 12 K.

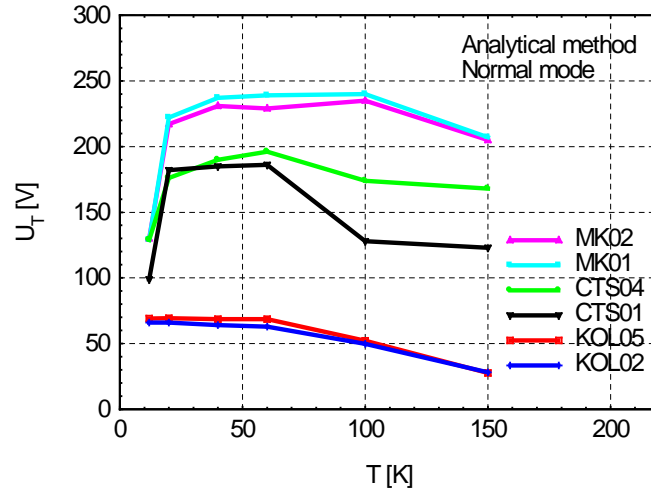


Fig. 7.4 U_T tunneling parameter vs. temperature from the analytical method in normal mode for the temperature range from 12 K up to 150 K in normal mode

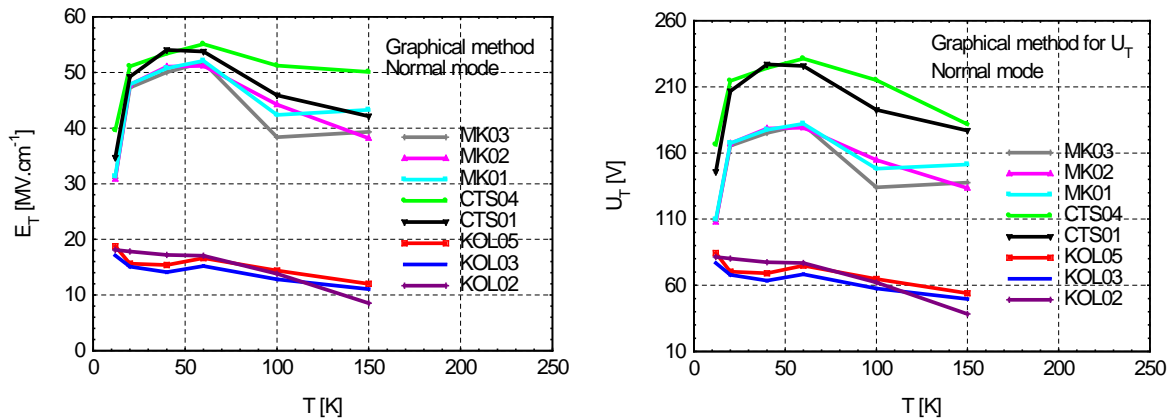


Fig. 7.5 E_T and U_T tunneling parameters vs. temperature from the graphical method in normal mode for the temperature range from 12 K up to 150 K

Identical shape of characteristics E_T vs. T and U_T vs. T was determined from graphical evaluation of I - V characteristics (see Fig. 7.5) both for capacitors with CP and MnO₂ cathode. From E_T and U_T values we can calculate from equations 3.19 and 3.21, respectively, the height of energy barrier formed on cathode/Ta₂O₅ interface. The calculations were performed considering constant value of electron effective mass $m^* = 0.1 m_0$, where $m_0 = 9.1 \cdot 10^{-31}$ kg is the electron rest mass, and constant value of Ta₂O₅ layer thickness given in Tab. 3. The dependences of calculated height of energy barrier formed on cathode/Ta₂O₅ interface on the temperature are shown in Fig. 7.6 for all evaluated capacitor series. Energy barrier height determined for the temperature

150 K is about 0.4 – 0.7 eV for KOL2012 series, about 1.5 eV for CTS2012 series, and 1.5 to 1.9 eV for MK2012 series. The results determined for capacitors with MnO₂ cathode are comparable to those obtained from $1/C^2$ vs. V characteristics evaluation. Energy barrier height determined for capacitors with CP cathode is for about 0.5 eV lower comparing to results obtained from $1/C^2$ vs. V characteristics evaluation. Considering the difference between the MnO₂ and CP work functions, which is 0.6 eV, this should represent the approximate difference between the energy barriers formed on CP resp. MnO₂/Ta₂O₅ interface. Then we should expect energy barrier height about 0.9 to 1.3 eV for KOL2012 series. Lower energy barrier determined for electron tunneling for capacitors with CP cathode can be caused by the incorporating of the deep donor levels or interface states into the tunneling process.

Energy barrier height on cathode/Ta₂O₅ interface for capacitors with both CP and MnO₂ cathode increases with decreasing temperature in the range 150 to 50 K for about 0.3 eV. This increase can be induced by the shift of Fermi level with temperature – with decreasing temperature the Fermi level moves close to the defect band energy level, while at the room temperature it is placed approximately in the middle between the defect band and the conduction band in Ta₂O₅ (see Fig. 7.13).

Calculated decrease of energy barrier height value for the temperatures below 20 K can be caused either by the decrease of effective thickness of barrier for electron tunneling due to band-bending (see Fig. 7.13) or by the change of value of electron effective mass. Considered value $m^* = 0.1 m_0$ is probably not valid in the extra low temperature range for samples with MnO₂ cathode.

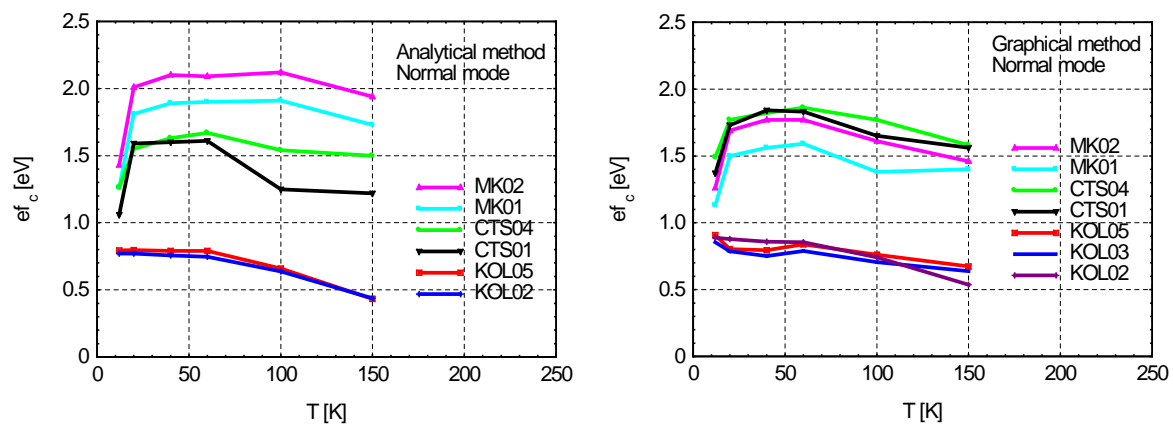


Fig. 7.6 Potential barrier height from the analytical method (left) and graphical method (right), dependence of the potential barrier on the cathode side vs. temperature from 12 K up to 150 K for all samples of evaluated series

Figure 7.7 shows the temperature dependence of parameters U_T determined from analytical evaluation of I - V characteristics in reverse mode. We can see that U_T value decreases with increasing temperature in the temperature range 12 to 100 K for samples of series KOL2012 with CP cathode and in the range 12 to 60 K for samples with MnO₂ cathode, respectively. Then determined U_T value strongly increases with increasing temperature for all capacitor series.

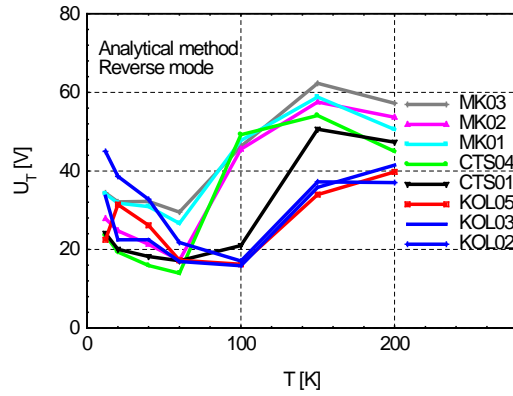


Fig. 7.7 U_T tunneling parameter vs. temperature from the analytical method in reverse mode for the temperature range from 12 K up to 200 K

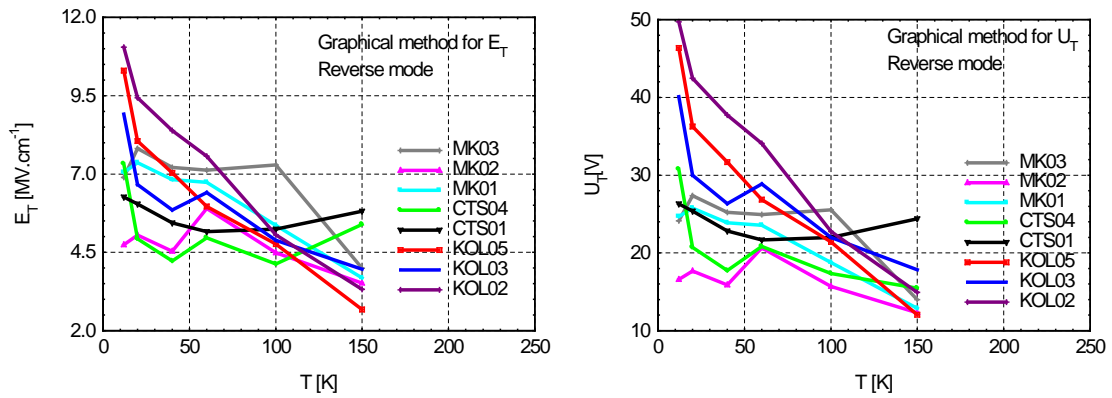


Fig. 7.8 E_T and U_T tunneling parameters vs. temperature from the graphical method in reverse mode for the temperature range from 12 K up to 150 K

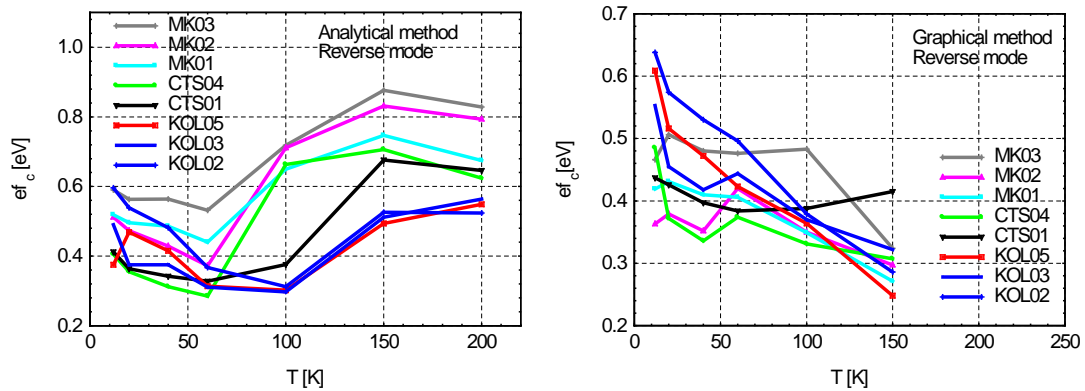


Fig. 7.9 Potential barrier height from the analytical method (left) and graphical method (right), dependence of the potential barrier on the anode side vs. temperature from 12 K up to 150 K for all samples of evaluated series

Temperature dependence of E_T and U_T determined from graphical evaluation of $I-V$ characteristics in reverse mode is shown in Fig. 7.8 both for capacitors with CP and MnO₂ cathode. Here the values of both parameters decreases with increasing temperature in the whole temperature range 12 to 150 K for all capacitors of studied series.

The dependences of calculated height of energy barrier formed on anode/Ta₂O₅ interface on the temperature determined from both analytical and graphical method are shown in Fig. 7.9 for all evaluated capacitor series. Figures 7.10 to 7.12 show the comparison of results from analytical and graphical method for each evaluated series. We can see that the results from both methods are comparable in the temperature range 12 to 100 K for all samples of KOL2012 series and sample CTS2012-01, and in the temperature range 12 to 60 K for sample CTS2012-04 and all samples of MK2012 series. Here the energy barrier height decreases with increasing temperature for 0.2 to 0.3 eV. This increase can be induced by the shift of Fermi level with temperature – with decreasing temperature the Fermi level moves close to the defect band energy level, while at the room temperature it is placed approximately in the middle between the defect band and the conduction band in Ta₂O₅. This process is the same as on the Ta₂O₅/cathode interface. The calculated increase of barrier height indicated from analytical method in the temperature range 100 to 200 K can be caused by neglecting additional current components in the *I-V* characteristic fitting. However further study of transport characteristics in the temperature range 100 to 300 K should be done.

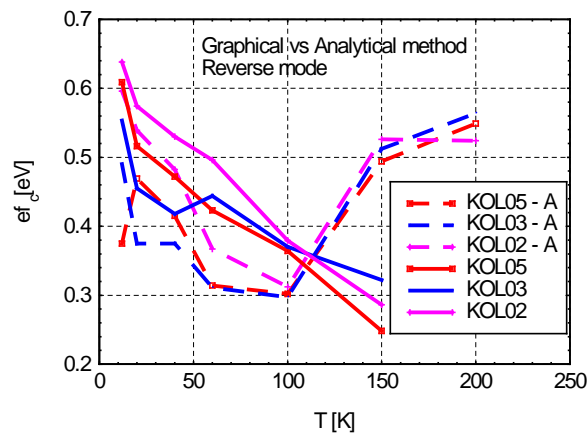


Fig. 7.10 Comparison of the potential barrier height on the anode side from the analytical method and graphical method, dependence of the potential barrier vs. temperature from 12 K up to 150 K for samples of series KOL2012

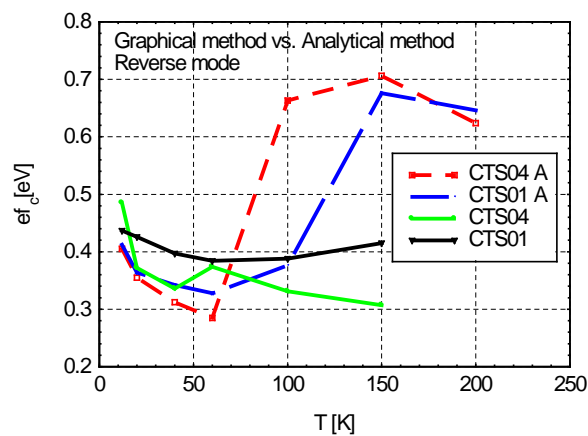


Fig. 7.11 Comparison of the potential barrier height on the anode side from the analytical method and graphical method, dependence of the potential barrier vs. temperature from 12 K up to 150 K for samples of series CTS2012

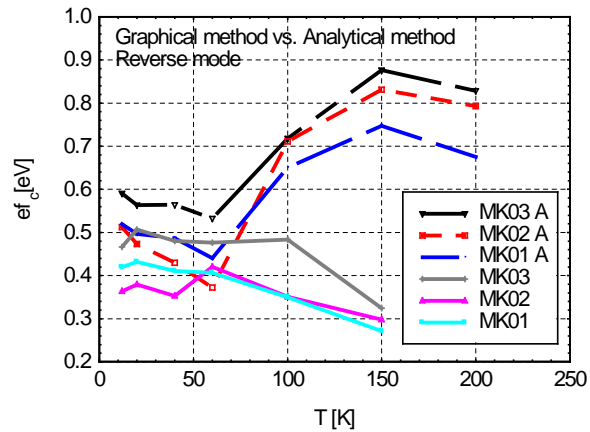


Fig. 7.12 Comparison of the potential barrier height on the anode side from the analytical method and graphical method, dependence of the potential barrier vs. temperature from 12 K up to 150 K for samples of series MK2012

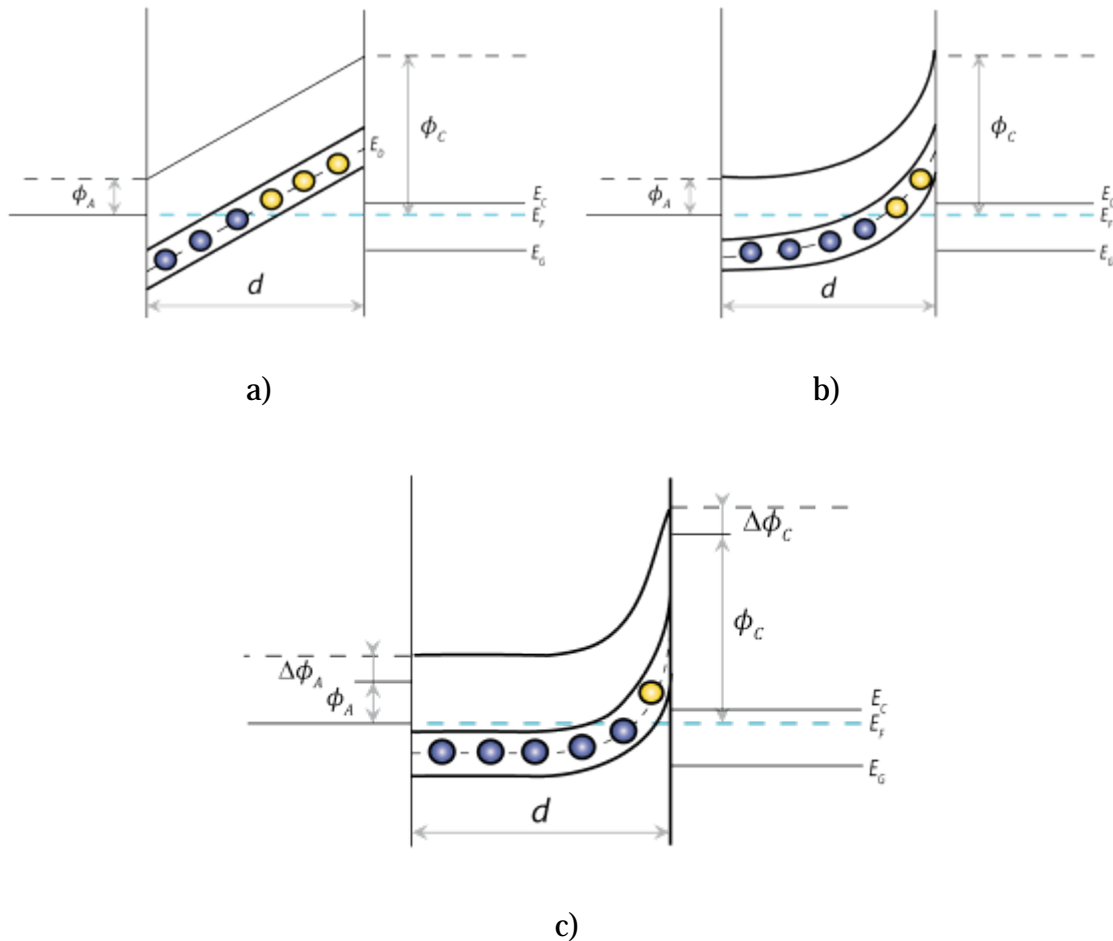


Fig. 7.13 Change of energy band structure in the MIS model for tantalum capacitor: a) triangular potential barrier for Fowler-Nordheim tunneling; b) decrease of potential barrier width for electron tunneling due to the band-bending; c) increase of potential barrier height due to the shift of Fermi level with temperature – Fermi level draw closer to the donor energy band

Figure 7.13 shows the changes of energy band structure in the MIS model of tantalum capacitor. Here the width of triangular type energy barrier for electron tunneling (a) can be reduced due to the band-bending (b) which can lead to the increase of tunneling current. The probability of charge excitation from the donor level decreases with decreasing temperature, which has an impact on the decrease of ionized donor states (ionized donors are highlighted by yellow color in the drawing). The decrease of temperature induces the shift of Fermi level – with decreasing temperature the Fermi level moves close to the defect band energy level (c) which leads to the increase of potential barrier on both M-I and I-S interfaces (here Df_A is barrier height increase on the anode side and Df_c is barrier height increase on the cathode side, respectively).

8. Conclusion

The charge transport mechanisms pronounced in tantalum capacitors, with both conductive polymer and manganese dioxide cathode in normal and reverse mode, respectively, are summarized in Tabs. 13 and 14. Here Ohmic denotes ohmic current component, PF is Poole-Frenkel current component, SCHLC is space-charge limited current, T-HOMO is tunneling current from HOMO level of conducting polymer into the defect bands in the Ta₂O₅ layer, Tunnel is Fowler Nordheim tunneling current through the triangular potential barrier. The electric field range, where appropriate transport mechanism is dominant, is determined for each current mechanism for both normal and reverse mode voltage bias. We can see that electric field range for ohmic and tunneling current component, respectively, is not the same for normal and reverse mode. That is influenced by the band-diagram asymmetry, where the barrier on the anode-Ta₂O₅ interface is significantly lower than the barrier on the cathode-Ta₂O₅ interface. Then the electron tunneling is observed for lower electric field in the reverse mode.

Tab. 13. Charge transport mechanisms summary in normal mode

Normal mode						
Current components:		Ohmic	PF	SCHLC	T-HOMO	Tunnel
		<i>DE</i> [MV.cm ⁻¹]				
Sample	Temperature					
KOL2012	12 – 100 K	<0.05	-	0.02-0.3	0.1-0.9	>0.9
	100 – 250 K	<0.05	0.1-0.6	-	-	>0.9
CTS2012	12 – 100 K	<0.8	-	-	-	>2.5
	100 – 250 K	<0.8	-	0.5-2 (250 K only)	-	>2.5
MK2012	12 – 100 K	<0.8	-	-	-	>2.1
	100 – 250 K	<0.8	-	-	-	>2.1

Tab. 14. Charge transport mechanisms summary in reverse mode

Reverse mode					
Current components:		Ohmic	TELC	SCHLC	Tunnel
		<i>DE</i> [MV.cm ⁻¹]	<i>DE</i> [MV.cm ⁻¹]	<i>DE</i> [MV.cm ⁻¹]	<i>DE</i> [MV.cm ⁻¹]
Sample	Temperature				
KOL2012	12 – 100 K	<0.08	-	0.02-0.3 (12 K only)	>0.65
	100 – 250 K	<0.08	0.2 – 0.5	-	>0.65
CTS2012	12 – 100 K	<0.3	-	-	>0.75
	100 – 250 K	<0.25	0.3 – 0.6	-	>0.75
MK2012	12 – 100 K	<0.5	-	-	>0.75
	100 – 250 K	<0.25	0.25-0.5	-	>0.75

Space-charge limited current and tunneling current from HOMO level of conducting polymer into the defect bands in the Ta₂O₅ layer are the components pronounced in the certain temperature range only. In studied samples the tunneling current from HOMO level was observed only on capacitors with CP cathode, while space-charge limited current is not limited to this cathode material. SCHLC was observed in the temperature range 12 to 80 K for samples with CP cathode and for temperature 250 K for sample with MnO₂ cathode of CTS2012 series.

The thermionic emission limited current is pronounced in the reverse mode for samples with both cathode types for the temperatures above 100 K. Calculated value of ideality factor is in the range 2 to 3 at temperature 200 K for all the samples which is close to the theoretical value published for Schottky diodes and MIS structures. The ideality factor value strongly increases with decreasing temperature, it is in the range 4.2 to 4.7 for temperature 150 K, and increases up to 12.2 -19 for the temperature 100 K. This high value of ideality factor can be caused by the considerable contribution of tunneling current component to the total current. Then I can conclude that TELC component should be considered for the temperatures above 150 K, while for lower temperatures it can be neglected.

The cathode material influences the transport characteristics in the normal mode only. We can see (Tab. 13) that the tunneling current is dominant for electric field above 0.9 MV.cm⁻¹ for structures with CP cathode, while for electric field above 2.1 MV.cm⁻¹ or 2.5 MV.cm⁻¹, respectively, for structures with MnO₂ cathode. This effect is influenced by higher value of energy barrier on the cathode-Ta₂O₅ interface. The conductance of all evaluated samples increases with temperature and it varies in the range 10⁻¹⁵ to 10⁻¹⁴ Sm⁻¹ however the values determined for samples with CP cathode are 2 to 4 times higher than for samples with MnO₂ cathode. The concentration of donor states in tantalum pentoxide layer is about 2x10⁻¹⁸ cm⁻³ for all evaluated series, so the difference in ohmic conductivity in normal mode should be influenced by the cathode material. The influence of cathode on the reverse mode characteristics is negligible. The differences in electric field range for ohmic current and tunneling current components in reverse mode are more probably dependent on the differences in electron affinity of Ta₂O₅ layer among different series.

Diffuse voltage determined from the CV characteristics at the room temperature is in the range 1.3 to 1.4 V for capacitors with CP cathode, while it is in the range 1.7 to 1.9 V for capacitors with MnO₂ cathode. Potential barrier formed on the Ta₂O₅ – CP interface is lower comparing to the potential barrier in capacitors with MnO₂ cathode for about 0.6 eV.

Donor concentration is in the range 1.6x10¹⁸ cm⁻³ to 2.3x10¹⁸ cm⁻³ for all measured samples at the room temperature. The lowest donor concentration and highest value of diffuse voltage determined for series MK2012 is in agreement with assumption that the tantalum pentoxide prepared with lower concentration of oxygen vacancies exhibit lower value of electron affinity and higher barriers on the Ta₂O₅/anode and Ta₂O₅/cathode interfaces.

From the evaluation of series CTS2012 in the wide temperature range it follows, that the effective concentration of donors in Ta₂O₅ layer increases with decreasing temperature for about 40% and the diffuse voltage value increases from the value 1.6 V at 300 K with decreasing temperature reaching value about 3.5 V for temperature 10 K. The diffuse voltage value is in agreement with potential barrier heights measured for temperatures 300 to 100 K [15 - 18] while the value determined for 10 K is for about 1 V higher.

Energy barrier height determined from tunneling current component for the interface cathode-Ta₂O₅ for the temperature 150 K is about 0.4 – 0.7 eV for KOL2012 series, about 1.5 eV for CTS2012 series, and 1.5 to 1.9 eV for MK2012 series. The results determined for capacitors with MnO₂ cathode are comparable to those obtained from $1/C^2$ vs. V characteristics evaluation. Energy barrier height determined for capacitors with CP cathode is for about 0.5 eV lower comparing to results obtained from $1/C^2$ vs. V characteristics evaluation. Considering the difference between the MnO₂ and CP work functions, which is 0.6 eV, this should represent the approximate difference between the energy barriers formed on CP resp. MnO₂/Ta₂O₅ interface. Then we should expect energy barrier height about 0.9 to 1.3 eV for KOL2012 series. Lower energy barrier determined for electron tunneling for capacitors with CP cathode can be caused by the incorporating of the deep donor levels or interface states into the tunneling process.

Energy barrier height determined from tunneling current component (graphical evaluation) for the interface anode-Ta₂O₅ for the temperature 150 K is in the range 0.25 to 0.4 eV for all evaluated series. The value increases with decreasing temperature for about 0.3 eV in the range 150 to 12 K. The results determined from analytical method are in agreement with those from graphical evaluation of Fowler-Nordheim plot in the temperature range 12 to 60 K. For higher temperatures the increase of potential barrier is indicated from the analytical evaluation of tunneling current component. The calculated increase of barrier height indicated from analytical method in the temperature range 100 to 200 K can be caused by neglecting additional current components (e.g. thermionic emission limited current) in the I - V characteristic fitting. However further study of transport characteristics in the temperature range 100 to 300 K should be done.

The comparison of temperature dependences of energy barrier height for the interface anode-Ta₂O₅ and cathode-Ta₂O₅ shows that both characteristics increase with decreasing temperature in the range 150 to 20 K for about 0.3 eV. This increase can be induced by the shift of Fermi level with temperature – with decreasing temperature the Fermi level moves close to the defect band energy level, while at the room temperature it is placed approximately in the middle between the defect band and the conduction band in Ta₂O₅. Calculated decrease of cathode-Ta₂O₅ energy barrier height value for samples with MnO₂ cathode for the temperatures below 20 K can be caused either by the decrease of effective thickness of barrier for electron tunneling due to band-bending or by the change of the value of electron effective mass. Considered value $m^* = 0.1 m_0$ is probably not valid in the extra low temperature range for samples with MnO₂ cathode.

I have determined the mobility of charge carriers in the capacitor structure from the evolution of space charge limited current component. The mobility is $m = 4.25 \times 10^{-7} \text{ m}^2 \text{V}^{-1} \text{s}^{-1}$ in the reverse mode while in normal mode is mobility $m = 4.59 \times 10^{-6} \text{ m}^2 \text{V}^{-1} \text{s}^{-1}$. The value of mobility of charge carriers differs in normal and reverse mode. The mobility of charge carriers for normal mode increases with temperature in the range 12 to 60 K. In this temperature range mobility increases with $T^{3/2}$ in silicon, cadmium telluride and the other semiconductors. Very low value of mobility was determined for sample CTS2012-04 $m = 3.8 \times 10^{-8} \text{ m}^2 \text{V}^{-1} \text{s}^{-1}$ which is about for two orders of magnitude lower than for the other samples.

I have determined basic parameters of charge carrier transport in Ta₂O₅ oxide nanolayers and at interfaces with cathode and anode, respectively, which can be used to improve technology of tantalum capacitors production.

References

- [1.] FRANKLIN, B. *Experiments and Observations on Electricity: Letter IV to Peter Collinson*. [online]. [cit. 2014-12-07]. Available on website: <http://www.chemteam.info/Chem-History/Franklin-1749/Franklin-1749-Start.html>
- [2.] SZE, S. M., NG, Kwok K. (1981 Jan 01). *Physics of semiconductor devices*. OSTI Identifier, OSTI ID: 5381484. 1981.
- [3.] TEVEROVSKY, A. Reverse Bias Behavior of Surface Mount Solid Tantalum Capacitors. In: *CARTS-CONFERENCE*. COMPONENTS TECHNOLOGY INSTITUTE INC., 2002., p. 105-123.
- [4.] SZE, S M., NG, Kwok K. *Physics of semiconductor devices*. JOHN WILEY & SONS, 2006.
- [5.] PRYMAK, J. Derating differences in Tantalum-MnO₂ vs. Tantalum-Polymer vs. Aluminum-Polymer. In: *CARTS-CONFERENCE*. COMPONENTS TECHNOLOGY INSTITUTE INC., 2003, p. 278-280.
- [6.] GL MILLER, Tantalum and Niobium, BUTTERWORTHS SEI. PUBL., London, 1959.
- [7.] PRYMAK, J. D. New tantalum capacitors in power supply applications. In: *Industry Applications Conference, 1998. Thirty-Third IAS Annual Meeting. The 1998 IEEE*. IEEE, 1998, p. 1129-1137.
- [8.] SIKULA, J., et al. Conductivity mechanisms and breakdown of NbO capacitors. In: *CARTS-CONFERENCE*. COMPONENTS TECHNOLOGY INSTITUTE INC., 2004, p. 141.
- [9.] MANCEAU, J.-P., et al. Leakage current variation with time in Ta₂O₅ MIM and MIS capacitors. In: *Integrated Reliability Workshop Final Report, 2006 IEEE International*. IEEE, 2006, p. 129-133.
- [10.] GILL, J. Basic Tantalum Capacitor Technology: Technical information. [online]. [cit. 2014-12-07]. Available on website: <http://www.avx.com/docs/techinfo/bsctant.pdf>
- [11.] JOHNSON, J. B. The Schottky effect in low frequency circuits. *Physical Review*, 1925, p. 71, ISSN 0031-899X.
- [12.] INEMI Technology Roadmaps: AVX TECHNICAL PAPERS. 2009.
- [13.] Teslácký svět: Časopis pracujících n.p. Tesla Lanškroun. LANŠKROUN: TESLA LANŠKROUN, 1976-1993. ISSN 001175941.
- [14.] TANTALUM-NIOBIUM INTERNATIONAL STUDY CENTER. *Tantalum-Niobium International Study Center* [online]. 1974, 2014 [cit. 2014-12-07]. Available on website: <http://tanb.org/>
- [15.] ZEDNICEK, T., SIKULA, J., LEIBOVITZ, H. A Study of Field Crystallization in Tantalum Capacitors and its effect on DCL and Reliability. *CARTS USA*, 2009, p. 315-319.
- [16.] SIKULA, J., et al. Tantalum and Niobium Oxide Capacitors: Leakage Current, Anodic Oxidation and Reliability. *CARTS Europe*, 2007, p. 213-222.
- [17.] SIKULA, J., et al. Tantalum Capacitor as a Metal-Insulator-Semiconductor Structure. In: *CARTS-CONFERENCE*, 2000, p. 102-108.
- [18.] SIKULA, J., et al. Niobium oxide and tantalum capacitors: leakage current and MIS model parameters. In: *CARTS-CONFERENCE*. COMPONENTS TECHNOLOGY INSTITUTE INC., 2007, p. 337.
- [19.] SIKULA, J., et al. Ion Diffusion and Field Crystallization in Niobium Oxide Capacitors. *CARTS Europe*, 2011, p. 3-33.

- [20.] TEVEROVSKY, A. Degradation of leakage currents in solid tantalum capacitors under steady-state bias conditions. In: *Electronic Components and Technology Conference (ECTC), 2010 Proceedings 60th*. IEEE, 2010., p. 752-757.
- [21.] TACANO, M., ZEDNICEK, T., SIKULA, J., SEDLAKOVA, V., NAVAROVA H. AND MAJZNER, J., Ta and NbO High Voltage Capacitors: Leakage Current Kinetics for MnO₂ and Conducting Polymer Cathode. In: *CARTS-CONFERENCE*, COMPONENTS TECHNOLOGY INSTITUTE INC., 2007.
- [22.] HARADA, D. „Self-healing mechanism of Neo-capacitor “. *NEC Research & Development*, 1997, 301-305.
- [23.] PRYMAK, J. D. Conductive polymer cathodes-the latest step in declining ESR in tantalum capacitors. *APEC 2000 Program*, 2000.
- [24.] P. LORRAIN, D. R. Corson, *Electromagnetism: Principles and Applications*, Freeman, New York, 1997.
- [25.] SIKULA, J., et al. Tantalum Capacitor as a Metal-Insulator-Semiconductor Structure. In: *CARTS-CONFERENCE*. 2000. p. 102-108.
- [26.] SIKULA, J., et al. Niobium oxide and tantalum capacitors: leakage current and MIS model parameters. In: *CARTS-CONFERENCE*. COMPONENTS TECHNOLOGY INSTITUTE INC., 2007. p. 337.
- [27.] ZEDNÍČEK, T. New Tantalum Technologies Tantalum Polymer and Niobium OxideCapacitors. *AVX Czech Republic*, 4.
- [28.] HOLMAN, B. *The Electrical Characterization of Tantalum Capacitors as MIS Devices*. ProQuest, 2008.
- [29.] SEDLAKOVA, V., et al. Tantalum and Niobium oxide capacitors: Field crystallization, leakage current kinetics and reliability. In: *Microelectronics Proceedings (MIEL), 2010 27th International Conference on*. IEEE, 2010. p. 439-442.
- [30.] PRYMAK, J. Replacing MnO₂ with conductive polymer in solid tantalum capacitors. In: *CARTS-CONFERENCE*. COMPONENTS TECHNOLOGY INSTITUTE INC, 1999. p. 148-153.
- [31.] CHANELIERE, C., et al. Tantalum pentoxide Ta₂O₅ thin films for advanced dielectric applications. *Materials Science and Engineering: R: Reports*, 1998, 22.6: 269-322.
- [32.] SIKULA, J., et al. Niobium Oxide and Tantalum Capacitors: Quantum Effects in Charge Carrier Transport. *CARTS USA*, 2006, 421-427.
- [33.] ZEDNÍČEK, T., SITA, Z., PALA, S. TANTALUM CAPACITORS TECHNOLOGY FOR EXTENDED OPERATING TEMPERATURE RANGE. In: *CARTS-CONFERENCE*. COMPONENTS TECHNOLOGY INSTITUTE INC
- [34.] KOPECKY, M, CHVATAL, M, SEDLAKOVA, V. Electron transport in tantalum nanolayers: Low temperature characteristics. In: *Electronic System-Integration Technology Conference (ESTC), 2010 3rd*. IEEE, 2010. p. 1-5.
- [35.] KOPECKÝ, M., CHVÁTAL, M., SEDLÁKOVÁ, V. Charge carrier transport in Ta₂O₅ oxide nanolayers. *The 15th Conference - Student EEICT 2010*, NOVAPRESS s.r.o., 2010.
- [36.] KOPECKÝ, M. Electron transport in Ta nanolayers: Application to tantalum capacitors. In: *Electronics Technology (ISSE), 2010 33rd International Spring Seminar on*. IEEE, 2010. p. 212-215.
- [37.] SIKULA, J., et al. Leakage Current and Quantum Effects in Tantalum Capacitors. In: *CARTS-CONFERENCE*. COMPONENTS TECHNOLOGY INSTITUTE INC.

- [38.] KOPECKÝ, M.; CHVÁTAL, M.; SEDLÁKOVA, V. Electron transport in tantalum nanolayers: Low temperature characteristics. In: *Electronic System-Integration Technology Conference (ESTC), 2010 3rd*. IEEE, 2010. p. 1-5.
- [39.] KOPECKÝ, M. Electron Transport in Ta Nanolayers: Application to Tantalum Capacitors. In: *Proceedings Of The 16th Conference - Student EEICT 2010*, NOVAPRESS s.r.o., 2010. p. 99-103.
- [40.] KOPECKÝ, M., SEDLÁKOVÁ, V., HOLCMAN, V., PETTERSSON, H. Analysis of transport mechanisms for the Ta₂O₅ layers for low temperature range 80 K to 300 K. In: *MIDEM Society for Microelectronic, Electronic Components and Materials - Conference 2012 Proceedings*. Slovenia: MIDEM, 2012. p. 145-150.
- [41.] SEDLÁKOVÁ, V., ŠIKULA, J., MAJZNER, J., KOPECKÝ, M., TACANO, M., ZEDNÍČEK, T. Reliability of Passive Electronic Devices: Failure Mechanisms and Testing. In: *CARTS USA 2010 PROCEEDINGS. USA, New Orleans: Electronic Components Association*, 2010. p. 309-330.
- [42.] HARTMANN, C., A. The regulation of the electrical elementary quantum from the Schottky effect, *ANNALEN DER PHYSIK*, vol. 65, pp. 51-78, 1921, ISSN 0003-3804.
- [43.] SCHOTTKY, W. Small-shot effect and flicker effect. *Physical Review*, 1926, 28.1: 74.
- [44.] ŠIKULA, J., SEDLÁKOVÁ, V., SITA, Z. Charge Carriers Transport and Noise in Niobium Oxide and Tantalum Capacitors. In: *EDS ' 06 IMAPS CS International Conference Proceedings. Brno, Cz, 2006*. p. 154 ISBN: 80-214-3246- 2.
- [45.] SCHOTTKY, W. On spontaneous current fluctuations in various electricity conductors, *Annals of Physics*, vol. 57, pp. 541 – 567, 1918, ISSN 0003-4916.
- [46.] HOLMAN, B. The Electrical Characterization Of Tantalum Capacitors As Mis Devices. [online]. 2008 [cit. 2014-12-07]. Available on website: <http://www.ces.clemson.edu/~galapat>
- [47.] ŠIKULA, J., et al. Charge Carrier Transport in NbO and Ta Capacitors in Temperature Range 100 to 300 K. *CARTS Europe, Bad Homburg*, 2006.
- [48.] KUPAROWITZ, M. Studium degradace isolační vrstvy Ta₂O₅. *VUTIUM*, Vědecké spisy vysokého učení technického v Brně 2014.
- [49.] PELČÁK, J. Transport elektrického náboje v tantalovém kondenzátoru. *VUTIUM*, Vědecké spisy vysokého učení technického v Brně 2011.
- [50.] SEDLÁKOVÁ, V. Non-Destructive Testing Of Passive Electronic Components. *Edice Habilitační a inaugurační spisy. Edice Habilitační a inaugurační spisy*. Vědecké spisy vysokého učení technického v Brně, 2010. 38 p. ISBN: 978-80-214-4092- 0.
- [51.] VASINA, P., et al. Failure modes of tantalum capacitors made by different technologies. *Microelectronics Reliability*, 2002, 42.6: 849-854.
- [52.] SEDLÁKOVA, V., et al. Noise of Ta₂O₅ and Nb₂O₅ thin insulating films in the temperature range 10 K to 400 K. In: *Noise and Fluctuations (ICNF), 2011 21st International Conference on*. IEEE, 2011. p. 486-489.
- [53.] KOPECKÝ, M., CHVÁTAL, M., SEDLÁKOVÁ, V. Electron Transport in Ta₂O₅ Nanolayers with Conducting Polymer Cathode. In: *EDS 2010 IMAPS CS INTERNATIONAL CONFERENCE PROCEEDINGS. FIRST*. Brno: NOVAPRESS s.r.o., 2010. p. 179-184. ISBN: 978-80-214-4138- 5.
- [54.] ZEDNICEK, T., et al. Tantalum and niobium technology roadmap. In: *CARTS-CONFERENCE. COMPONENTS TECHNOLOGY INSTITUTE INC.*, 2002. p. 142-147.

- [55.] ZEDNICEK, T., et al. Tantalum and niobium technology overview. In: *Electronics Technology: Integrated Management of Electronic Materials Production, 2003. 26th International Spring Seminar on. IEEE, 2003.* p. 456-459.
- [56.] MONTERO, J. M., et al. Trap-limited mobility in space-charge limited current in organic layers. *Organic Electronics*, 2009, 10.2: 305-312.
- [57.] REDDY, V. RAJAGOPAL, et al. Electrical Properties and Current Transport Mechanisms of the Au/n-GaN Schottky Structure with Solution-Processed High-k BaTiO₃ Interlayer. *Journal of Electronic Materials*, 2014, 43.9: 3499-3507.
- [58.] DARLING, B. B. Current-voltage characteristics of Schottky barrier diodes with dynamic interfacial defect state occupancy. *Electron Devices, IEEE Transactions on*, 1996, 43.7: 1153-1160.

Author's products

KOPECKÝ, M.; Software for measuring electronic components called SUMBED in Labview. (2012)

KOPECKÝ, M.; Hardware for measuring electronic components called UMBED. (2012)

KOPECKÝ, M.; TRČKA, T.: Software for measuring; Software for measuring of charging, discharging and IV characteristics of capacitors. (2012)

TRČKA, T.; KOPECKÝ, M.: Software for measuring; Software for measuring of breakdown voltage and leakage current in capacitors. (2012)

KOPECKÝ, M.; ŠIMEK, M.: SNMP Multicast Monitor; SNMP Multicast Monitor. Software for monitoring multicast sessions. (2009)

Author's involvement in projects

Cooperation on the research intention MSM0021630503 (New Trends in Microelectronic SysSEMs and Nanotechnologies) MŠMT, Brno University of Technology, CZ; 2011-2012

FRVŠ, Brno University of Technology, CZ; 2011-2011

Modernization of cryostat laboratory for nondestructive testing of electronic components

Participation in grant - Stochastic phenomena in MIS and MIM semiconductor structures, Brno University of Technology, CZ; 2010-2010

Research methodologies for improving the quality of optoelectronic materials and components

Participation in grant GACR 102/09/H074 - Diagnostics of material defects using the latest defectoscopic methods, Brno University of Technology, CZ; 2009-2009

Participation in grant GA103/06/0708 - Acoustic and electromagnetic emission in materials research, Brno University of Technology, CZ; 2009-2009